Alma Mater Studiorum · Università di Bologna

Scuola di Scienze
Corso di Laurea Magistrale in Fisica

Climatological analysis of temperature and salinity fields in the Mediterranean Sea

Relatore:
Prof. Nadia Pinardi

Presentata da:
Michela Giusti

Correlatore:
Dott. Simona Simoncelli

Correlatore:
Dott. Marina Tonani

Sessione II
Anno Accademico 2013/2014

Acknowledgements

I am very grateful to my supervisor Professor Nadia Pinardi for his invaluable guidance and constant encouragement throughout my work and in the preparation of this thesis. Many thanks are also due to Dr. Simona Simoncelli, Dr. Marina Tonani and Alessandro Grandi for their thoughtful advice, precious help and cooperation.

Special thanks go to my parents, Luigina and Franco, and my aunt Antonietta for their unfailing encouragement and trust, as well as their support, both material and immaterial, throughout my studies, and, last but not least, to my fiancée, Giacomo, for his infinite patience, wisdom, and caring attitude. To him I dedicate this thesis.

This page is intentionally left blank.

Abstract

A climatological field is a mean gridded field that represents the monthly or seasonal trend of an ocean parameter. This instrument allows to understand the physical conditions and physical processes of the ocean water and their impact on the world climate. To construct a climatological field, it is necessary to perform a climatological analysis on an historical dataset. In this dissertation, we have constructed the temperature and salinity fields on the Mediterranean Sea using the SeaDataNet 2 dataset. The dataset contains about 140000 CTD, bottles, XBT and MBT profiles, covering the period from 1900 to 2013.

The temperature and salinity climatological fields are produced by the DIVA software using a Variational Inverse Method and a Finite Element numerical technique to interpolate data on a regular grid. Our results are also compared with a previous version of climatological fields and the goodness of our climatologies is assessed, according to the goodness criteria suggested by Murphy (1993). Finally the temperature and salinity seasonal cycle for the Mediterranean Sea is described.

Una climatologia rappresenta il campo medio mensile o stagionale di un parametro dell'oceano su una griglia regolare. Questo strumento permette di capire i processi e le condizioni fisiche dell'acqua e il loro impatto sul clima. Per costruire una climatologia è necessario compiere un'analisi climatologica su un dataset storico. In questa tesi sono state create climatologie di temperatura e salinità del Mediterraneo usando il dataset SeaDataNet 2. Questo dataset comprende circa 140000 profili misurati con CTD, bottiglie, XBT and MBT nel Mediterraneo e copre un periodo che va dal 1900 al 2013.

Per produrre le climatologie è stato usato il software DIVA che utilizza il Variational Inverse Method e il Finite Element method per interpolare i dati su una griglia regolare. Abbiamo poi comparato i risultati con quelli di una versione precedente, valutando la bontà delle nostre climatologie, in base ai criteri di 'goodness' introdotti da Murphy (1993). Infine abbiamo descritto il seasonal cycle per la temperatura e la salinità nel Mediterraneo.

This page is intentionally left blank.

Contents

List of Figures

This page is intentionally left blank.

List of Tables

This page is intentionally left blank.

Chapter 1

Introduction

In physical oceanography, climatology is the study of the trend of a hydrological or biochemical propriety of the ocean for annual, seasonal, and monthly periods. These studies are important to understand the physical conditions and physical processes of the ocean water and their impact on the world climate. For this reason, the oceanographic community has been collecting a huge amount of experimental data for several decades, in order to create complete, multidisciplinary, and international data sets that allowed to construct climatological fields of the ocean parameters. A climatological field is a mean field of an ocean parameter that represents the monthly or daily climatological state of the sea. This representation is 'the smoothest field that respects the consistency with the observed values over the domain of interest' [1] and permits to solve the 'gridding problem': we can redistribute the parameter values from an irregular distribution to a regular grid.

The aim of this work is to produce new three-dimensional temperature and salinity fields in the Mediterranean Sea through climatological analysis of SeaDataNet 2 *in situ* data set.

The dissertation is organized as follows:

- In chapter 1, a brief history of the climatological analyses is outlined;
- In chapter 2, SeaDataNet 2 data set is described, including the eight principles of the quality control of the data set.
- In chapter 3, a description of the data analysis algorithms is performed.
- In chapter 4, the results of the climatological analysis are presented.

- In chapter 5, a seasonal cycle analysis of temperature and salinity fields is performed.
- In chapter 6, the conclusions of the study are provided.

1.1 Climatological studies in the Mediterranean Sea

The Mediterranean Sea is among the oceanographically most interesting regions of the world ocean because of its unique features. Since many years, it has been the site of climatology projects. In fact, despite its little dimensions, it is the focus of a great range of processes and interactions, including for example, some physical processes of the global general circulation. The Mediterranean Sea is a semi-enclosed sea that has been divided by the oceanographers in two sub-basins: the Western Mediterranean and the Eastern Mediterranean. The boundary line between the two regions is the Sicily Strait. The reason for this division is not only geographic but especially related to hydrological and physical properties such as temperature, salinity, and circulation. As we can see from Figure 1.1, the Western Mediterranean includes: the Strait of Gibraltar, that controls the exchange of water between the Mediterranean Sea and the Atlantic Ocean; the Alboran Sea, enclosed between the Morocco coasts and the meridional Spain coasts; the Balearic Sea, which is delimited by the Spanish and French coasts in the West, and confines with the Algerian basin in the South, the Ligurian Sea in the North, and Sardinia and Corsica in the East; and the Tyrrhenian Sea, separated by the Sardinia channel. The Eastern Mediterranean includes the Adriatic Sea in the North, separated from the Southern Ionian basin by the Otranto strait, and the Levantine basin in the East, separated from the Aegean Sea by the Greek islands.

We now presents a briefly description of the vertical structure of the Mediterranean water masses and the general circulation. Traditionally it is possible to identify three principal water masses, that are related to their formation locations:

- The Modified Atlantic Water (MAW), which is located between the surface and 100 m, entering from the Strait of Gibraltar. Its path proceed in the zonal direction and it is possible to follow it observing the salinity values between 20 (in the Western basin) to 50 m (in the eastern basin).
- The Levantine Intermediate Water (LIW), which is located between 200 and 300 m, is produced in the Levantine basin during winter. Its circulation goes from east to west.

FIGURE 1.1: Mediterranean Sea.
Source: `http://media-2.web.britannica.com/eb-media/10/6010-004-373EBA60.jpg`

- The Mediterranean Deep Water (MDW), which is the deep water mass, is separated in two reservoirs from the Strait of Sicily. The western part (WMDW) was produced during winter in the Gulf of Lions, the eastern part (EMDW) in the Adriatic and the Aegean Sea also in winter.

The Mediterranean general circulation is forced by the wind stress and the buoyancy fluxes. It is possible to notice from Figure 1.2 that the northern areas are characterized by cyclonic circulation while the souther areas by anticyclonic circulation. This is related to the wind stress curl sign. An important features present in the Mediterranean basin are the gyres that generally are forced by wind stress. The cyclonic gyres, presented in the northern areas, are forced also by deep and intermediate water formation, while the southern gyres are forced of the intermediate waters. Another important component of the Mediterranean Sea are the mesoscale eddies that are different from gyres for the persistency time. We start to describe the general surface circulation (see Figure 1.2) from the entering of the AW from Gibraltar, that meandering around the two Alboran gyres. These gyres are different in dimension and time persistence. Between the eastern Alboran gyre and a cyclonic eddy there is The Almera-Oran front that gives the name at the eddy: Almera-Oran cyclonic eddy. After the Almera-Oran front we can see two different currents: one going northward toward the Ibiza channel and the other forming

an important segment of the Algerian Current. In this zone there are a frequently growth of large anticyclonic eddies, persisting for several months. In the central western Mediterranean there is a eastward current called the Western MidMediterranean Current (WMMC). This current merges at north with the southern border of the cyclonic flow called the Gulf of Lion gyre that reachs a northward current also called the Liguro–Provenal–Catalan Current. Eastward of the Balearic Islands, the WMMC flows in the open ocean turning southward along the western coasts of Sardinia and forming an intensified current called the Southerly Sardinia Current (SSC). The SSC flows along the Tunisian coastlines and forms another segment of the Algerian Current in the Sardinia Channel. In the southern Tyrrhenian Sea the reformed Algerian Current is divided in three branches: two branches flows in the Strait of Sicily and the third flows in the Tyrrhenian Sea. Furthermore in the Tyrrhenian Sea we can find three cyclonic gyres: the South-Western Tyrrhenian Gyre (SWTG), the South-Eastern Tyrrhenian Gyre (SETG) and the Northern Tyrrhenian Gyre (NTG). The SWTG forms in the middle of the Tyrrhenian Sea a northward current, called the Middle Tyrrhenian Current (MTC). Through the Strait of Sicily, the Algerian Current branches into the Sicily Strait Tunisian Current (SSTC) along the southern coasts and the Atlantic Ionian Stream (AIS). At about $13°E$ the SSTC turns northward around a large anticyclonic gyre called the Sirte Gyre (SG). The northern border of the SG is the AIS current that divided the Ionian Sea in two regions. North of the AIS there are an eastern boundary current, called Eastern Ionian Current (EIC), a weak cyclonic gyre, called the Northern Ionian Cyclonic Gyre and the Pelops Gyre (PG). Before passing the Cretan Passage the AIS forms a current along the North African coasts called the Cretan Passage Southern Current (CPSC). The other branches formed are the the Mid-Mediterranean Jet (MMJ) and the Southern Levantine Current (SLC). The first is located between the Mersa Matruh Gyre System (MMGS) at south and the Rhodes Gyre at north, and flows inside the Asia Minor Current that forms the Shikmona Gyre System. In the northern part of the Cretan Passage, before the Strait of Kassos, the continuation of the Asia Minor Current forms a large anticyclonic meander, encircling the area of the recurrent anticyclonic Ierapetra Gyre. The Adriatic Sea is dominated by the Middle and Southern Adriatic cyclonic gyres and the Eastern Adriatic Current and the Western Adriatic Coastal Current systems. The Aegean Sea shows a southward flow through the Cyclades (the Cretan Sea Westward Current (CSWC)) and in the northern area the circulation is dominated by a well-defined and high-intensity anticyclonic gyre: the North Aegean Sea Anticyclone (NASA).

The intermediate circulation shows in Figure 1.3 is related to the LIW and generally flows in

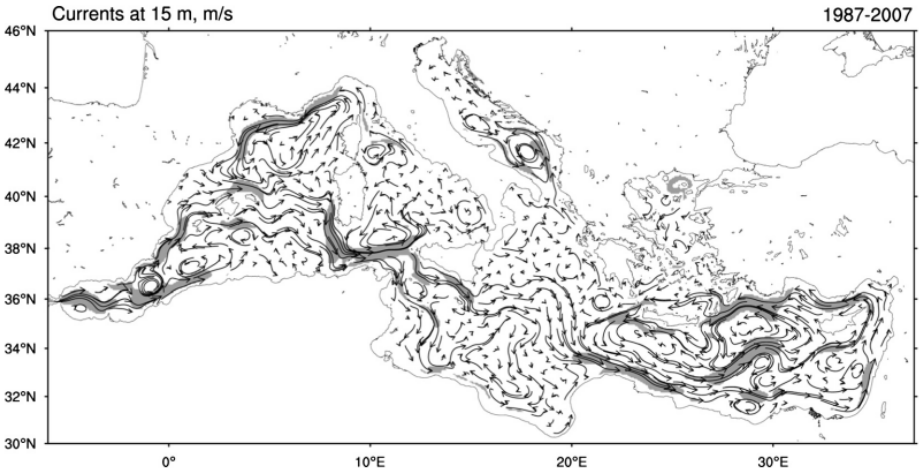

FIGURE 1.2: Mediterranean Sea circulation at 15 m.
Source: Pinardi *et al.*, 2013

the opposite direction to the surface circulation. The description starting from the Levantine basin because is the site of the LIW formation. The Rhodes Gyre and Ierapetra Ierapetra are consistent with the surface flow. The Mersa Matruh Gyre has a more varied structure due to a large meander of the MMJ and a large-amplitude anticyclone near the Egyptian coasts. The Shikmona Gyre System presents several anticyclonic semi–stationary eddies. the surface Cretan Sea Westward Current (CSWC) branches in the Ionian Sea into three streams at this depth. The first forms the southern border of the Pelops Gyre, the second turns eastward while the other joins the Sirte Gyre anticyclonic flow. The preferred path for the LIW is southward, along the Gulf of Sirte and westward LIW current of the Sicily Strait emerges as a branching of the SG south–western intensified current. Nortward of the AIS surface current there is a cyclonic gyre at this depth called the Northern Ionian Cyclonic Gyre (NICG). In the Western Mediterranean the LIW current turns cyclonically around the SWTG. The LIW path is characterized by two major branches one directed northward, toward the Gulf of Lion Gyre and the second westward toward the Strait of Gibraltar. At this depth the Gulf of Lion Gyre presents several cyclonic circulation structures inside the larger-scale gyre[1].

The Mediterranean Sea climatological water masses and the general circulation have been the object of study of many articles. One of the first climatological analyses of hydrographic data as a basis of geostrophic circulation in the Mediterranean has been conducted by Ovchinnikov (1966) [2].

[1] All the general circulation description is take from Pinardi *et al.*, 2013.

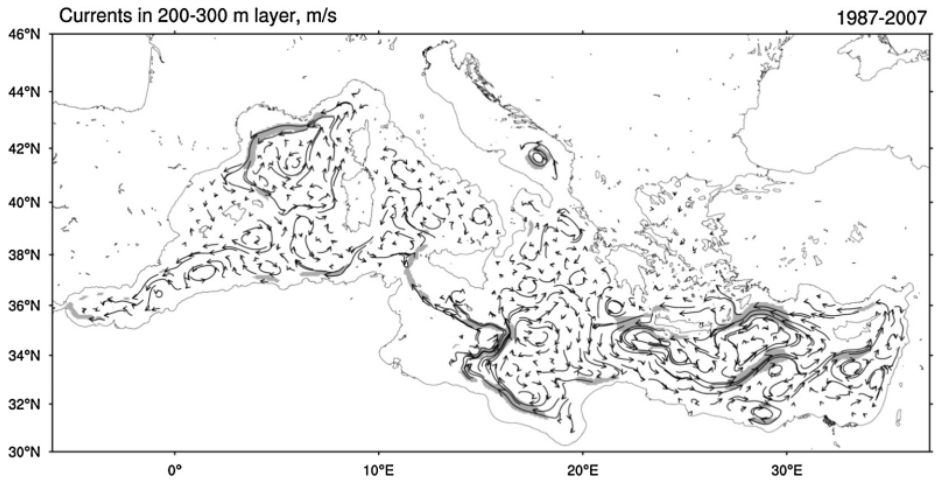

FIGURE 1.3: Mediterranean Sea circulation at 200–300 m.
Source: Pinardi *et al.*, 2013

Subsequent attempts to improve the knowledge of properties and circulation in the Mediterranean Sea, in particular in the Eastern Mediterranean, brought ambiguous and contradictory results [3]. In 1982, on the occasion of a Congress of the International Commission for the Scientific Exploration of the Mediterranean, an international research group was formed, called POEM (Physical Oceanography of the Eastern Mediterranean, 1984), supported by IOC/UNESCO (the Integovermental Oceanographic Commission). The group focused on the description of the phenomenology of the Eastern Mediterranean, by both analysing historical data, and collecting new data. Moreover, the group modelled the circulation of the sea and its physical, biological and chemical fundamental processes. The focus on the Eastern Mediterranean Sea was motivated by the very scanty knowledge of this basin compared with other world regions [3] as well as by a special interest in some of its characteristics reproducing the global ocean general circulation but with multiple and interactive space and time scales [4].

Following the POEM effort, Hecth *et al* (1988) [5] succeeded in describing the climatological seasonal and instantaneous kinematical properties of the mesoscale flow field on the Levantine Basin through the climatological water masses properties and their seasonal variations. The authors used a long time series data that covered the period from February 1979 to August 1984 on a regular grid domain (a box of 2°30' x 2° with the station located at 0.5°). They characterized some different water mass layers for temperature and salinity values and time duration. Furthermore they mapped the flow field and observed a new kind of mesoscale variabilities with the formation of eddies and jets never revealed before.

A more specific work aimed at the construction of a climatological atlas is the first numerical

Climatological Atlas of World Ocean by Levitus (1982) [6]. Levitus used data of the National Oceanographic Data Center (NODC), Washington, D.C, that included temperature, salinity and oxygen data measured from stations, mechanical bathythermographs, and expendable bathythermographs of the previous eighty years. Levitus followed a standard procedure comprising a quality control and a statistical check to eliminate spurious data and an objective analysis at standard levels on a one degree latitude-longitude grid between the surface and ocean bottom with a maximum depth of 5500 m.

In Figure 1.4, we show a climatological salinity field of the Mediterranean Sea during winter, reconstructed with the Levitus atlas by Brasseur *et al.* (1996) (whose for a climatological work in the Mediterranean Sea, will be described further on). It can be noted that the general trends of this parameter were adequately represented (in the Eastern Mediterranean values are higher than in the Western Mediterranean), although the spatial resolution did not conform to the regional scale. Levitus work was the start of the World Ocean Atlas (WOA) project by the Ocean Climate Laboratory of the National Oceanographic Data Center that produced new atlas at four year intervals from 1994 to 2013. The WOA project followed procedures that were similar to the ones employed by Levitus. In fact the WOA dataset consists of objectively-analysed global grids at 1° spatial resolution. Data are interpolated onto 33 standardised vertical intervals from the surface to 5500 m and the averaged fields are produced for annual, seasonal and monthly time-scales. The WOA 2013 extended the vertical levels from 33 to 102 to have more accurate quality control of observational data and study how mixed layer depth changes with reduced error. The WOA 2013 also added the 1° and 1/4° horizontal resolution versions for temperature and salinity field. All data and products are available on the WOA 2013 website[2].

As far as the Western Mediterranean Sea is concerned, an important climatological study was performed by Picco (1990) [7] who reconstructed a numerical atlas from 15000 hydrographic profiles coming from different sources for the period 1909-1987.

Brasseur *et al.* (1996)[1] introduced a new method to reconstruct the three dimensional fields of the properties of the Mediterranea Sea. Unlike their predecessors these authors used a variational inverse method to generate the climatological maps, rather than the objective analysis introduced by Gandin[3] (1969). They also used the CTD data in addition to bottle data coming from several datasets covering the period 1900-1987, namely the BNDO (Bureau National del Données Océaniques, Brest,French) and the U.S. NODC. All those in situ data were collected in a single

[2]http://www.nodc.noaa.gov/OC5/woa13/

[3]The two methods will be described in detail in the fourth chapter

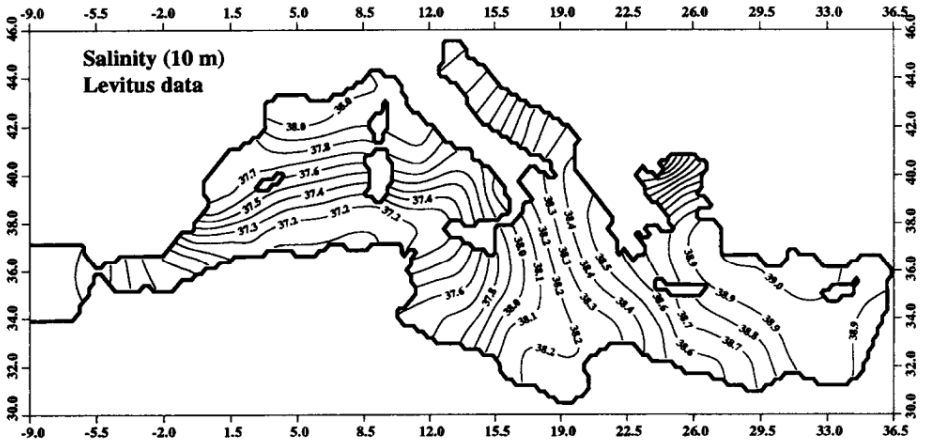

Fig. 1. Climatological salinity field in the Mediterranean surface layer (10-m depth) during winter: contouring of the Levitus (1982) gridded data set.

FIGURE 1.4: Salinity field at 10 m of the Mediterranean Sea.
Source: P. Brasseur *et al.* (1995)

dataset called MED2. After a brief description of the data distribution and reduction, Brasseur *et al.* concentrated on the variational analysis method to show that it was 'mathematically equivalent but numerically more efficient' than the objective analysis. They in fact compared the results obtained with the objective analysis method (see Figure 1.5) with those obtained through the variational analysis method (see Figure 1.6): actually, only minimal differences can be noticed between the two maps.

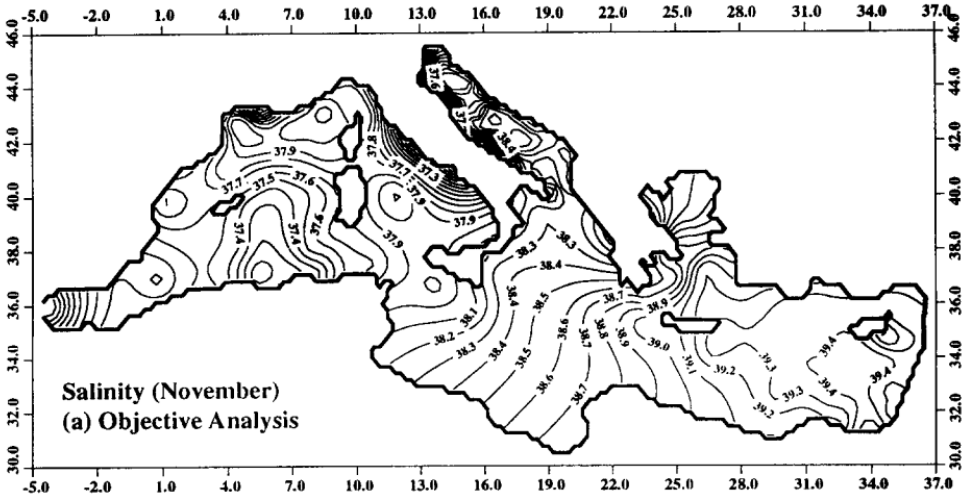

FIGURE 1.5: Salinity field at 10 m depth during November reconstructed from the statistical OA scheme.
Source: P. Brasseur *et al.* (1995)

With time, it has become evident that the results of such studies are influenced by the quantity and the quality of data used. Moreover new versions of those fields are an essential part of the

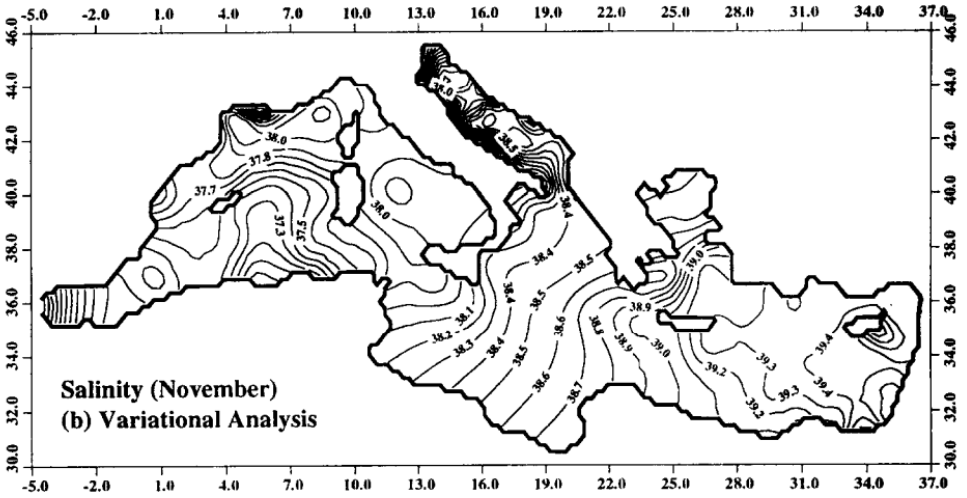

FIGURE 1.6: Salinity field at 10 m depth during November reconstructed from the variational inverse method.
Source: P. Brasseur *et al.* (1995)

numerous toolkits used by oceanographers, engineers, managers, navies, and authorities to monitor the ocean state and variability, to infer possible climate changes, and to initialize models. This fostered the need of historical multidisciplinary archive of observational data which would be otherwise difficult to find, and could possibly be lost. The Intergovernmental Oceanographic Commission began to foster international projects to compile exhaustive data sets and make them available to the entire scientific community with a standard format and quality assurance procedure. After some important programmes such as GODAR[4] (Global Oceanographic Data Archaeology and Rescue), and EU/MAST-MATER project [8] (Mass Transfer and Ecosystem Response financially supported by the Marine Science and Technology programme of the European Unit), the most representative and comprehensive project for the Mediterranean and Black Sea was MEDAR/MEDATLAS II (Mediterranean Data Archaeology and Rescue) that collected historical data from about 1890 to 2002. SeaDataNet (2006-today) is the evolution of MEDAR/MEDATLAS II. We will discuss it in the second chapter. The participants of MEDAR/MEDATLAS II are detailed in Figure 1.7.

The goal of MEDAR/MEDATLAS II was to gather, safeguard and make available to the entire scientific community a comprehensive data set of oceanographic parameters which includes, not only temperature and salinity but also dissolved oxygen, hydrogen sulfure, alkalinity, phosphate, ammonium, nitrite, nitrate, silicate, chlorophyll and pH, collected in the Mediterranean and Black Seas, through a wide co-operation of the Mediterranean and Black Sea countries.

[4]This project, presented by NODC, considerably increased the volume of historical oceanographic data about climate change and other researches, as well as of digitized data, and ensured their submission to national data centers and the World Data Center System

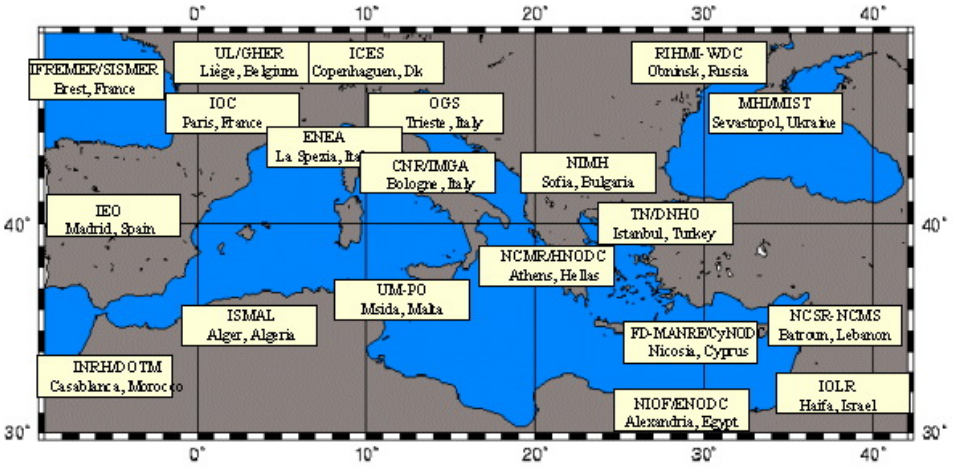

FIGURE 1.7: MEDAR/MEDATLAS partners.
Source: `http://medar.ieo.es/participantes_en.htm`

Furthermore the programme provided new observations for data-void areas in the Eastern and Southern parts of the Mediterranean Sea and Black Sea, employing a standard format(MEDATLAS), and a standard procedure for quality checking based on the international IOC, ICES and EC/MAST recommendations, with both automatic (objective) and visual (subjective) checks. The project also developed valuable products such as climatological gridded statistics and maps (Figure 1.8). Data and products were collected in an atlas available free of charge[5], that contains observed and analysed data, maps, software and documentation.

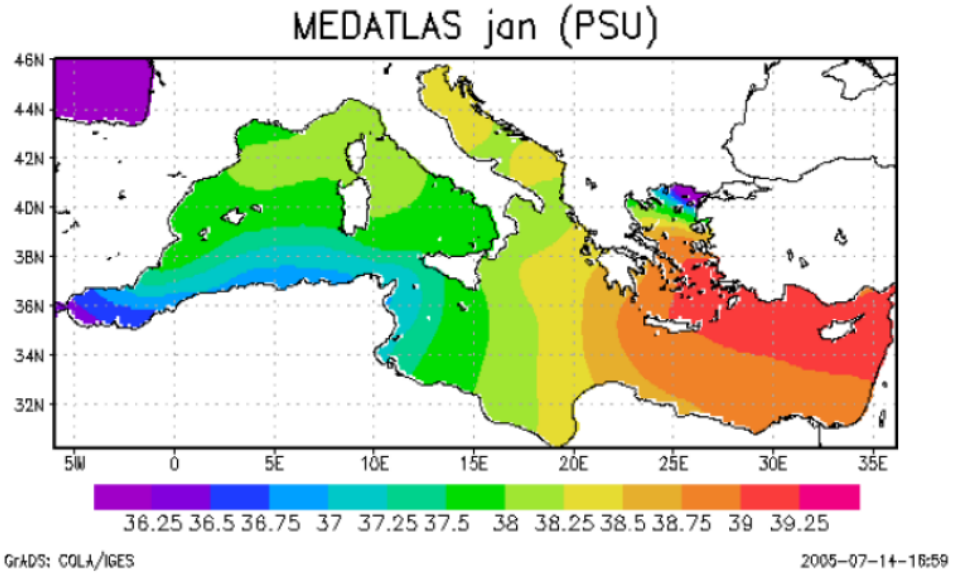

FIGURE 1.8: Example of salinity field of MEDAR/MEDATLAS data set.
Source: JRA5: Mediterranean products Data analysis protocol for the Mediterranean Sea

[5] `http://modb.oce.ulg.ac.be/medar` and on CD-Rom

1.2 Data sources

Over the years the sources of the ocean observations have changed and evolved. We can divide the platforms in two general classes:

- **in-situ platforms**;
- **satellite-based instruments**.

The former have been used by oceanographers for ages.They included surface and sub-surface moorings, profiling floats, research vessels and volunteer observing ships and gliders. The parameters measured by in-situ platforms are: temperature, salinity, pressure, dissolved oxygen, hydrogen sulfure, alkalinity, phosphate, ammonium, nitrite, silicate, chlorophyll and pH.

A mooring is a vertical wire anchored to the sea floor where scientific instruments can be attached and climb up and down the underwater wire. This platform measures a wide variety of surface and sub-surface variables including temperature, salinity, currents over long periods of time, and transmits the collected data to a satellite (Figure 1.9).

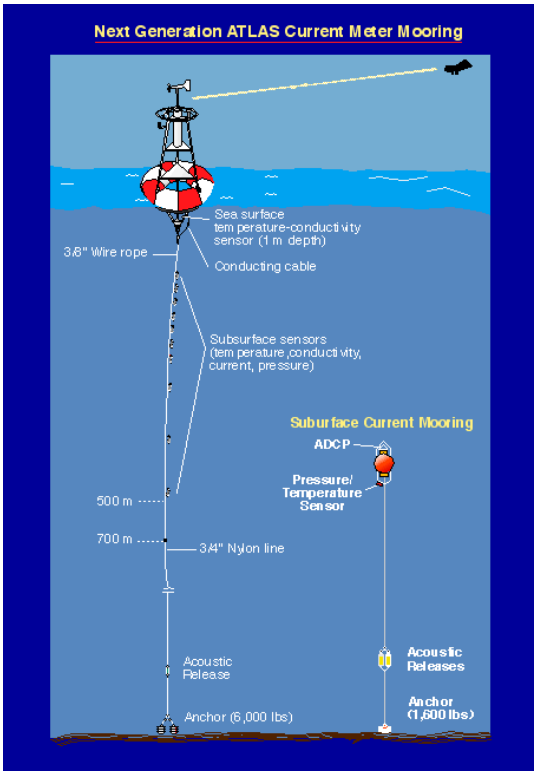

FIGURE 1.9: Prototype ATLAS moorings.
Source: `http://www.pmel.noaa.gov/tao/images/nxcur.gif`

A profiling float is a platform that changes its buoyancy by rising and descending in the ocean from sea surface to thousands meters in depth (Figure 1.10). This instrument mainly measures temperature and salinity; the data are transmitted via satellite (Figure 1.11). ARGO is a collaborative partnership of more than 30 nations from all continents that countes approximately 3600 drifting profiling floats deployed worldwide.

Research vessels deliver several high-accurate parameters (including chlorophyll-a and temperature) from sea surface to the ocean floor, but with intermittent spatial coverage. The most important instruments used on vessels and ships to measure temperature and salinity are: Niskin bottles, bathythermographs (MBT and XBT) and CTD.

The Niskin bottle is a tube, made of plastic, at both ends. Each end is equipped with a cap which is either spring-loaded or tensioned by an elastic rope (Figure 1.12). At a certain depth, both caps shut and seal the tube. The Niskin bottle is used to collect water samples from below the surface. A modern variation uses remotely controlled caps, making it possible to mount together, as many as 36 bottles, in a circular frame. This device is called rosette (Figure 1.13).

There are two types of bathythermographs:

- The mechanical bathythermograph (MBT) has a liquid-in-metal thermometer to measure temperature and a Bourdon tube sensor for pressure. Temperature measurements are imprinted on a coated glass slide by a mechanical stylus (Figure 1.14). The highest depth these instruments can reach is 300 m. These instruments were put out of service in the 80s.

- The expendable bathythermograph (XBT) is an instrument that measures temperature and is launched by research or commercial vessels. The XBT falls through the water from the surface to 750-1800 m below . The XBT is a probe composed of a thermistor connected electronically to a chart recorder, a wire and a shipboard canister (Figure 1.15). Oceanographers use fall-rate equations to calculate depth profiles:

$$z(t) = at^2 + bt \tag{1.1}$$

  where $z(t)$ is the depth in meters, t is the time, and a and b are empirical coefficients.

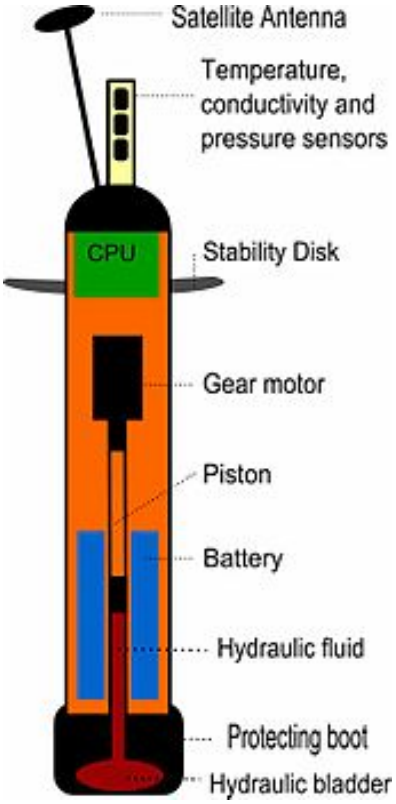

FIGURE 1.10: An ARGO profiling float.
Source: http://en.wikipedia.org/wiki/Argo_(oceanography)

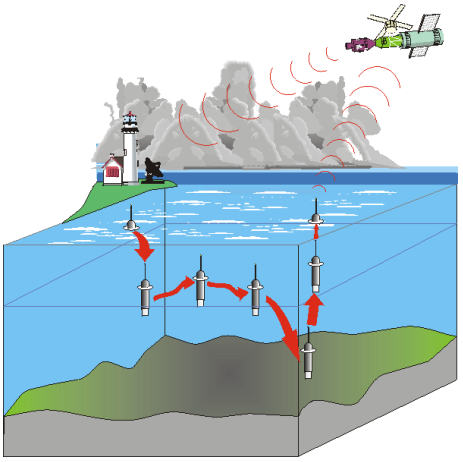

FIGURE 1.11: A profiling float system.
Source: http://www.ifremer.fr/dtmsi/images/produits/marvor/provor001.gif

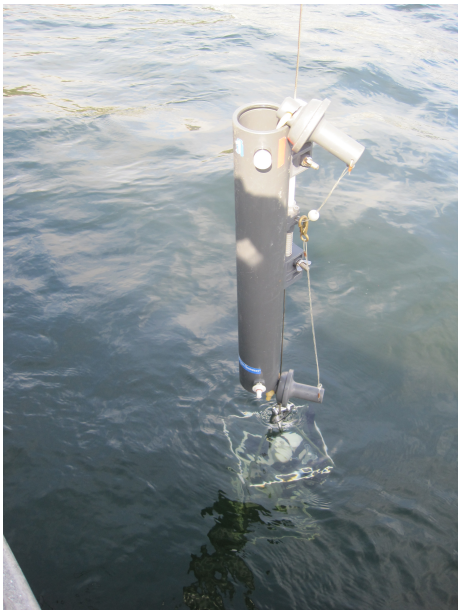

FIGURE 1.12: A Niskin bottle.
Source: http://courses.washington.edu/uwtoce12/methods/images/nisk3.jpg

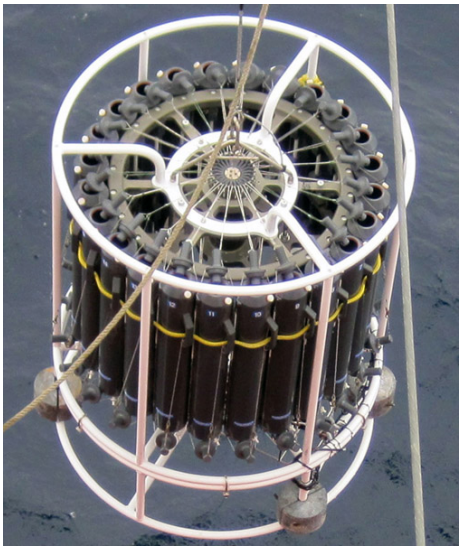

FIGURE 1.13: A rosette.
Source: http://continentalshelf.gov/missions/10arctic/logs/aug25/media/ctd0809_6475crds_600.jpg

CTD (Conductivity, Temperature, and Depth) is a set of sensors used to measure these three parameters; depth is assessed by hydrostatic pressure equation; and salinity by electrical conductivity (Figure 1.16). CTDs are usually mounted on a rosette and are lowered into the water on a wire to different depths. They transmit real-time data via a cable to a ship's computer.

Gliders are autonomous underwater vehicles (AUV) that change their bouyancy through volume changes to move vertically, and use an internal battery to propel themselves horizontally on a specific path (Figure 1.17 and Figure 1.18). The vertical range goes from 0 m to 1000 m. These instruments measure physical and biochemical parameters, and transmit data via satellite.

Satellite–based instruments have been developed since the 1970s. Those instruments are basically radiometers in different intervals of wavelength, (such as microwave or infrared region) and altimeters (Figure 1.19). The main parameters being measured are: Sea Surface Temperature (SST), salinity, dynamic height/altimetry, wind and sea state, and sea ice.

In this work we will use an *in situ* database for the analysis.

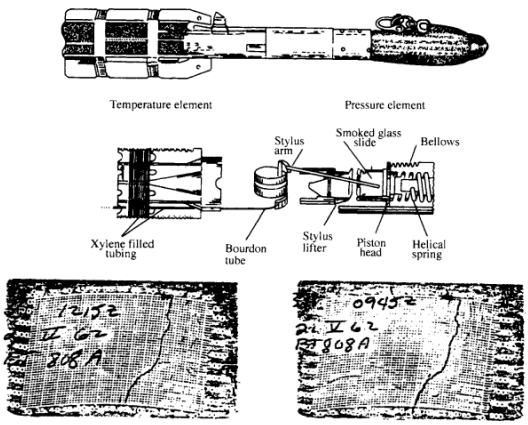

FIGURE 1.14: An MBT.
Source: Data Analysis Methods in Physical Oceanography - Emery, W. J. and Thomson, R. E.

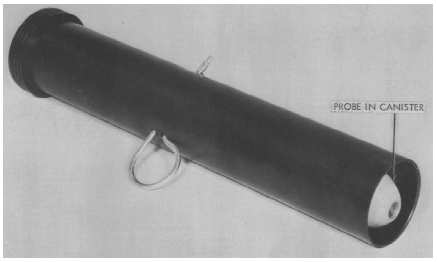

Fig. 1: XBT diagrams: Bathythermograph (probe) and exploded view.

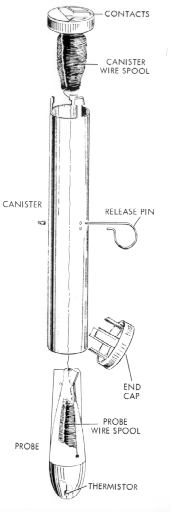

FIGURE 1.15: An XBT.
Source: `http://www.aoml.noaa.gov/phod/hdenxbt/xbtfigs2.gif`

FIGURE 1.16: CTD.
Source: `http://en.wikipedia.org/wiki/CTD_(instrument)#mediaviewer/File:CTD-me-details_hg.jpg`

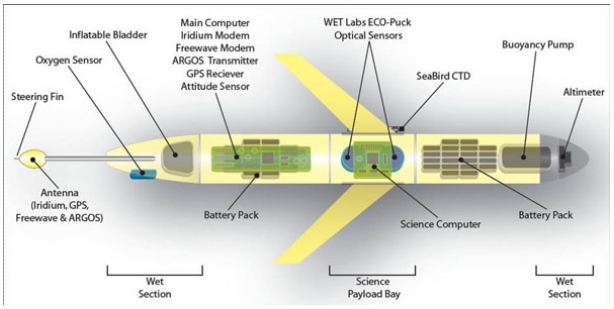

FIGURE 1.17: A glider.

Source: `http://imos.org.au/uploads/pics/Glider_structure.jpg`

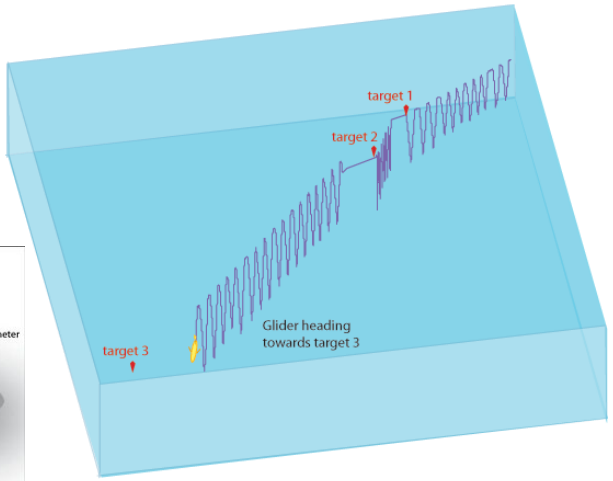

FIGURE 1.18: An example of a glider trajectory.

Source: `http://imos.org.au/uploads/pics/glider_path_01.gif`

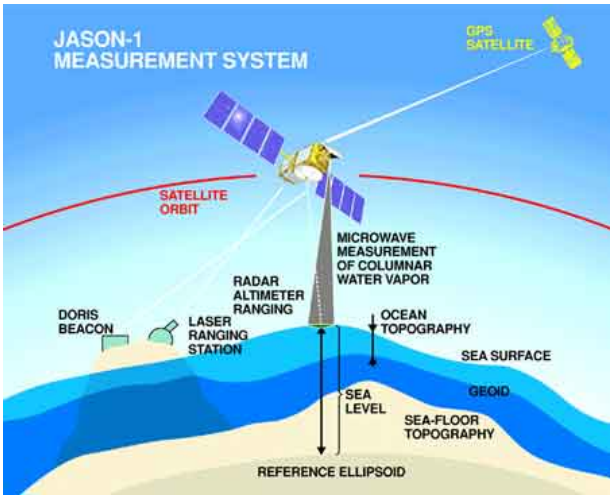

FIGURE 1.19: Altimetry satellite.

Source: `http://oceanworld.tamu.edu/students/satellites/images/altimetry_schematic_1.jpg`

Chapter 2

Data set description

In Chapter 1 we described international marine projects such as MEDAR/MEDATLAS that aimed to collect and share data for the entire community. We also stressed the importance of the quantity and especially the quality of the data sets in order to accurately reconstruct a climatological field. In this chapter we will introduce the project from which we obtained the data set we used to construct the climatological fields. We will discuss the spatial and temporal sampling of data and the standard principles of quality control.

2.1 SeaDataNet

The initial SeaDataNet (Pan-European infrastructure for ocean and marine data management) was lauched in 2006 to integrate historical, multidisciplinary data on a unique, standardized online data management infrastructure. SeaDataNet is coordinated by IFREMER (Institut Français de Recherche pour l'Exploitation de la Mer) and takes advantage of the collaboration of 40 European scientific marine research institutes from 35 different countries (Figure 2.1).

This project addressed the problem of the fragmentation of the marine scientific community: it allowed to manage and share data, coming from several scientific and research institutes along the coastlines of the European seas, by introducing common standards (metadata format, data format quality control methods, and quality flags). Furthermore this system allows users to find data, metadata, and products coming from different data centers through a unique integrated portal. The first part was completed in 2011 and SeaDataNet II started in the same year with

FIGURE 2.1: SeaDataNet partners.
Source: `http://www.seadatanet.org/Overview/Partners`

the aim to complete, extend and improve the previous work, starting from the number of data centers, which raised from 40 to 90.

The SeaDataNet II infrastructure is depicted in Figure 2.2.

The activities of the project are of three different types:

1. The Coordination activities (COORD) include the promotion and coordination of the entire infrastructure, data discovery, safeguard and improvement of existing data, and management of the standard catalogues. Those catalogues are metadata and data services that help users gather important information about marine organisations, research projects, and cruise reports. SeaDataNet II provides access to the following data sets:

    - European Directory of Marine Organisations (EDMO);
    - European Directory of Marine Environmental Data sets (EDMED);
    - European Directory of Marine Environmental Research Projects (EDMERP);
    - Cruise Summary Reports (CSR);
    - European Directory of the initial Ocean-observing Systems (EDIOS);
    - Common Data Index (CDI).

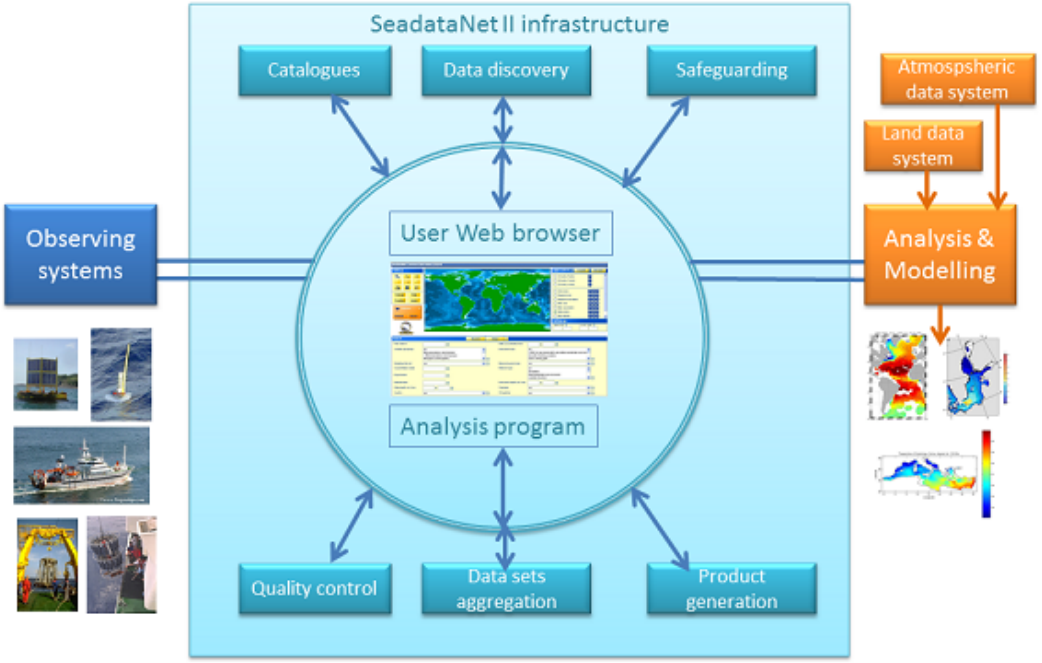

FIGURE 2.2: SeaDataNet 2 Infrastructure.
Source: `http://www.seadatanet.org/Overview/Context-and-Objectives`

2. The Support activities (SUPP) consist in the provision of metadata, data, aggregated data sets, and data products.

3. The Research activities (RTD) include the scientific control of the coverage and quality of the data sets, the generation of data sets aggregations, and products such as gridded fields of environmental parameters (to estimate their mean, seasonal variability and interannual trend), and visualing and analysing software (e.g. ODV, DIVA[1]).

Among the catalogues, the Common Data Index (CDI) is the most important for users because it is the direct interface between users and data sets. From this interface it is possible to search, request and download data, filtered by parameters, geographical region, instrument type and other criteria (Figure 2.3). The CDI Version 1 has been launched as pilot in 2008; the CDI Version 3, launched in 2013. can be found online[2].

The data sets are of three different formats:

[1]This software will be described in the third chapter
[2]`http://seadatanet.maris2.nl/v_cdi_v3/search.asp`

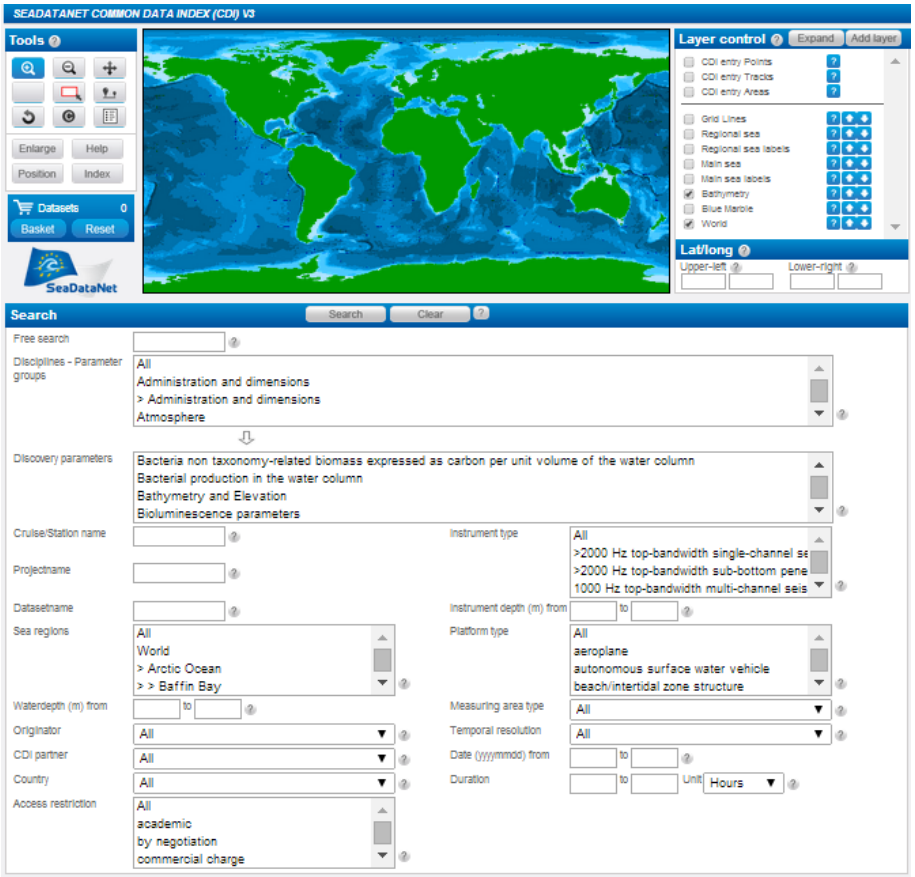

FIGURE 2.3: SeaDataNet Common Data Index (CDI).
Source: `http://seadatanet.maris2.nl/v_cdi_v3/search.asp`

- SeaDataNet ODV import format, a richer variant of the ODV[3] (Ocean Data View) version 4 generic spreadsheet format, including additional information.

- SeaDataNet MEDATLAS format, an autodescriptive ASCII format developed for hydrological vertical profiles by the MEDATLAS group in 1994 in conformity with the international ICES/IOC GETADE recommendations.[4]

- SeaDataNet Climate and Forecast (CF) NetCDF format, a machine-independent data format that supports "the creation, access, and sharing of array-oriented scientific data"[5] NetCDF uses the CF conventions for metadata.[6]

[3] `http://odv.awi.de/`
[4] `http://www.ifremer.fr/sismer/program/formats_phy/formats_UK.htm`
[5] `http://www.unidata.ucar.edu/software/netcdf/index.html`
[6] `http://cfconventions.org/`

2.1.1 Data gathering and processing

The data considered in this study are temperature and salinity profiles for the region of the Mediterranean Sea during the period 1900-2013. In order to have a more convenient and effective data access we decided to transfer the data into a MySQL database. This allowed us to:

- divide the data into thirteen standard regions (see Subsection 2.2.2);
- easily compute sums and statistical operations by means of a declarative query language (SQL);
- interpolate data for the final analysis (see Section 3.1);
- make additional quality controls on data and metadata (e.g. position/longitude/latitude of a profile).

In Figure 2.4 an informal workflow diagram is depicted. We used an ad-hoc Python script to populate a MySQL database with the data coming from SeaDataNet datasets. Two main tables were created: the first one, datarows, contains the profile metadata (Cruise, Station, Latitude, Longitude, DateTime, Instrument type, Local_Cdi_Id, Edmo_code, and Bathymetry); the second one, measurements, contains the actual data (Depth, Depth_qual, Temperature, Temperature_qual, Salinity, and Salinity_qual).

By means of another ad-hoc Python script, we created a third table with the interpolated values of temperature and salinity (see Section 3.1). Finally, DIVA and MATLAB were employed to create the tables, maps, and charts presented in this dissertation. The usage of DIVA for constructing the final climatological fields will be discussed in Chapter 3.

2.2 Data sampling

As already mentioned, the data set consists of temperature and salinity measurements collected during the XX century and in the first decades of the XXI century by 39 research institutes of different European countries, identified by the EDMO (Table 2.1) in the Mediterranean Sea. The database includes about 140900 hydrographic profiles, measured with different types of instruments. This is the main reason for the irregular vertical and spatial distributions:

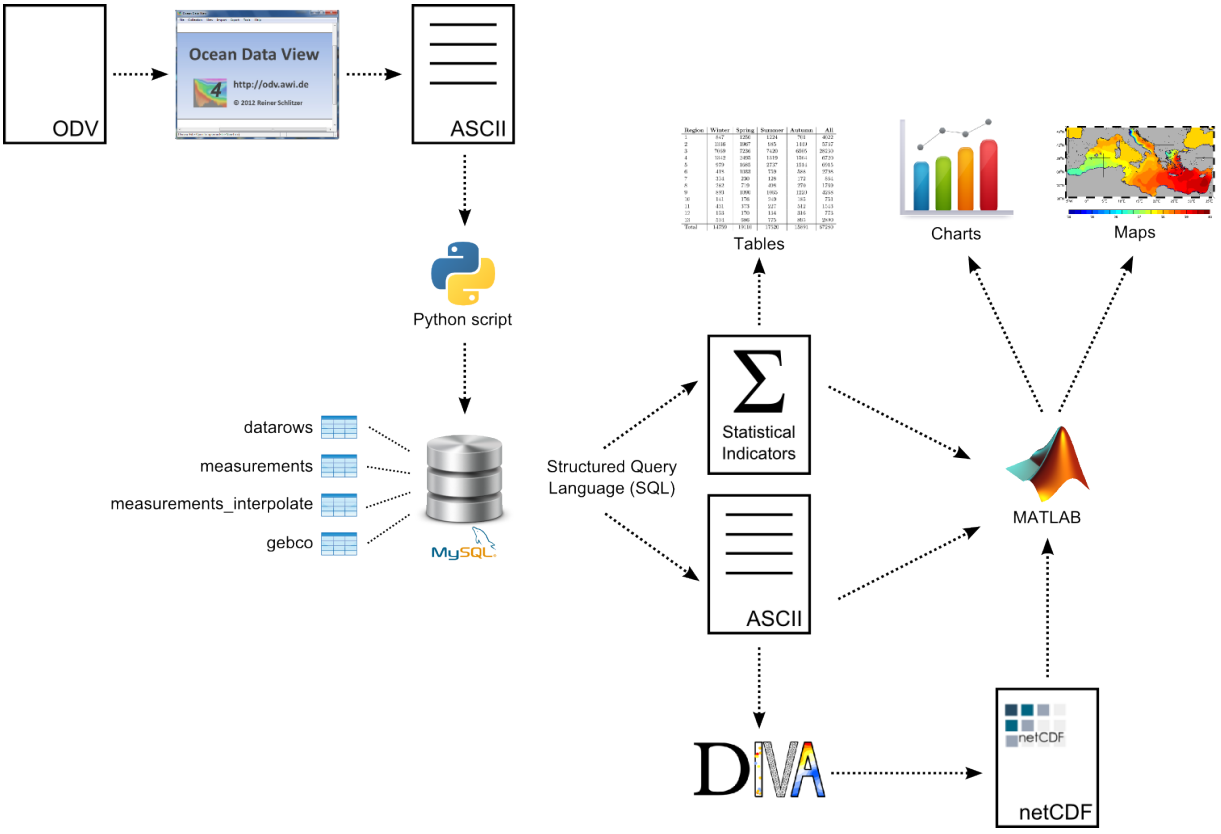

FIGURE 2.4: Work flow diagram.

- The vertical range is very different with respect to the instruments; for example XBT have a shorter vertical range with respect to ARGO profiling floats.
- The spatial coverage depends, not only on the countries resources but also on the sampling methods. In fact some data come from coastal monitoring, some profiles are sampled by scientific or commercial ships during their specific routes, whereas other profiles are sampled on specific grid.

Therefore it is important to focus on the description of the spatial and vertical distribution of the dataset, as we will show below.

2.2.1 Data time coverage

In this paragraph we present the time coverage of our dataset through the monthly, yearly, and seasonally number of profiles trends. First of all we count the number of profiles over years. Figure 2.5 shows the irregular distribution of data: there was a remarkable increase from the

EDMO	Institute	Profiles
43	British Oceanographic Data Centre (BODC)	13
108	CNR, Istituto di Scienze Marine (Sezione di Venezia - ex IBM)	4041
120	OGS (Istituto Nazionale di Oceanografia e di Geofisica Sperimentale)	6250
126	SACLANT Undersea Research Centre (SACLANTCEN)	489
127	CNR, Istituto di Scienze Marine (Sezione di Trieste)	1521
128	CNR, Istituto per lo Studio della Dinamica delle Grandi Masse	75
134	CNR, Institute of Marine Science U.O.S. of Pozzuolo di Lerici (SP)	2527
136	ENEA Centro Ricerche Ambiente Marino - La Spezia	8949
138	University of Genova - Laboratory of Marine Geology and Sedimentology	34
144	Institute of Marine Science (ISMAR) - Ancona	1134
145	Institute of Marine Science (ISMAR) - Bologna	142
149	ISAC - Institute of Atmospheric Sciences and Climate (Rome)	39
164	Hellenic Centre for Marine Research, Institute of Oceanography (HCMR/IO)	6070
234	Università degli Studi di Napoli 'Parthenope'	900
237	Stazione Zoologica Anton Dohrn of Naples	584
238	Marine Biology Laboratory of Trieste	643
269	Hellenic National Oceanographic Data Centre (HCMR/HNODC)	2128
353	IEO/Spanish Oceanographic Institute (IEO)	6250
486	IFREMER / IDM/SISMER	35560
540	SHOM (Service Hydrographique et Oceanographique de la Marine)	29234
630	NIOZ (Royal Netherlands Institute for Sea Research)	277
681	All-Russia Research Institute of Hydrometeorological Information (RIHMI)	7309
697	National Institute for Marine Research and Development "Grigore Antipa"	1
700	Institute of Oceanography and Fisheries (IOF)	1498
708	International Ocean Institute - Malta Operational Centre	307
710	Israel Marine Data Center (ISRAMAR)	29
711	Cyprus Oceanography Center (OC-UCY)	1548
730	International Council for the Exploration of the Sea (ICES)	68
731	Department of Navigation and Hydrography and Oceanography, Turkish Navy	288
802	Istanbul University, Institute of Marine Science and Management	23
840	Institute of Biology of the Southern Seas, NAS of Ukraine	1502
1130	ARPA Emilia-Romagna - Struttura Oceanografica Daphne	3965
1229	National Institute of Biology - NIBMarine Biology Station	1873
1232	Institut National des Sciences et Technologies de la Mer – INSTM	125
1338	Italian Navy Hydrographic Office	4445
1339	Commissione Permanente per lo Studio dell'Adriatico, Venezia	107
2432	Institute of Marine Biology (IMBK)	1
3234	Data Publisher for Earth & Environmental Science (PANGAEA)	84

TABLE 2.1: Data set institutes.

60s to 2013, with a spike in 2000. We decide to divided the data set in two periods: 1900-1987 and 1988-2013.

We also divided the dataset by instruments, period, and parameters to calculate the percentages profiles and measurements. Table 2.2 and Table 2.3 show those values. From 1910 to 1987 the number of casts is about 47.70% of the total, divided in 42.90% of MBT/XBT, and 57.10% of all other types of instruments (Figure 2.6). From 1988 to 2013 the number of profiles is about 52.30% of which 35.91% MBT/XBT, and 64.09% all other types of instruments (Figure 2.7). About 20% of measurements are collected in the first period and 80% in the second.

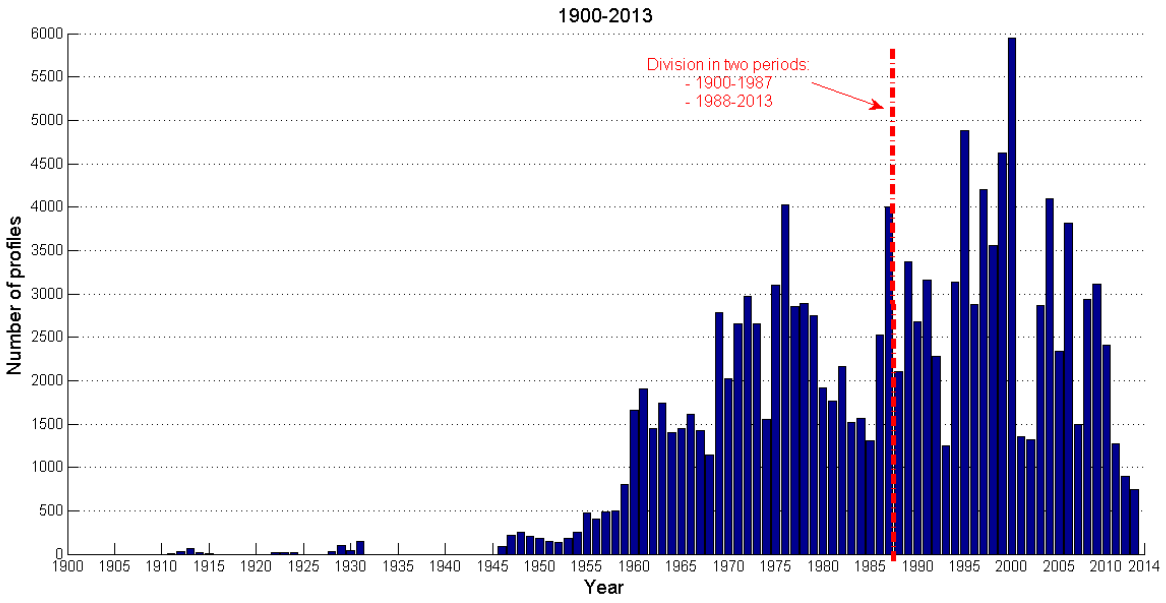

FIGURE 2.5: Numbers of profiles during years.

Period	MBT/XBT	Other instruments	All	Temperature	Salinity
1900-1987	28863	38417	67280	65955	36700
1988-2013	26461	47236	73697	71322	46885
Total	55324	85653	140977	137277	83585

TABLE 2.2: Data set casts divided for instrument.

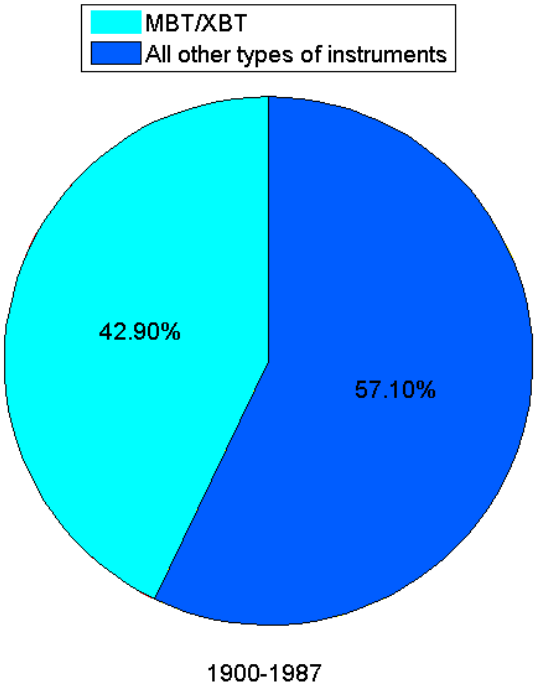

FIGURE 2.6: Percentages of types of instruments used from 1910 to 1987.

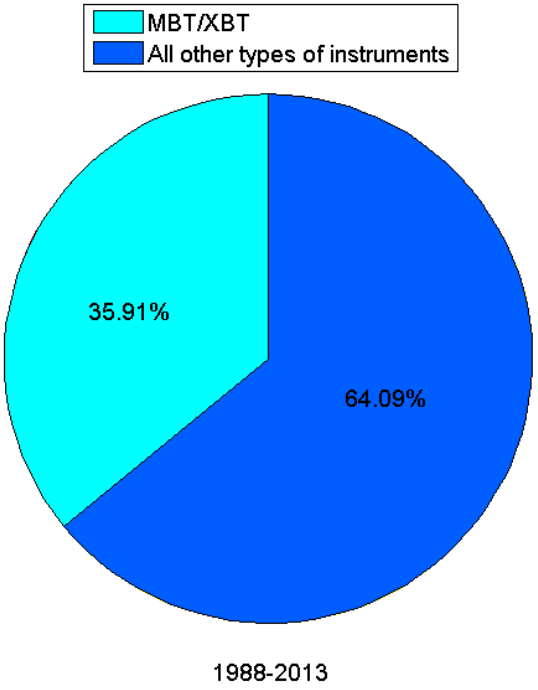

FIGURE 2.7: Percentages of types of instruments used from 1988 to 2013.

Period	**Temperature**	**Salinity**
1910-1987	4822425	4556855
1988-2013	20086756	11588552
Total	24909181	16145407

TABLE 2.3: Data set measurements.

The disparity between the number of profiles and measurements in the first period can be traced back to the instruments features, such as their low accuracy and short vertical range. The higher number of profiles is related to a progressive increase of observational programmes. Furthermore the numbers of MBT/XBT profiles in the second period are smaller than in the first because the MBT were put out of service in the 80s.

The monthly distribution of profiles is shown in Figure 2.8. As one can notice there is a seasonal trend in both periods. During the first three months of the year the number of profiles increases; in April we have a small decrease and an immediate increase in May. During summer we can see a smooth decline from June to August, a small increase in September, that continue in October, and another slow decrement from November to December.

Those month and year distributions are probably due to the need to monitor some seasonal processes that occurred in specific periods, such as the deep water formation occurring in February in the Gulf of Lions, or interannual variabilities that typically produce important changes in the

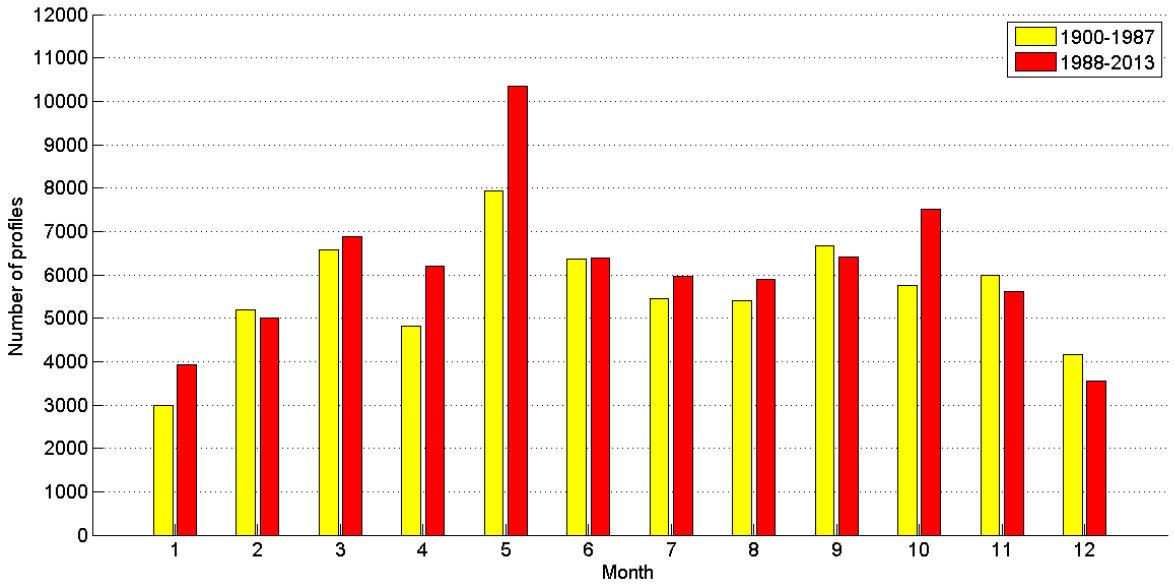

FIGURE 2.8: Month distribution.

major properties of the Mediterranean Sea [9]. An important example is the Eastern Mediterranean Transient (EMT) occurred between the end of the 80s and the start of the 90s.[10] This event is the reason for the increase of the Water Mass Formation rate, particularly in the Eastern basin, and for the increase of the salinity values, occurred first in the Eastern basin and later in some areas of the Western Mediterranean.[11]

2.2.2 Data spatial coverage

In this paragraph we focus on the horizontal and vertical coverage of the data divided by parameters, standard region and periods. As seen in Figures 2.9, 2.10, and 2.11, the horizontal distribution of station data is inhomogeneous too, in that some areas are more sampled than others. In particular we can find a larger number of profiles in the Western than in the Eastern Mediterranean. Furthermore, as shown in Figure 2.12 and Figure 2.13 there are more temperature casts with respect to salinity in general.

To make a more detailed analysis, we divided the Mediterranean Sea in 13 regions, represented in Figure 2.14. The Western Mediterranean includes the regions 1-2-3-4, and the Eastern Mediterranean the regions 5-6-7-8-9-10-11-12-13. In the Eastern part, the Levantine basin has been divided in 4 areas (10,11,12,13), because of its large dimensions.

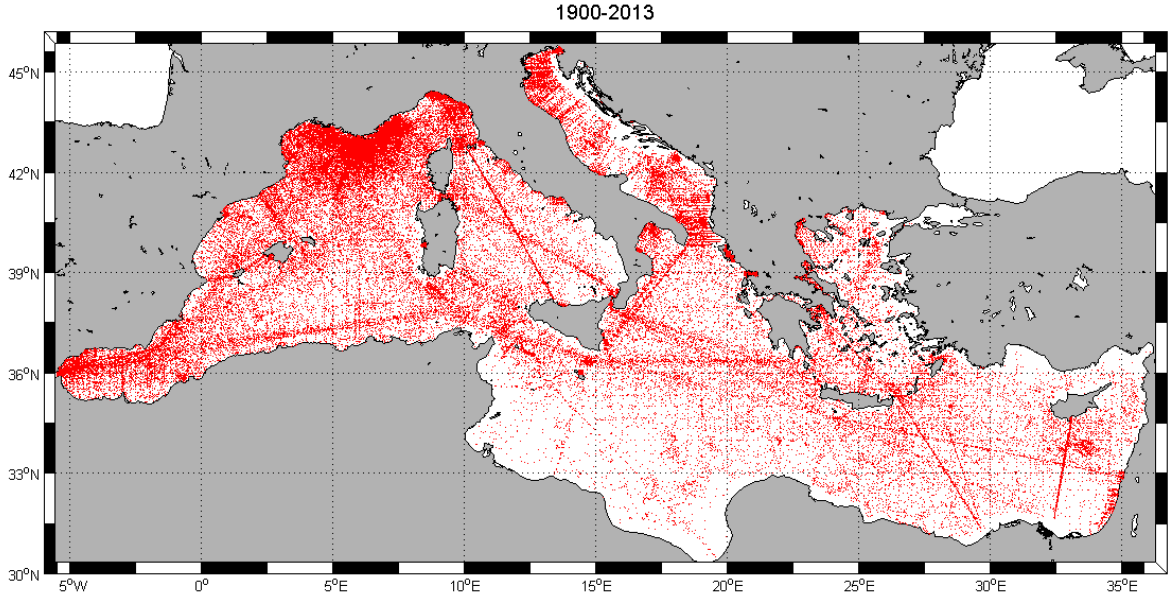

FIGURE 2.9: Location of temperature and salinity profiles from 1910 to 2013.

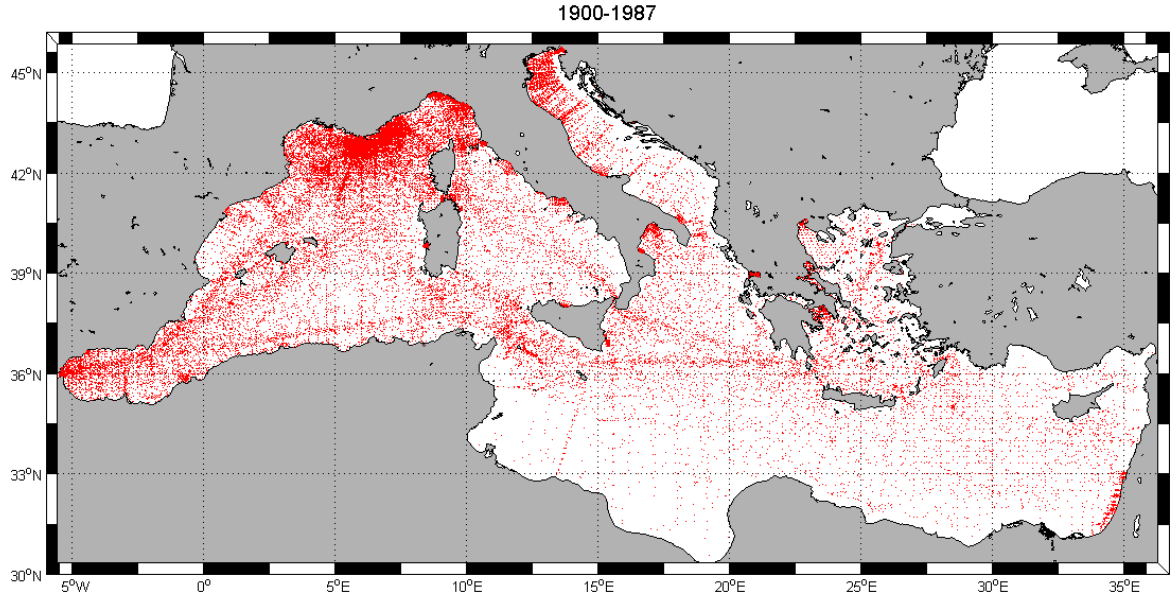

FIGURE 2.10: Location of temperature and salinity profiles from 1910 to 1987.

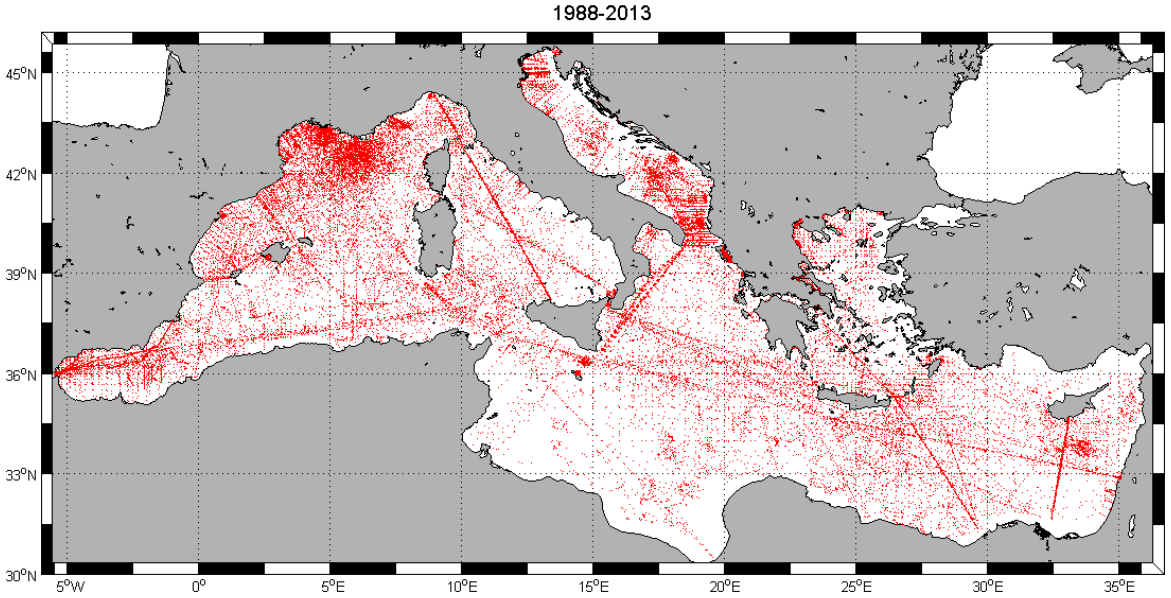

FIGURE 2.11: Location of temperature and salinity profiles from 1988 to 2013.

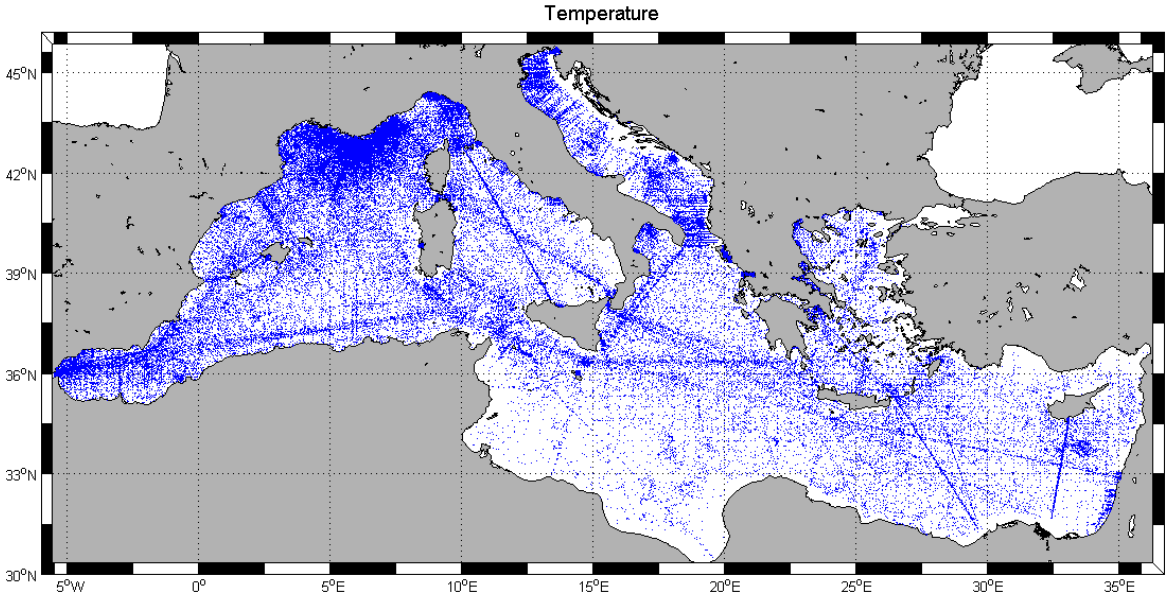

FIGURE 2.12: Location of temperature profiles from 1910 to 2013.

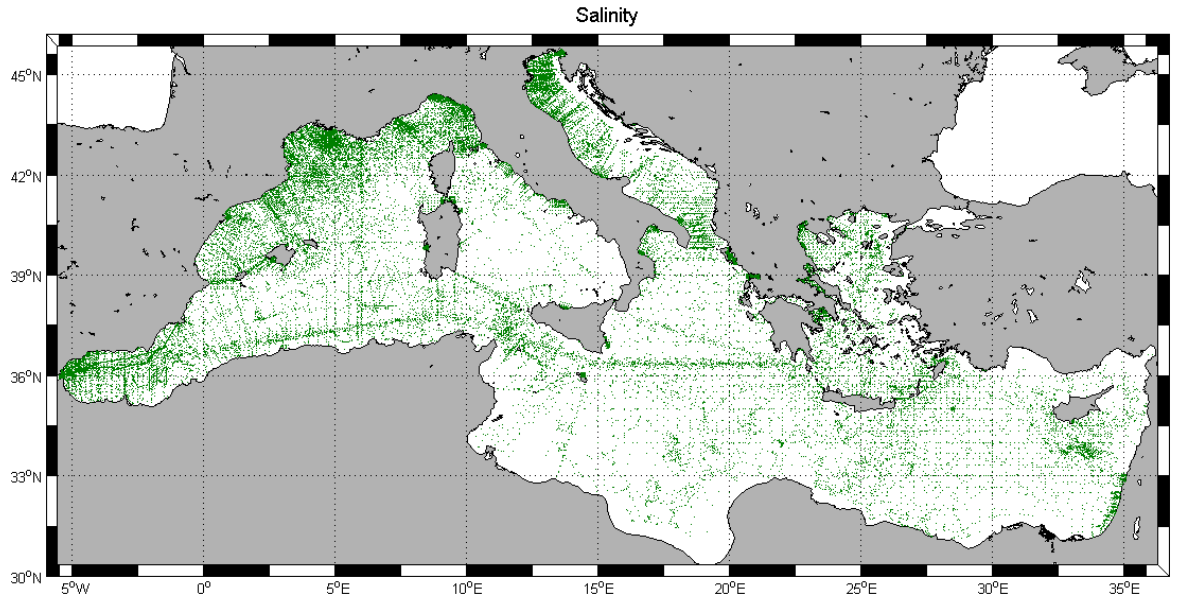

FIGURE 2.13: Location of salinity profiles from 1910 to 2013.

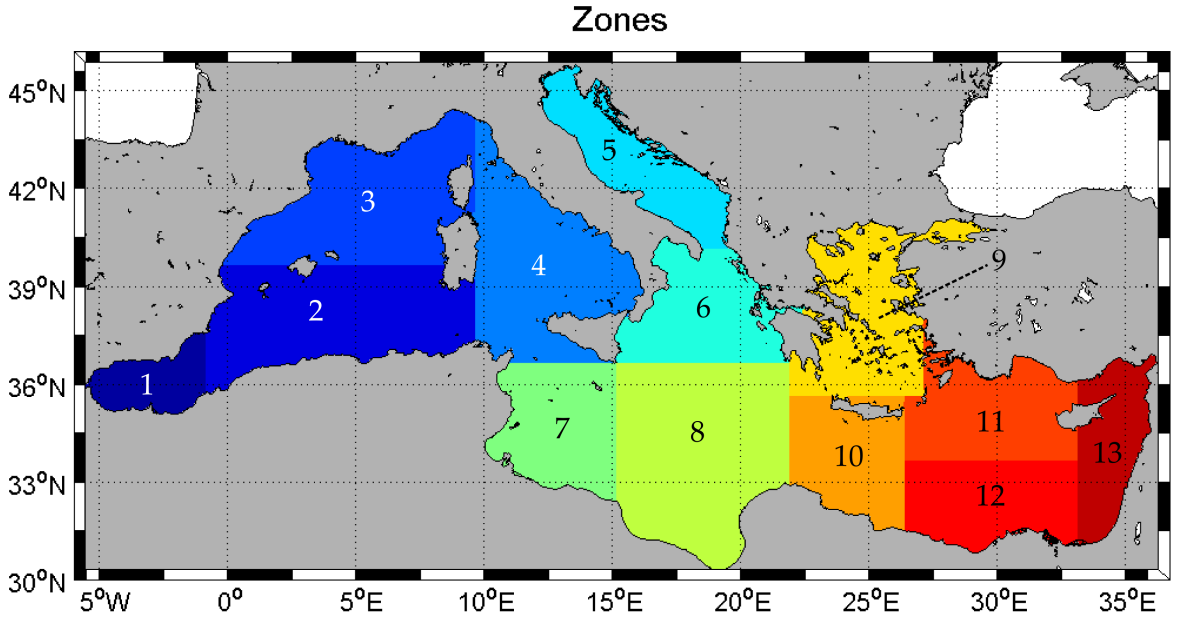

FIGURE 2.14: Regions of the Mediterranean Sea.

We also calculate the percentages of number of profiles per region and period. Figure 2.15 shows the percentages of number of profiles for each region with respect to the total casts. Figure 2.16 and Figure 2.17 show the percentages of the casts for each region in the period 1910-1987 and the period 1988-2013, respectively. As it can be seen, what was qualitatively revealed by the maps is confirmed by the numbers.

In the Western basin we generally find higher percentages, in particular in zone 3 (Gulf of Lions), than the Eastern basin. We calculate about 56% of casts for the West and 44% for the East over the total period (see Figure 2.15. We calculate about 66% for the West and 34% for the East in the first period (see Figure 2.16), and about 48% for the West and 52% for the East in the second period (see Figure 2.17). The latter result is related to an increase of the experiments conducted in particular in the Levantine and Adriatic basins. Furthermore there is a decrease of percentages in region 3. Among the Eastern regions, the Adriatic Sea and Aegean Sea (zone 5 and 9, respectively) have a more dense coverage of casts. The Tunisian basin (zone 7) remains the region with the lowest number of profiles, also for deep/bathimetric reasons.

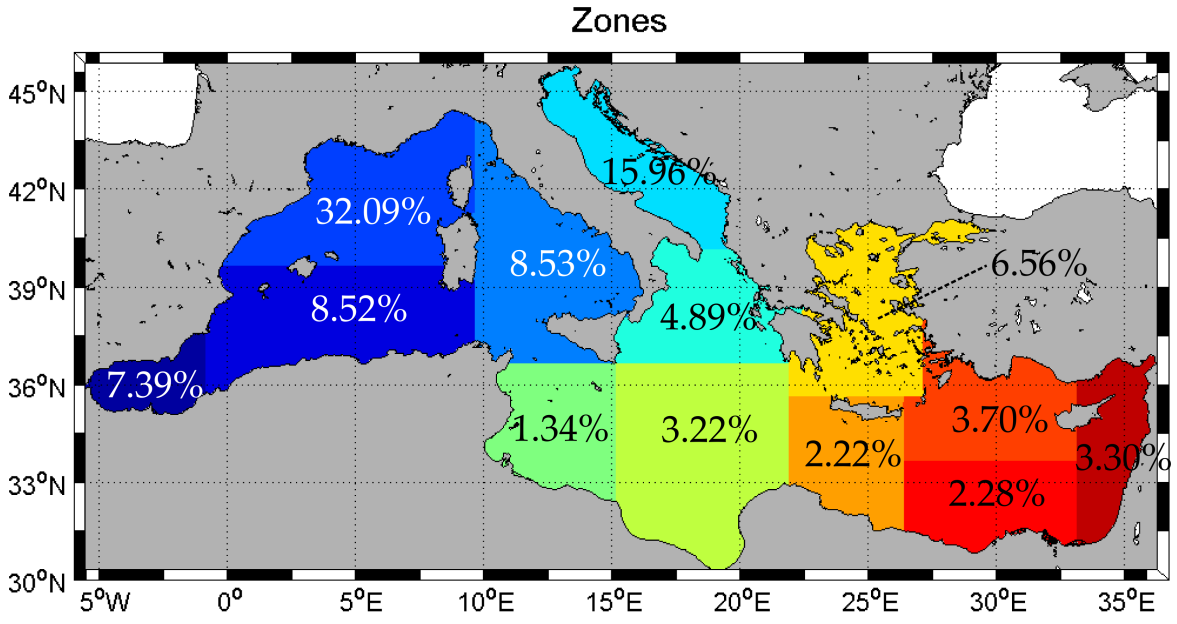

FIGURE 2.15: Percentages of the total casts for each region.

For a more specific analysis we present the distribution of the number of casts divided by season and region. In Table 2.4 and Figure 2.18 we present the distribution of profiles by regions and seasons (in the period 1910-1987). The general trend, illustrated above, is respected. However, no trend can be identified with respect to the seasons, in that each region presents a distinct

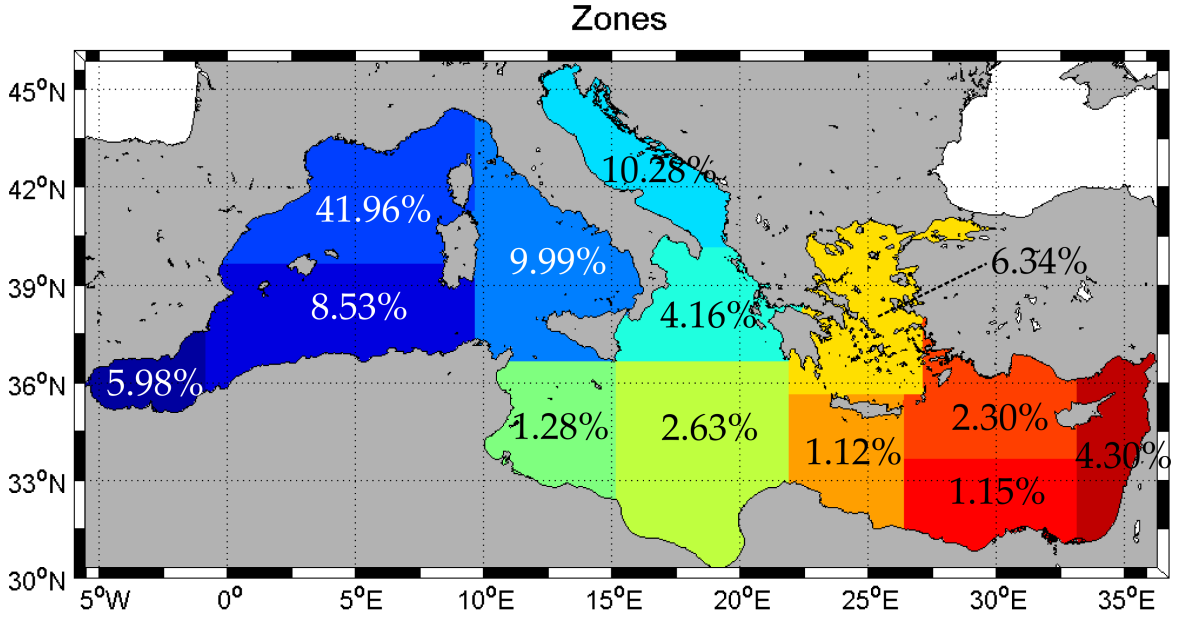

FIGURE 2.16: Percentages of profiles for each region in the period 1910-1987.

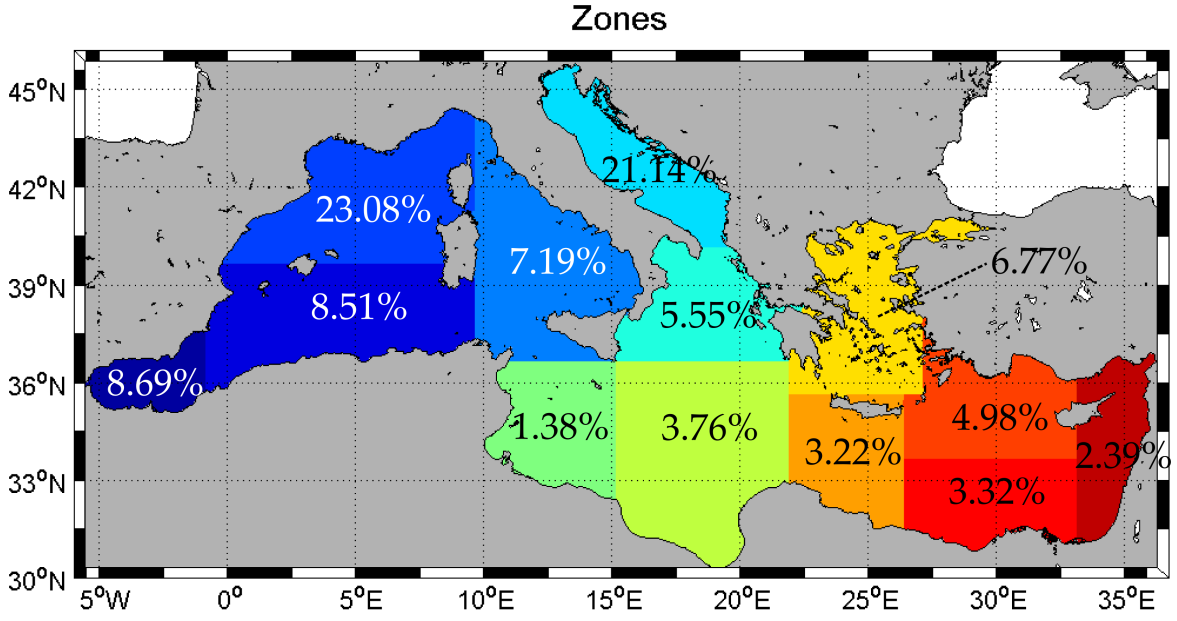

FIGURE 2.17: Percentages of profiles for each region in the period 1988-2013.

distribution. On the whole, the greatest number of casts and the highest number of maxima for regions are seen in spring.

Region	Winter	Spring	Summer	Autumn	All
1	847	1250	1224	701	4022
2	1336	1967	985	1449	5737
3	7069	7236	7420	6505	28230
4	1342	2495	1319	1564	6720
5	979	1685	2737	1514	6915
6	418	1033	759	588	2798
7	334	230	128	172	864
8	282	719	498	270	1769
9	893	1090	1065	1220	4268
10	141	176	249	185	751
11	431	373	227	512	1543
12	153	170	134	316	773
13	534	686	775	895	2890
Total	14759	19110	17520	15891	67280

TABLE 2.4: Number of temperature and salinity profiles by seasons and regions from 1910 to 1987.

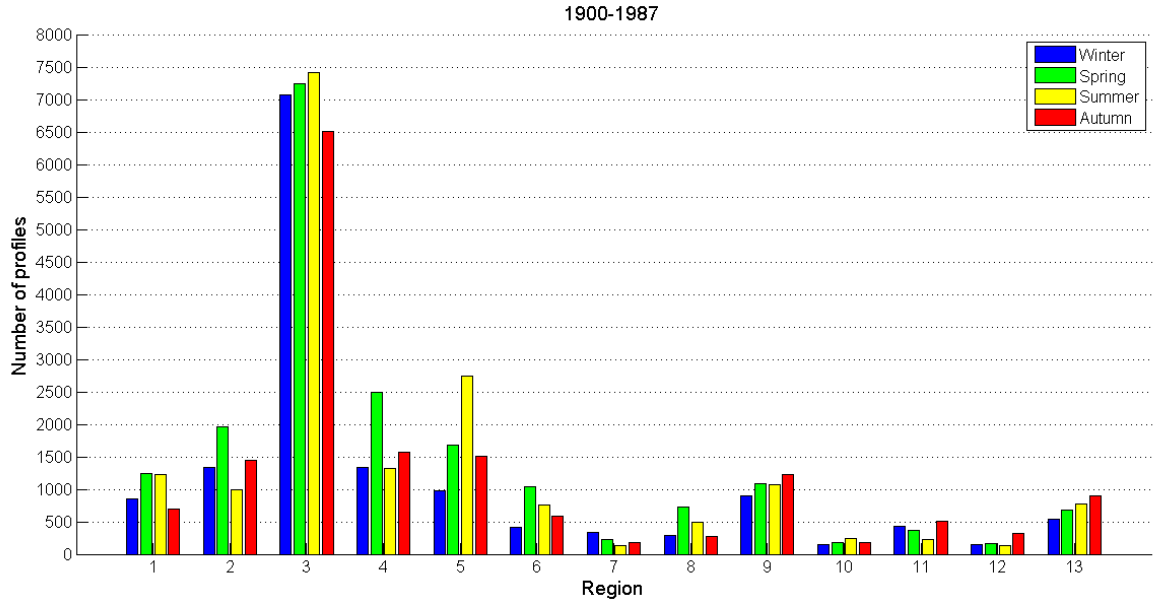

FIGURE 2.18: Number of casts for seasons and regions from 1910 to 1987.

Table 2.5 and Figure 2.19 show the number of profiles by regions and seasons from 1988 to 2013. Also in this period there is no regular regional trend. The season with maximum casts is summer and the highest number of maxima occurs in autumn.

Region	Winter	Spring	Summer	Autumn	All
1	473	2020	2877	1031	6401
2	1404	2059	1455	1355	6273
3	3547	6670	3525	3268	12399
4	1237	1453	1051	1561	5302
5	3131	4796	3799	3856	15582
6	1142	1079	617	1255	4093
7	168	307	324	219	1018
8	564	712	768	730	2774
9	1609	1242	1418	717	4986
10	505	503	811	556	2375
11	966	933	750	1022	3671
12	529	644	511	764	2448
13	527	540	358	339	1764
Total	15802	22958	18264	16673	73697

TABLE 2.5: Hydrological casts divided for seasons and regions from 1988 to 2013.

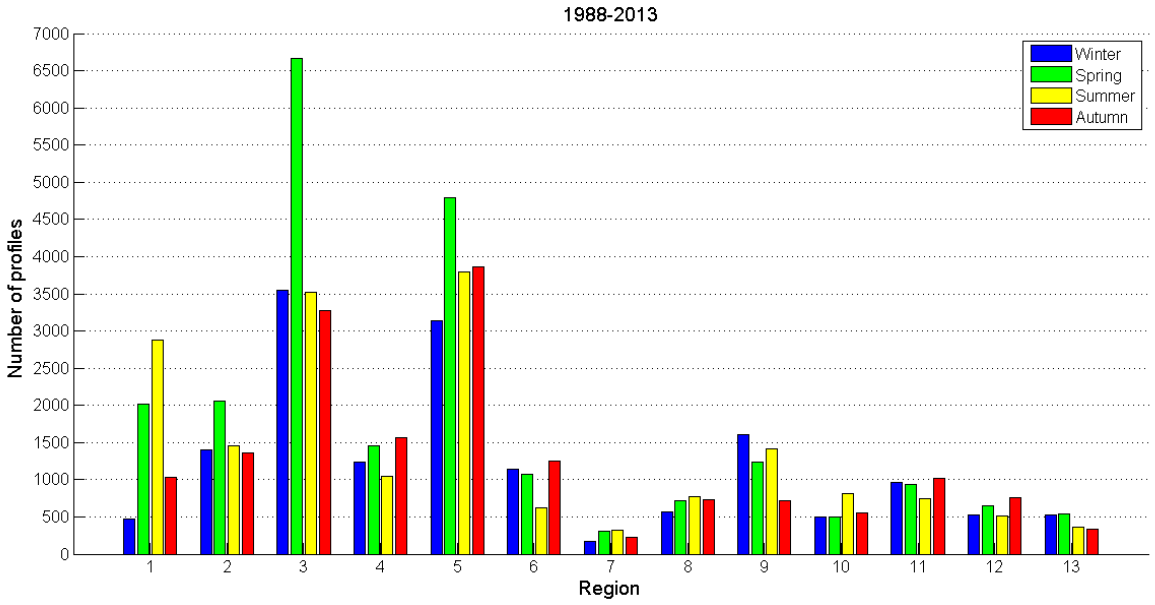

FIGURE 2.19: Number of casts for seasons and regions from 1988 to 2013.

2.2.3 Data vertical distribution

In this section we focus on the vertical coverage divided by region, basin, parameter, and season. This analysis is important for the final results because the accuracy of climatological fields is strictly related to the number of measurements presented in the evaluated levels, as we will discuss in SubSection 4.1.3.

Figure 2.20 shows the distributions of temperature measurements in the Western Mediterranean divided in its four regions(specified in Subsection 2.2.2). Region 1, 2, and 4 present similar

distribution: the greatest number of measurements can be found at depths between 0 and 750m . Region 3 is, as usual, the region with the highest number of temperature measurements. In fact the the depths in which we have the greatest number of measurements in this region are the ones between 0 and 1500m. The region having the measurements at highest depth is the fourth because it is the region with the deepest bathymetry. Figure 2.21 shows the distribution of salinity measurements in the Western Mediterranean. Again regions 1, 2, and 4 present the same trend, and the greatest number of measurements is concentrated between 0 and 750m. Also in this case, region 3 has the highest number of measurements.

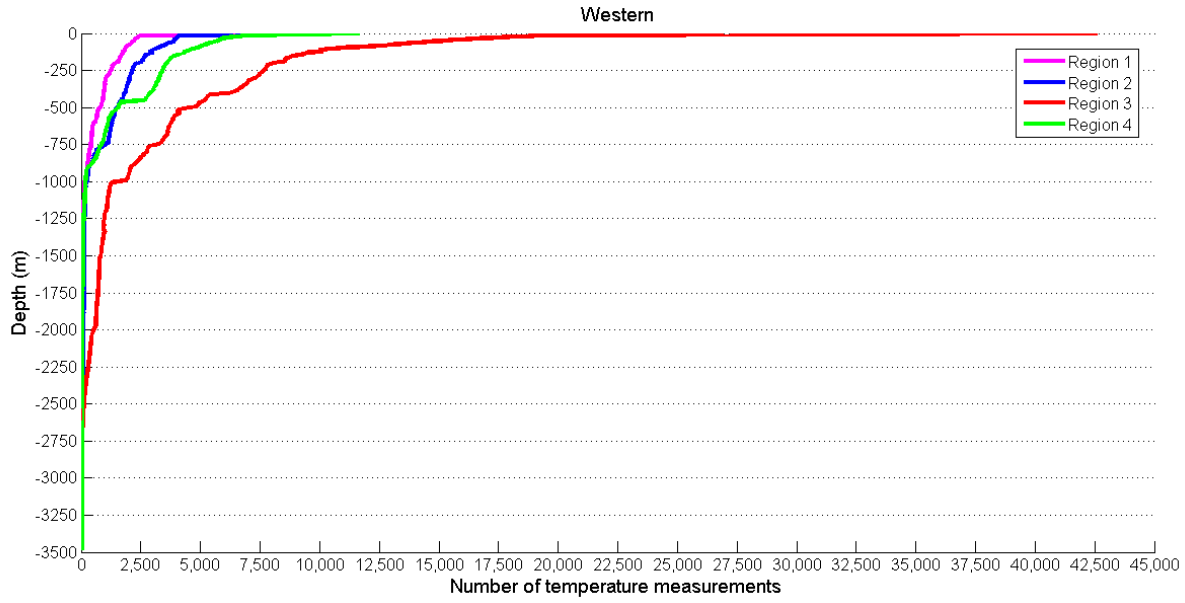

FIGURE 2.20: Western Mediterranean: Number of temperature measurements with respect to depth.

Figure 2.22 shows the distributions of temperature measurements in the Eastern Mediterranean divided in its nine regions(specified in Subsection 2.2.2). The distribution of measurements is similar for all regions, and the major number of measurements is between 0 and 750m. Zone 7 is the one with the smallest number of measurements. Zone 8 is the region with the measurements at the highest depth. Figure 2.23 shows the distributions of salinity measurements in the Eastern Mediterranean. Salinity present the same characteristics of temperature distributions, but the total number of measurements is smaller.

Let us now considered the seasonal trends of temperature and salinity measurements in the entire Mediterranean region. Figure 2.24 shows the number of seasonal temperature measurements trend. All the seasonal distributions present the same decreasing trend with respect to depth.

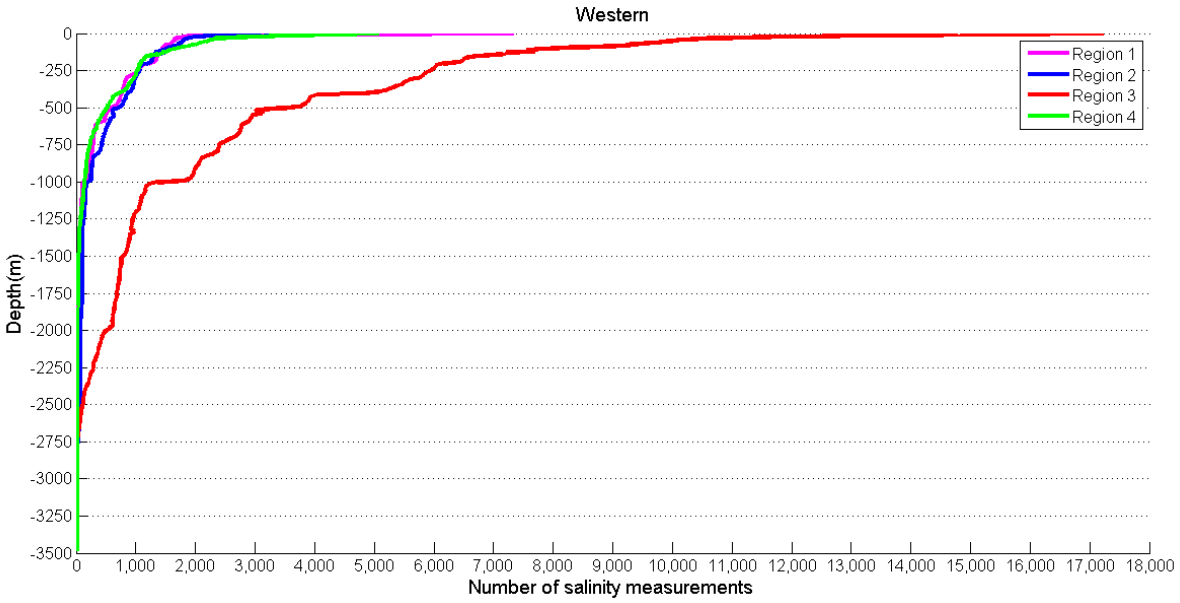

FIGURE 2.21: Western Mediterranean: Number of salinity measurements with respect to depth.

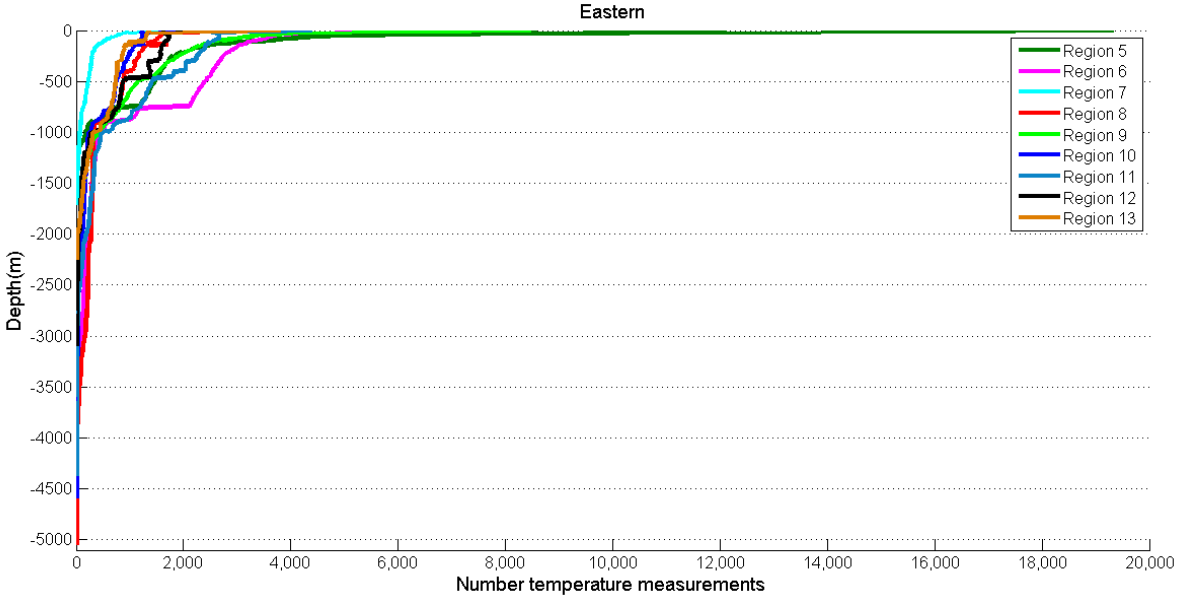

FIGURE 2.22: Eastern Mediterranean: Number of temperature measurements with respect to depth.

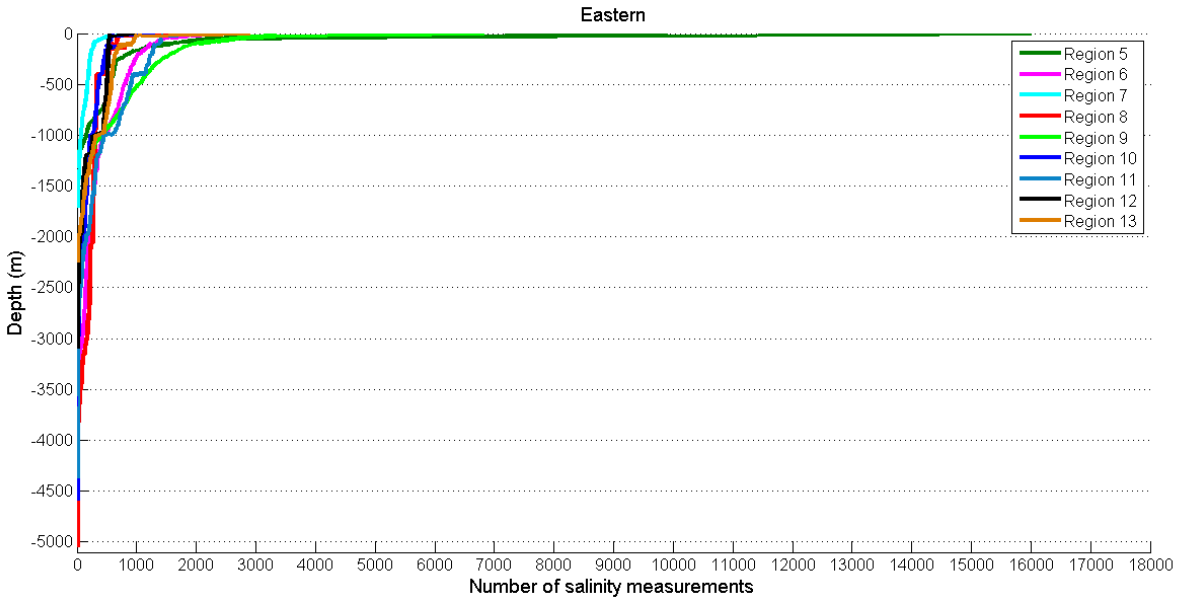

FIGURE 2.23: Eastern Mediterranean: Number of salinity measurements with respect to depth.

This decrease with depth is confirmed by the percentages presented in Table 2.6. We calculated the percentages for all seasons dividing the range depth in five major intervals. For all cases the first interval has the highest value of about 65% and the last interval has the smallest value. In autumn and summer, the percentages of the last interval are higher than in the other season, as shown in Figure 2.24.

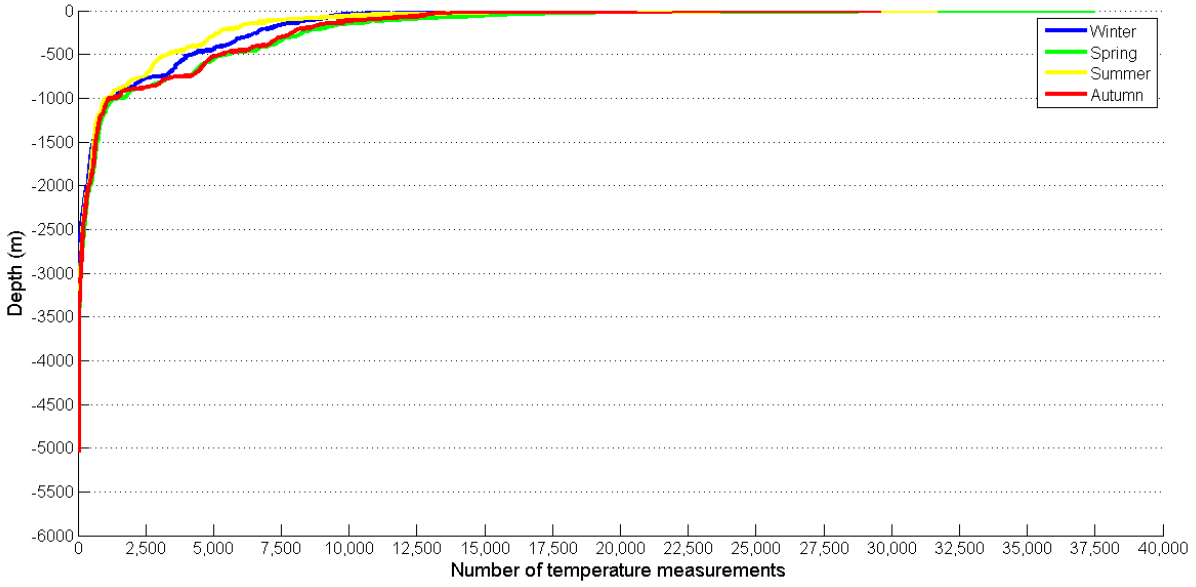

FIGURE 2.24: Number of temperature measurements with respect to depth and season.

Figure 2.25, the salinity trends for all the seasons, present the same decreasing tendency, as

Interval of depth (m)	Winter	Spring	Summer	Autumn
0 - 500	64,98%	65,84%	65,05%	64,26%
500 - 1000	22,76%	21,82%	19,99%	23,35%
1000 - 1500	6,29%	5,59%	6,67%	5,58%
1500 - 2000	3,64%	3,65%	4,48%	3,69%
Depth $>$ 2000	2,33%	3,10%	3,81%	3,12%

TABLE 2.6: Percentages of temperature measurements per interval of depth.

temperature. In Table 2.7, we show the percentages of salinity measurements divided by season and interval of depth. Also in this case the percentage values confirm that measurements tend to decrease with depth, and in summer and autumn we find the highest percentages.

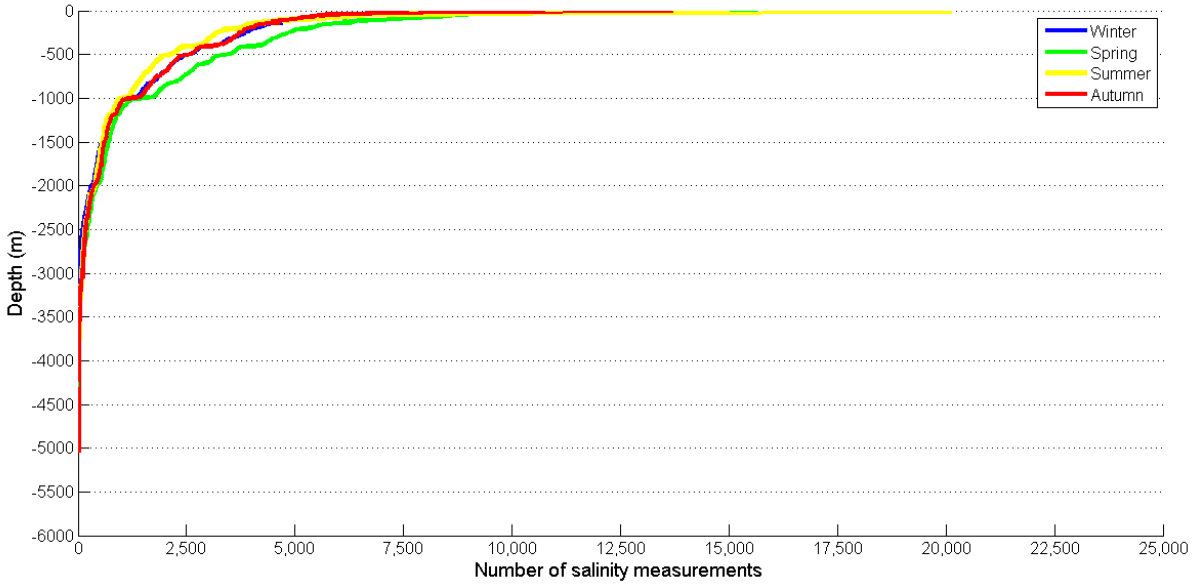

FIGURE 2.25: Number of salinity measurements with respect to depth and season.

Interval of depth (m)	Winter	Spring	Summer	Autumn
0 - 500	58,38%	58,69%	59,48%	58,60%
500 - 1000	23,30%	22,67%	19,78%	19,78%
1000 - 1500	9,41%	8,40%	9,20%	9,20%
1500 - 2000	5,43%	5,53%	6,18%	6,33%
Depth $>$ 2000	3,48%	4,71%	5,36%	6,09%

TABLE 2.7: Percentages of salinity measurements per interval of depth.

2.3 Quality Control procedure

As said before, one of the fundamental requirements of a successful data analysis is the quality of the data set. All the SeaDataNet data centers carry out a Quality Control of the collected data before developing them. The Quality Control procedure, in accordance with the IOC (Intergovernmental Oceanographic Commission) and ICES (International Council for the Exploration of the Sea), has standard automatic and human monitoring tests of instruments and parameters.

The QC procedure applies not only to data but also to metadata. Three main kinds of test are conducted:

1. **Check of the Format**: points out wrong platform codes or names, parameter names or units, missing compulsory information like cruise, observation system, or sensor type.
2. **Check of the location and date** which can be further distinguished in:
    - **Duplicates test**.
    - **Date and time test**: controls whether the date and time format are correct (Year 4 digits, Month 1/12,Day 1/31, Hour 0-23, and Minute 0-59).
    - **Longitude and latitude test**: controls whether the range of the coordinates (the former from -180 to 180 and latter from -90 to 90) is correct.
    - **Position test**: requires that the geographical coordinates must not be on land.
3. **Check of the measurements**: these tests typically vary according to the parameters and instruments used; however three general tests apply to any parameter and instrument:
    - **Global range test**: controls whether the parameter measurements are in the appropriate range of the ocean.
    - **Regional range test**: controls whether the regional values fall within the typical extremes of each particular region.
    - **Deepest pressure test**: controls whether pressure values exceed the bathymetry value.

Now we introduce specifically the QC procedure for vertical profiles. In this procedure, the **Ship Velocity test** is added to the general location and date tests.

The Ship Velocity test consists in calculating the ship velocity through the distance and time interval between two consecutive stations. If the value is less than tha maximum standard ship speed, the position is good. If the position is wrong it is possible correct it by interpolation [12].

The measurement tests for vertical profiles are:

- Global range test (as above).
- General malfunction test: permits to check whether the profile is constant (if so some sensor was jammed), and the presence of at least two parameters (vertical and measurement value).
- Pressure trend checks whether pressure increases monotonically.
- Regional range test (as above). The regions considered are specified in MEDAR/MEDALTAS project (see Figure 2.26).
- Deepest pressure test (as above).
- Spikes detection test: identifies the spikes on profile values. The IOC algorithm requires at least three consecutive good values and considers the difference in value for regulary spaced data (e.g. CTD):

$$\left| \frac{V_2 - (V_3 + V_1)}{2} - \frac{\mid V_1 - V_3 \mid}{2} \right| \; > \; \text{THRESHOLD VALUE.} \tag{2.1}$$

  For irregular spaced data (e.g. Bottles) the algorithm considers the difference in gradients:

$$\left| \left| \frac{(V_2 - V_1)}{(P_2 - P_1)} - \frac{(V_3 - V_1)}{(P_3 - P_1)} \right| - \left| \frac{(V_3 - V_1)}{(P_3 - P_1)} \right| \right| \; > \; \text{THRESHOLD VALUE.} \tag{2.2}$$

- Narrow range test: compares the profile values with the previous climatologies for the region by linear interpolation at the level of the observation. If the value differs from the climatological point more than:
  - 5 × Standard Deviation[7] over the shelf (depth $<$ 200 m);
  - 4 × Standard Deviation at the slop and straits region (200 m $<$ depth $<$ 400 m);
  - 3 × Standard Deviation at the bottom (depth $>$ 400 m)

[7] In Physical oceanography Standard Deviation represents the natural variability of system. For this reason the SD range of values changes with respect to depth.

the point is marked as 'outlier'.

- Density inversion test: permits to identify wrong values of temperature and salinity by the UNESCO equation of state for sea water[13].

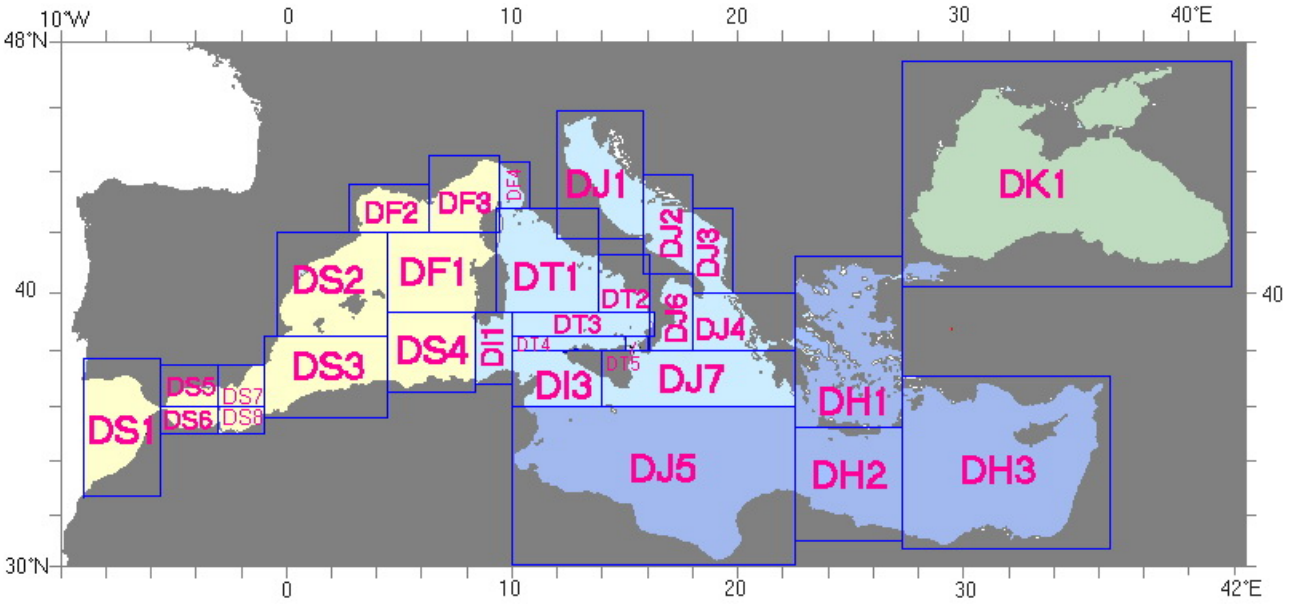

FIGURE 2.26: Regions used for the Regional range test.

The general goal of a Quality Control is to assign a quality flag to each value of the data set to indicate its degree of reliability, as well as the possible points of error. The data values are not modified. SeaDataNet adopted the QC flag scale introduced by the GTSPP (Global Temperature and Salinity Profile Programme) project[8] with some addictions (Figure 2.27).

In Table 2.8 we present, in percentages, the Quality Flag values of temperature, salinity, and depth measurements of our dataset. As can be noted, most values have the 'good' flag, about 95% for temperature and %57 for salinity. Only the salinity shows a high number of missing values because we consider some profiles that have only temperature measurements, as XBT profiles.

Through a visual inspection of the station maps, we noticed that some profiles appeared to be wrong, as their position corresponded to a land point (e.g Figure 2.28). Therefore, we proceeded to an additional quality control on the station coordinates. We added the GEBCO (General Bathymetric Chart of the Oceans) gridded bathymetric data set to the MySQL database, putting

[8] http://www.nodc.noaa.gov/GTSPP/

Key	Entry Term	Abbreviated term	Term definition
0	no quality control	none	No quality control procedures have been applied to the data value. This is the initial status for all data values entering the working archive.
1	good value	good	Good quality data value that is not part of any identified malfunction and has been verified as consistent with real phenomena during the quality control process.
2	probably good value	probably_good	Data value that is probably consistent with real phenomena but this is unconfirmed or data value forming part of a malfunction that is considered too small to affect the overall quality of the data object of which it is a part.
3	probably bad value	probably_bad	Data value recognised as unusual during quality control that forms part of a feature that is probably inconsistent with real phenomena.
4	bad value	bad	An obviously erroneous data value.
5	changed value	changed	Data value adjusted during quality control. Best practice strongly recommends that the value before the change be preserved in the data or its accompanying metadata.
6	value below detection	BD	The level of the measured phenomenon was too small to be quantified by the technique employed to measure it. The accompanying value is the detection limit for the technique or zero if that value is unknown.
7	value in excess	excess	The level of the measured phenomenon was too large to be quantified by the technique employed to measure it. The accompanying value is the measurement limit for the technique.
8	interpolated value	interpolated	This value has been derived by interpolation from other values in the data object.
9	missing value	missing	The data value is missing. Any accompanying value will be a magic number representing absent data.
A	value phenomenon uncertain	ID_uncertain	There is uncertainty in the description of the measured phenomenon associated with the value such as chemical species or biological entity.

FIGURE 2.27: Quality Control flag.

QF	Temperature	QF%	Salinity	QF%	Depth	QF%
0	719180	2.56%	719598	2.57%	1127663	4.02%
1	26653249	95.03%	15989979	57.01%	26714494	95.25%
2	49615	0.18%	0	0.00%	161788	0.58%
3	12596	0.05%	8986	0.03%	2316	0.01%
4	25583	0.10%	39039	0.14%	41481	0.15%
5	9	0.00%	0	0.00%	2	0.00%
9	587513	2.09%	11290143	40.25%	1	0.00%

TABLE 2.8: Temperature, salinity, and depth Quality Flag values.

it in a separate table. GEBCO was used to identify and remove the offending profiles. Figure 2.29 illustrates the land points found and Figure 2.30 the corrected map.

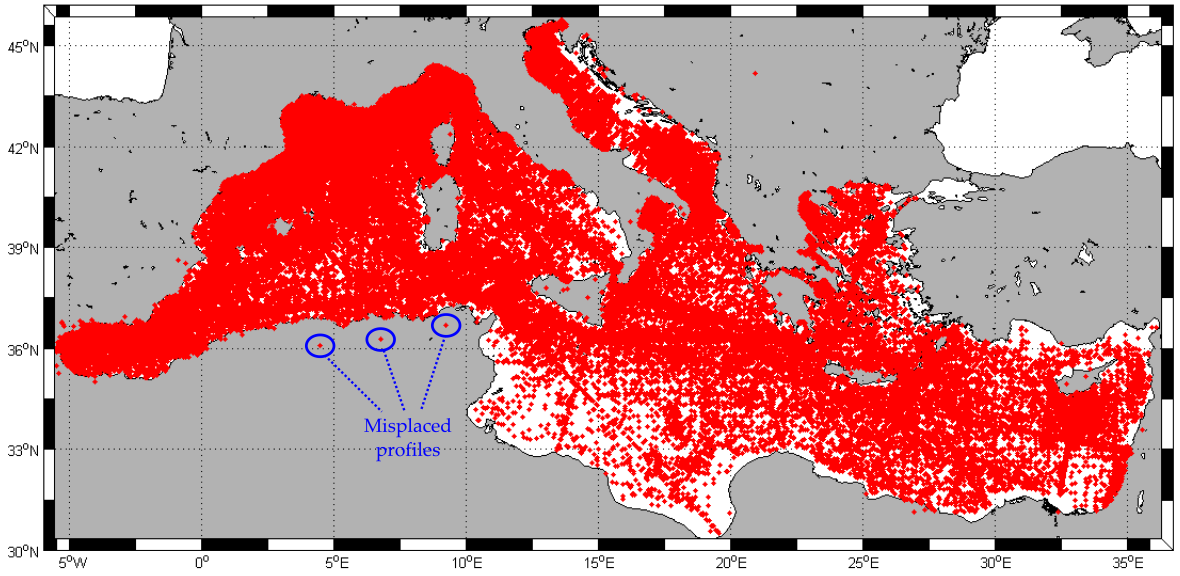

FIGURE 2.28: Example of map with wrong positions.

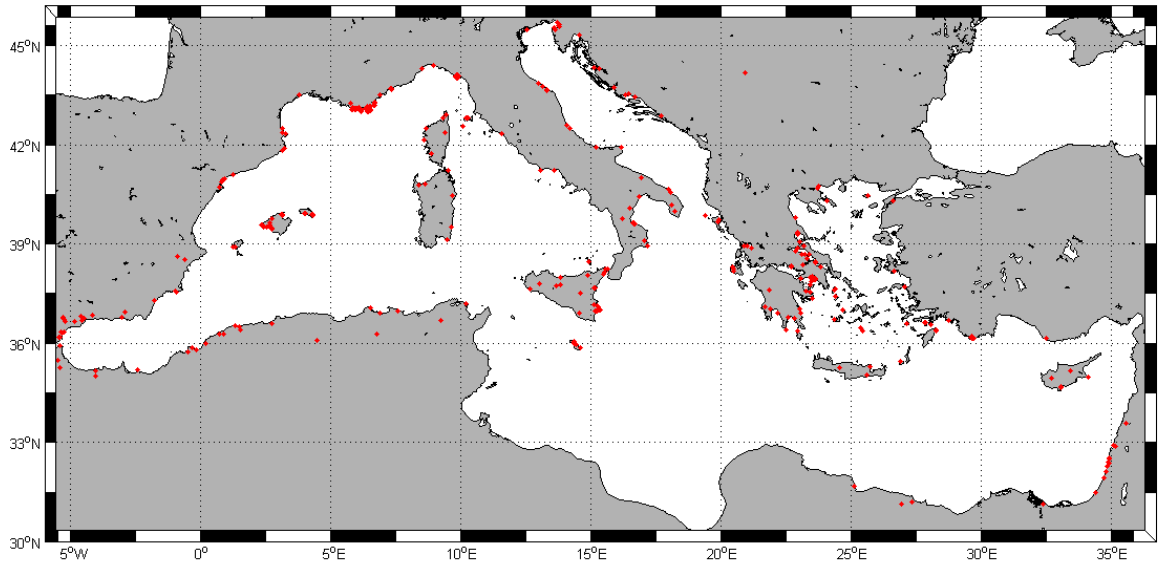

FIGURE 2.29: Map with land points.

The number of profiles with wrong positions is 2763, about 1.67% of the total casts. Most wrong positions are very close to the coast. It is important to exclude these profiles from the analysis in that the coastal data can produce very strong gradients on the climatologies for effect as river

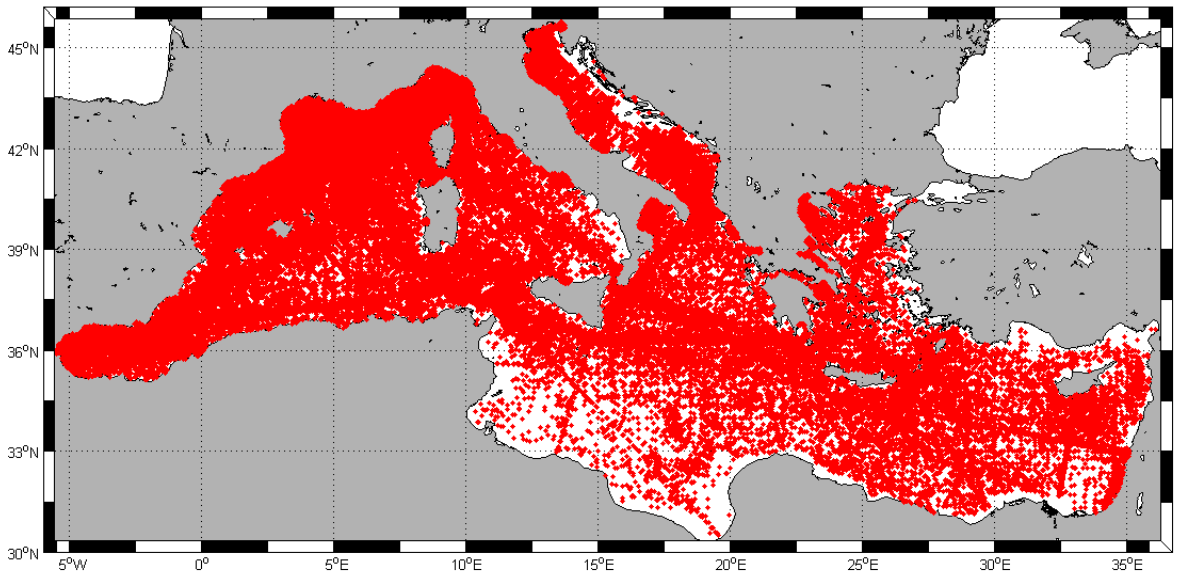

FIGURE 2.30: Correct map.

runoff... In general, for other uses of the data an additional quality control is necessary that considers additional types of procedure to check whether the coastal position is wrong.

GEBCO also allowed us to map the bathymetry of the Mediterranean Sea (Figure 2.31) and to understand the depth distribution of the data in relation to the geographical areas (see Subsection 2.2.3).

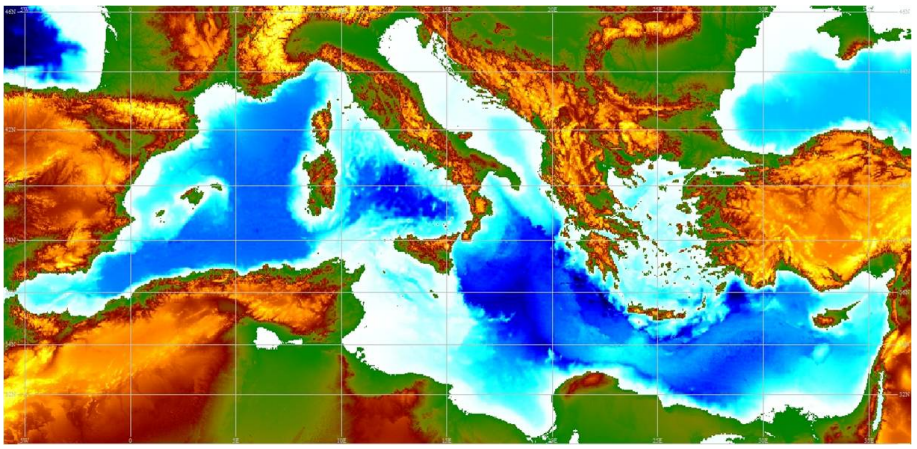

FIGURE 2.31: Bathymetry of the Mediterranean Sea.

This page is intentionally left blank.

Chapter 3

Data analysis algorithms

In Chapter 2 we described the dataset in terms of numbers of profiles and measurements with respect to the time periods, the standard regions, and depth. In this chapter we will focus on the algorithms for the data analysis.

First of all we interpolate vertically each profile to have data on a number of standard levels which will be used in the climatological analysis. Then we describe the Variational Optimal Interpolation theory that allows to spatially interpolate our data and create the climatological fields on a regular grid. For these interpolations we use the data with quality flag 1 for the period 1900 to 2013.

3.1 Vertical interpolation

Data were acquired at discrete irregular levels due to the limitations imposed by the instruments used and the environmental conditions. Therefore, it was necessary to interpolate the profiles on standard levels at a regular distance: in particular we used linear interpolation with a distance of ten metres of depth between levels. We used a linear interpolation that takes a linear polynomial as function.

Let $T(z)$ be the temperature at depth z. In order to calculate a data point on a standard level z we solve the equation:

$$T(z) = T(z_0) + \frac{T(z_1) - T(z_0)}{z_1 - z_0}(z - z_0) \tag{3.1}$$

$z_1 \geq z$ and $z_0 \leq z$ are the depth levels closest to z where the actual value of the temperature is provided by the data set. The same equation applies for the salinity as well.

In order to interpolate the profiles, we employed an ad-hoc Python program (see Appendix).The program is articulated in four steps:

1. Definition of the standard depth levels, from the surface to 5500 m with a step every 10 metres.
2. Identification of the two nearest neighbours (greater and lower) of each level through the function `findNearest`.
3. Definition of the linear equation, as seen above, in general form.
4. Calculation of the differences between the involved depth and the nearest neighbours to check that they are distant at most 5 m from the standard level. If the check succeeds, the interpolated temperature and salinity levels are calculated. Otherwise, no interpolated values are computed, and the program proceeds to the next standard level. It is necessary to deal with the surface layer (0 m) as a special case: this level does not have the lower neighbour and this is why we decided to take the greater neighbour only, provided it lies within a 5 m range.

Figure 3.1 shows an example of an interpolated profile. The blue line is the original profile and the red line is the interpolation. The result is quite satisfactory, as the interpolation curve fits accurately the profile curve.

3.2 Variational Optimal Interpolation Techniques

In this section we present the DIVA software that permits to interpolate data spatially and produce the smoothest field of the parameter at issue. DIVA is the acronym for Data-Interpolating Variational Analysis: the software, developed in Fortran 90, uses the Variational Inverse Method (VIM) to create the spatial optimized interpolation. This software was developed by GHER (GeoHydrodynamics and Environment Research), a research group of the University of Liègi, and thus solving of the classical gridding problem in oceanography. The gridding problem is related to the inhomogeneous distribution of *in situ* data in space and time and the necessity to determine a field on a regular grid. In Figure 3.2 there is a schematic representation of the

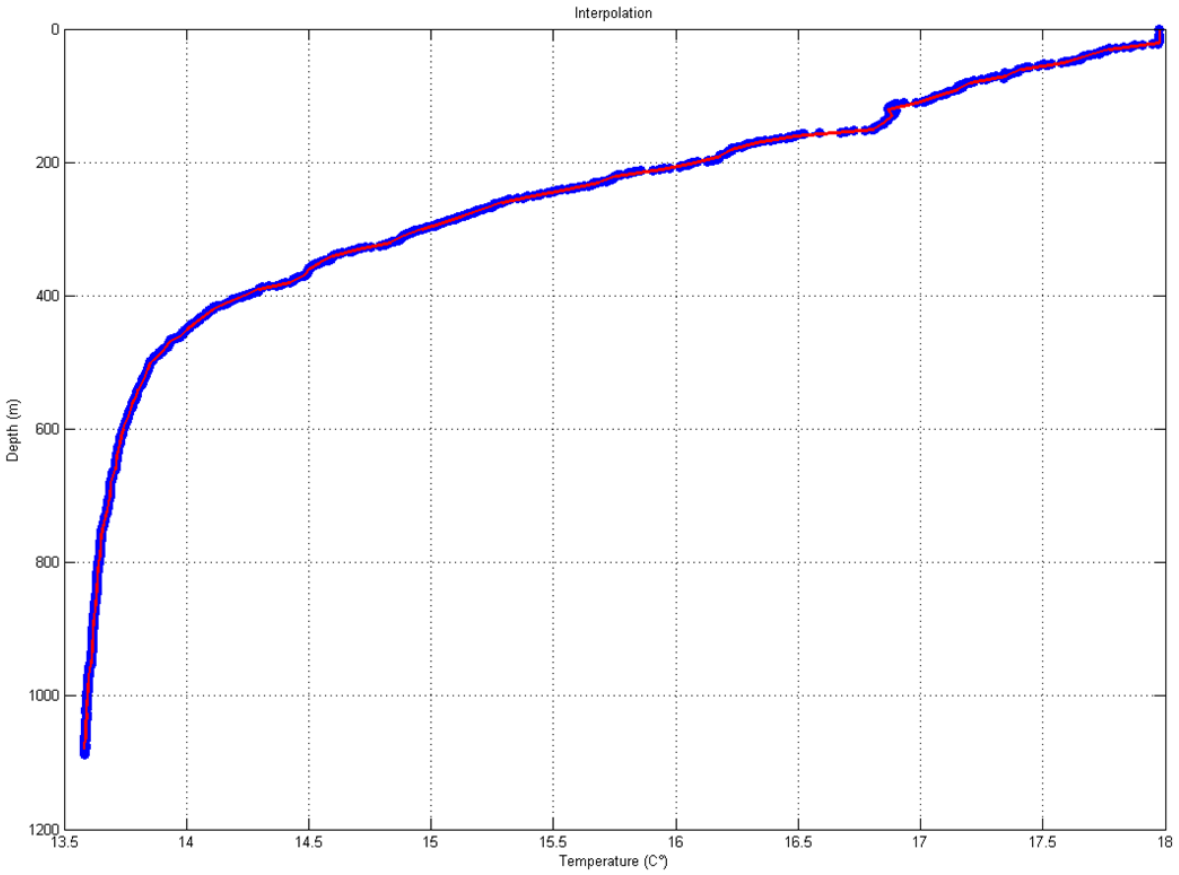

FIGURE 3.1: Example of interpolated profile.

gridding: the blue dots are the data points that are interpolated on the black dot that represents a standard grid point of the target field.

3.2.1 Theory

The oldest method introduced in oceanography and meteorology to construct an optimal interpolation of data is the Objective Analysis (OA) (Gandin, 1965), expressing the target field $\phi(\mathbf{r})$ as a linear combination of the data anomalies d_j with respect to a background field $\phi_b(\mathbf{x})$:

$$\phi(\mathbf{r}) = \phi_b(\mathbf{r}) + \sum_{j=1}^{N_d} d_j w_j \tag{3.2}$$

with w_j are weights, N_d represent the number of data, and x is the location of the data point represented by longitude e latitude. The criterion of the method is to minimize the expect error $e(\mathbf{x})^2$ assuming the following statistical knowledge of the target field and the noise:

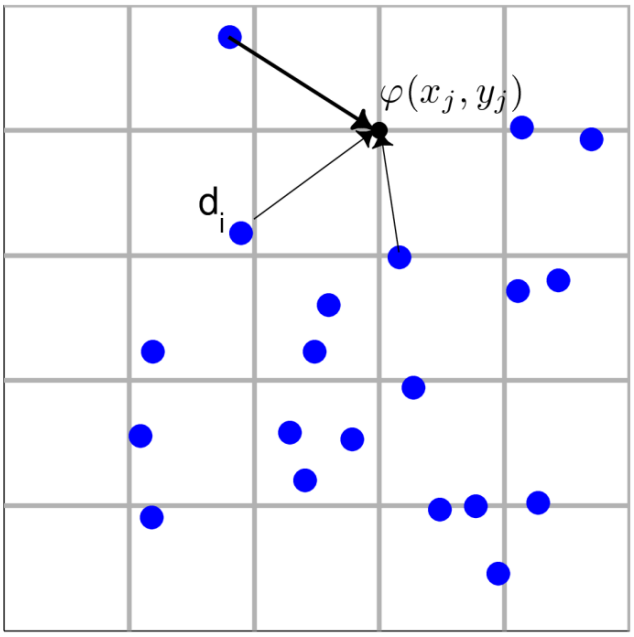

FIGURE 3.2: Gridding problem
Source: http://modb.oce.ulg.ac.be/mediawiki/index.php/File:Gridding2.png

- The mean of the probability distribution of the target field at the point $\mathbf{x}$ is zero.
- The mean of the probability distribution of the noise at the point $\mathbf{x}$ is supposed to be zero.
- The noise is homogeneous.
- The probability distributions are supposed to be uncorrelated from one point to another.

The expect error is:

$$e^2(\mathbf{x}) = \overline{[\phi(\mathbf{x}) - \phi_t(\mathbf{x})]^2} \tag{3.3}$$

with $\phi_t(\mathbf{x})$ is the true(unknown) field, the bar is the average.

Replacing 3.2 in 3.3 and defining the observation covariance matrix $\mathbf{D} = \overline{\mathbf{d}\mathbf{d}^T}$, the covariance between the data and the real field $\mathbf{c} = \overline{\phi_t(\mathbf{x})\mathbf{d}}$, and the vector $\mathbf{w}(\mathbf{x})$, that contain the weights used for interpolation, we obtain:

$$e^2(\mathbf{x}) = \overline{\phi_t(\mathbf{x})^2} \ - \mathbf{c}^T\mathbf{D}^{-1}\mathbf{c} + \left(\mathbf{w} - \mathbf{D}^{-1}\mathbf{c}\right)^T \mathbf{D}\left(\mathbf{w} - \mathbf{D}^{-1}\mathbf{c}\right). \tag{3.4}$$

Assuming that the observations are independent and the observation error covariance is written σ^2, the matrix $\mathbf{D}$ becomes:

$$\mathbf{D} = c(\mathbf{x}_i, \mathbf{x}_j) + \sigma^2\delta_{ij}. \tag{3.5}$$

The solution of the OA is:

$$min\ e^2(\mathbf{x}) = \overline{\phi_t(\mathbf{x})^2}\ - \mathbf{c}^T\mathbf{D}^{-1}\mathbf{c} \tag{3.6}$$

and the result field:

$$\phi(\mathbf{x}) = \phi_b(\mathbf{x}) + \sum_{j=1}^{N_d} d_j w_j = \mathbf{c}^T\mathbf{D}^{-1}\mathbf{d} \tag{3.7}$$

The derivation of the expected error variance $e^2(\mathbf{x})$ from the solution is:

$$e^2(\mathbf{x}) = \epsilon^2(\mathbf{x}) - \mathbf{c}\mathbf{x}^T\mathbf{D}^{-1}\mathbf{c}\mathbf{x} \tag{3.8}$$

where ϵ^2 is the prior error variance. It is possible to notice that the data distribution and the statistics control the error estimation. This result field is the best estimation possible but it is important insert the correct specification of the covariances.

The variational analysis (VIM), used by DIVA and introduced in meteorology by Wahba and Wendelberger [14], was proved to be statically equivalent to the OA (Brasseur *et al.*, 1996) but uses as method of resolution the minimization of a variational principle on the domain of interest Ω performed with a finite-element method. This type of method is a spline analysis. The variational principle on the domain of interest Ω to be minimized is:

$$min_\phi\ J[\phi],\ J[\phi] \equiv \sum_{j=1}^{N_d} \mu_j \left[d_j - \phi(\mathbf{x_j})\right]^2 + \|\phi\|^2 \tag{3.9}$$

and the norm is defined:

$$\|\phi\|^2 = \int_\Omega \left(\alpha_2 \nabla\nabla\phi : \nabla\nabla\phi + \alpha_1 \nabla\phi \cdot \nabla\phi + \alpha_0 \phi^2\right)\, d\Omega \tag{3.10}$$

with:

- α_0 is the weight on the field ϕ.
- α_1 is the weight on the gradient of the field and so on the slope of ϕ.
- α_2 is the weight on the variability and the curvature of the field.
- μ is the weight on data. It is assigned to each data and it is defined as:

$$\mu = \frac{\sigma^2}{\epsilon^2}\frac{4\pi}{L^2} \tag{3.11}$$

where the first fraction is the signal-to-noise ratio, σ^2 is the data error variance, ϵ^2 is the background error variance and L is the correlation length. The latter represents the distance over which a given data point influences its neighbourhood, and estimate the shape of the correlation function.

If we suppose that the domain Ω is infinite the solution to the variational problem 3.9 can be written as:

$$\phi = \mathbf{c}^T(\mathbf{x})\mathbf{D}^{-1}\mathbf{d} \tag{3.12}$$

where $\mathbf{c}(\mathbf{x})$ is the data-field covariance, $\mathbf{d}$ the data vector, and $\mathbf{D}$ is the data correlation matrix defined as:

$$\mathbf{D} = K(\mathbf{x}_i, \mathbf{x}_j) + \frac{1}{\mu}\delta_{ij} \tag{3.13}$$

where K is the kernel of the Hilbert space and in an infinite domain is proportional to the correlation function. The kernel function used in this case is given by:

$$K(r) = \left(\frac{r}{L}\right) K_1 \left(\frac{r}{L}\right) \tag{3.14}$$

with r is the Euclidean distance, L the correlation function, and K_1 is the modified Bessel function. The equation 3.12 has the same structure solution of the OA minimization and it is the proof of the statistical equivalence of the two methods. Table 3.1 summarizes the two type of analysis.

	OA	**VIM**
Minimization	$e^2(\mathbf{x}) = \overline{[\phi(\mathbf{x}) - \phi_t(\mathbf{x})]^2}$	$J[\phi] \equiv \sum_{j=1}^{N_d} \mu_j \left[d_j - \phi(\mathbf{x_j})\right]^2 + \|\phi\|^2$
Solution	$\phi(\mathbf{x}) = \mathbf{c}^T\mathbf{D}^{-1}\mathbf{d}$	$\phi(\mathbf{x}) = \mathbf{c}^T\mathbf{D}^{-1}\mathbf{d}$
Data correlation	$[\mathbf{D}]_{ij} = c(\mathbf{x}_i, \mathbf{d}_j) + \sigma^2\delta_{ij}$	$[\mathbf{D}]_{ij} = K(\mathbf{x}_i, \mathbf{x}_j) + \frac{1}{\mu}\delta_{ij}$
Data-field covariance	$[\mathbf{c}]_i = c(\mathbf{x}_i, \mathbf{x}_j)$	$[\mathbf{c}]_i = K(\mathbf{x}, \mathbf{x}_i)$

TABLE 3.1: Statistical equivalence between the OA and VIM.
Source: Rixen *et al.*, 2000

The solution 3.12 for the variational problem has a high numerical cost for a big number of data. Furthermore, differently from the atmospheric domain which is unbounded, the ocean domain which is bounded by the coasts, makes it difficult to find a rigorous analytical solution to VIM and a finite element method is implemented to solve these problems.

3.2.2 Finite-Element solution method

As in Diva User Guide [15], the minimization of 3.9 is performed by a Finite Element (FE) method, hence the need for generating a finiteelement grid. Because the field to analyse is only defined in the water, the minimization also works only within the contours defining the coastline or more generally, the considered isobath. Thus the grid generation has to be consistent with the coast existing in the considered region. The corresponding mathematical problem is referred to the *Constrained Triangulation*. To solve 3.9, the real domain is split into a mesh of N_e triangularelement (e.g. Figure 3.3):

$$J(\phi) = \sum_{e=1}^{N_e} J_e(\phi_e). \tag{3.15}$$

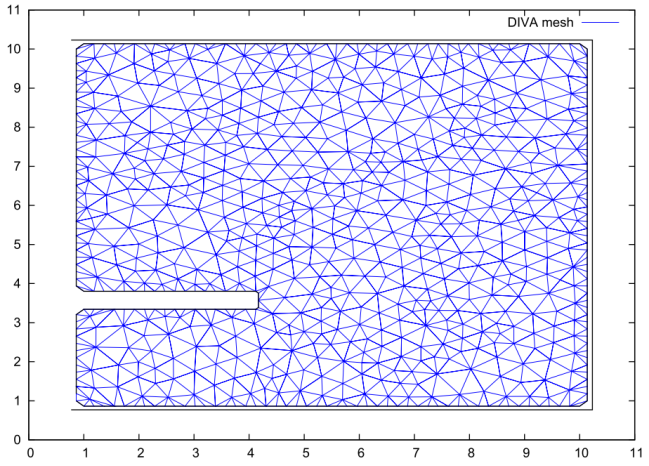

FIGURE 3.3: Diva example mesh.
Source: Introduction to Optimal Interpolation and Variational Analysis, Barth *et al.*, 2008

In each element the solution is a linear combination of a set of shape functions $\mathbf{s}$ (3^{rd} polynomials) and the continuity between elements is assured by identification of adjacent *connectors*:

$$\phi_e(\mathbf{r}_e) = \mathbf{q}_e^T \mathbf{s}(\mathbf{r}_e) \tag{3.16}$$

with $\mathbf{q}$ the connectors vector and $\mathbf{r}_e$ the position in a local coordinate system. Substituting 3.16 in 3.15 and using the variational principle 3.9, we get

$$J_e(\mathbf{q}_e) = \mathbf{q}_e^T \mathbf{K}_e \mathbf{q}_e - 2\mathbf{q}_e^T \mathbf{g}_e + \sum_{j=1}^{N_{de}} \mu_j d_j^2 \tag{3.17}$$

where K_e the local stiffness matrix and g is a vector which depends on local data. Matrix K is decomposed into a normrelated term and a data related term. On the whole domain, 3.17 reads:

$$J(\mathbf{q}) = \mathbf{q}^T\mathbf{K}\mathbf{q} - 2\mathbf{q}^T\mathbf{g} + \sum_{j=1}^{N_d} \mu_j d_j^2 \tag{3.18}$$

of which the minimum is reached where:

$$\mathbf{q} = \mathbf{K}^{-1}\mathbf{g}. \tag{3.19}$$

Matrix K has a size approximatively proportional to the number of degrees of freedom of the system, but can be very sparse if the elements are properly sorted.

To map the data on the finite element mesh, a transfer operation T_2 (depending on the shape functions) is applied:

$$\mathbf{g} = \mathbf{T}_2(\mathbf{x})\mathbf{d}. \tag{3.20}$$

and to have the solution at any location inside the domain, another transfer T_1 is applied:

$$\phi(\mathbf{x}) = \mathbf{T}_1(\mathbf{x})\mathbf{q}. \tag{3.21}$$

Combining the two previous equations, we obtain the relation between ϕ, the interpolated field at location $\mathbf{x}$ and the data vector $\mathbf{d}$:

$$\phi = \mathbf{T}_1(\mathbf{x})\mathbf{K}^{-1}\mathbf{T}_2(\mathbf{x})\mathbf{d}. \tag{3.22}$$

In analogy with the OA solution, the error estimation of the variational method is:

$$e^2(\mathbf{x}) = \epsilon^2(\mathbf{x}) - \mathbf{T}_1(\mathbf{x})\mathbf{K}^{-1}\mathbf{T}_2(\mathbf{x})\mathbf{c}(\mathbf{x}). \tag{3.23}$$

We will show some examples of error maps in Section 4.1.3.

Chapter 4

Data analysis results

In this Chapter we focus the attention on the description of the gridded fields produced by DIVA. We show some examples of the background fields used to perform the analysis, and of temperature and salinity maps at some levels, and in some months, and seasons. Furthermore we present the analysis error maps, and try to estimate the 'goodness'[1] of our gridded fields , intercomparing gridded fields from previous analyses.

4.1 Mapped fields

The analysis is computed with the DIVA version: DIVA3D (Diva-4.6.4). The climatologies are produced for 33 standard levels (5500, 5000, 4500, 4000, 3500, 3000, 2500, 2000, 1750, 1500, 1400, 1300, 1200, 1100, 1000, 900, 800, 700, 600, 500, 400, 300, 250, 200, 150, 125, 100, 75, 50, 30, 20, 10, 0 m) and the horizontal grid is $1/8° \times 1/8°$, starting from $(9.25°W, 30°N)$ and ending $(36.5°E, 46°N)$.

To run the analysis, it is important to set the free parameters of the algorithm and decide about the input dataset. The coastline files are important because they permit to set the domain of the variational analysis. The coastlines were computed by Tonani *et al.* [16].

The free parameters of the Variational Techniques to be set are:

- The Correlation Length, that we set constant and equal to 2°.

[1]The goodness is interpreted as the Murphy definition (see Section 4.2).

- The grid coordinates in degree (longitude & latitude).
- The assumption on the background error variance ϵ^2 equal to 0.6 for temperature and salinity.
- The Signal to Noise ratio, that is set constant and equal to 0.5

4.1.1 Background field

As said in the previous section, the background field is the first guess of the mapping algorithm.

The background fields were computed at Istituto Nazionale di Geofisica e Vulcanologia (INGV) and given to us for conducting the present analysis. They were computed with monthly mean for temperature, and annual mean for salinity in each level.

In Figure 4.1 we present the background fields for temperature and salinity. Figure 4.1a and 4.1b show, respectively, the temperature and salinity backgrounds at the surface, Figure 4.1c and 4.1d at 100 m, and Figure 4.1e and Figure 4.1f at 500m.

The white zones are the areas with a shallower bathymetry than the level considered. The Black Sea and the Bay of Biscay are excluded from the analysis. These backgrounds have been heavily smoothed and averaged.

4.1.2 Temperature and salinity maps

In this Subsection we present and comment on some temperature and salinity climatologies calculated with DIVA. These gridded fields describe and represent the main characteristics of the Mediterranean water masses and some aspects of the Mediterranean circulation. To make a more detailed analysis on the superposition of the 3 different water masses of the Mediterranean, we show three main different depths for both temperature and salinity fields.

Let us consider Figure 4.2 that shows the temperature distributions on the surface in March, June, September and December. We show these months to represent the seasonal cycle of the thermal field. As one can notice there are a remarkable differences between the Western and Eastern basin. To start with, the Western basin presents smaller values than the Eastern basin. This is related to the modification of the Atlantic Water that changes its characteristics during the circulation into the entire basin. Another important feature consist in the different

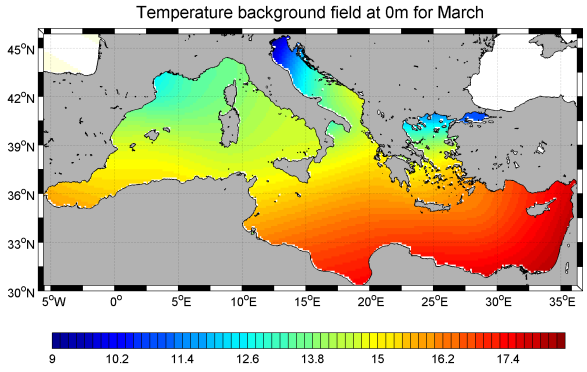

(a) Temperature backgound at 0m

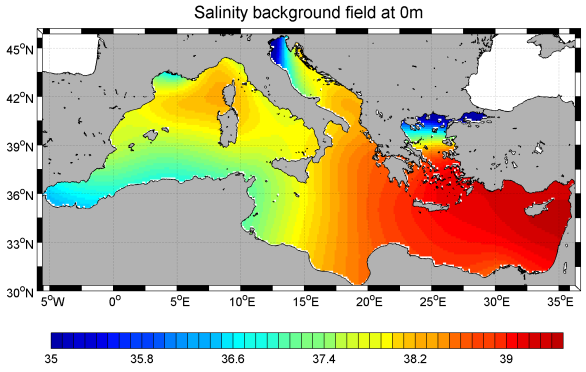

(b) Salinity backgound at 0m

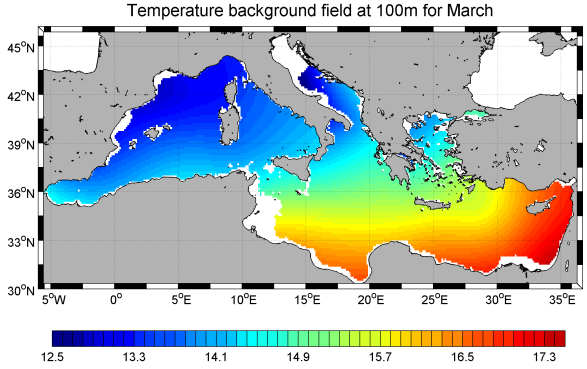

(c) Temperature backgound at 100m

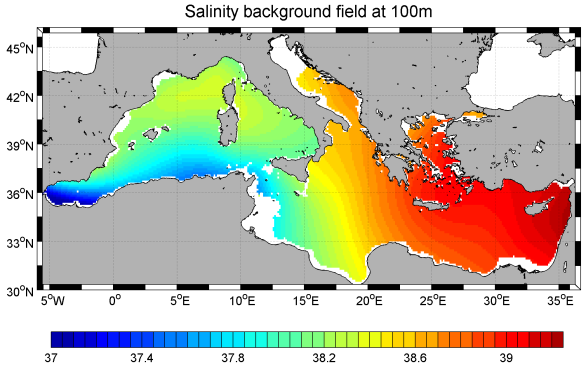

(d) Salinity backgound at 100m

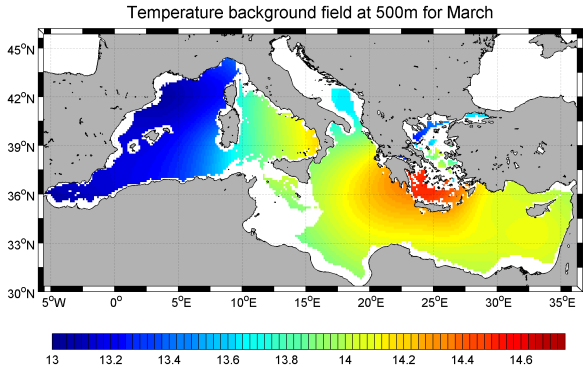

(e) Temperature backgound at 500m

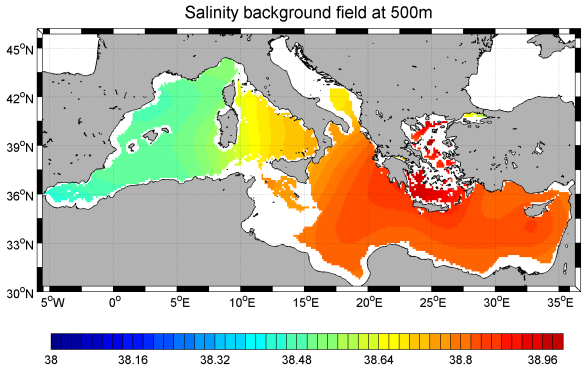

(f) Salinity backgound at 500m

FIGURE 4.1: Examples of monthly temperature and annual salinity background fields at different depths for March.

values occurring during the various months. We can see a mean shift of about $7°C$ between March to June in both regions. The zone with the lowest temperature values is the Adriatic Sea. Furthermore, it is possible to notice some subbasinscale gyres and eddies whose energetic features vary with to the season. An example is the Rhodes Gyre occurring between summer and autumn in the East of Crete, which is quite visible in Figure 4.2c and Figure 4.2d, and is identified by the minimum of temperature.

Figure 4.3 illustrates the salinity distributions of the surface by seasons. We can see homogeneous increase of salinity from the Strait of Gibraltar, where it is about 36.6 psu, to the Eastern basin, where the values exceed 39 psu, in particular in the Levantine basin. These high values are strictly connected to the air surface interaction, the strong evaporation that exceeds precipitation, and the river runoff. In fact the zones with the lowest salinity values are placed on river estuaries, as the North Adriatic, or are close to other basins, as the North Aegean Sea, connected to the Black Sea. Furthermore, we notice that in the Western basin the highest values of salinity occur during winter and spring; whereas the Eastern basin has the higher values in summer and autumn, except for the Adriatic Sea that presents the highest values in winter. This situation is connected to atmospheric events and some oceanic processes such as, for example, the deep water formation in the Gulf of Lions during winter. In this area we can see a strong cyclonic gyre that disappears in summer.

Let us now consider the temperature fields at 100m, shown in Figure 4.4. We can notice some remarkable characteristics at this depth. First of all the highest temperature values are occurr in autumn and rather than in summer, with the a mean shift of only $1°C$ with respect to winter. The Western basin shows lower temperatures than the Eastern one, in particular in the Gulf of Lions. The Adriatic Sea is, as usual, the zone with the lowest temperatures in the Eastern part. In general the subbasinscale features, for istance the Rhodes Gyre and the eddies in the Algerian basin, are less represented. The main feature that we can notice is the Ierapetra Gyre that occurs in summer and autumn at the southeast of Crete.

The salinity fields at 100m, shown in Figure 4.5, present a more homogeneous trend than at the surface. In the Western basin we can find a salinity range from about 37 to about 38.5 psu, with a maximum of 38.6 psu during spring in the eastern coast of the Corsica island. In the Eastern basin the range is between 38.4psu and 39 psu, with a maximum of about 39.5 psu in the Levantine basin and the southern Aegean Sea during spring. The lowest values of salinity in the Eastern part are near the coasts of Libya and Tunisia. Near the Israel coast we can notice

a weak gyre of about 39.25 psu, named the Shikmona Gyre that has its major intesity during winter.

Figure 4.6 shows the temperature field at 500m. We can see the decrease of temperature range in the entire basin and the homogeneity of the distribution, in particular in the Western basin. The temperature values of the northwestern and western part of the Western basin are between $13°C$ and $13.45°C$; whereas the values of the eastern part, separated by Corsica and Sardinia, are between $13.7°C$ and $14.2°C$. This is connected to the westward circulation of the LIW from the Eastern Basin. The lowest temperatures occur in the Gulf of Lions in winter and autumn, associated with the Deep Water formation. In the Eastern basin the temperature range is between $13.8°C$ and $14.6°C$. The highest temperature is found in the Sea of Crete (southern part of the Aegean Sea), where there is the Cretan Deep Water formation, during winter and autumn. In the south of the Crete island, we can see the Ierapetra Gyre in three different energetic conditions: it is stronger in winter than in summer and autumn. Furthermore, we can notice the seasonal cycle of the Western Cretan Cyclonic Gyre, with the highest intensity in autumn. Finally, near the coast of Israel, Lebanon and Syria, there is the Shikmona Gyre that shows its lowest intensity in summer and its highest intensity during winter.

Figure 4.6 shows the temperature field at 500m. We can see the decrease of temperature range in the entire basin and the homogeneity of the distribution, in particular in the Western basin. The temperature values of the northwestern and western part of the Western basin are between $13°C$ and $13.45°C$; whereas the values of the eastern part, separated by Corsica and Sardinia, are between $13.7°C$ and $14.2°C$. This is connected to the westward circulation of the LIW from the Eastern Basin. The lowest temperatures occur in the Gulf of Lions in winter and autumn, associated with the Deep Water formation. In the Eastern basin the temperature range is between $13.8°C$ and $14.6°C$. The highest temperature is found in the Sea of Crete (southern part of the Aegean Sea), where there is the Cretan Deep Water formation, during winter and autumn. In the south of the Crete island, we can see the Ierapetra Gyre in three different energetic conditions: it is stronger in winter than in summer and autumn. Furthermore, we can notice the seasonal cycle of the Western Cretan Cyclonic Gyre, with the highest intensity in autumn. Finally, near the coast of Israel, Lebanon and Syria, there is the Shikmona Gyre that shows its lowest intensity in summer and its highest intensity during winter.

Figure 4.7 shows the salinity field at 500m. We can see a slight increase of the salinity values in the Western basin: the range is between about 38.48 psu and about 38.70 psu. This is connected

to the progressive mixing of the LIW, that proceed towards the Strait of Gibraltar. The range of salinity values of the Eastern basin is between about 38.64 to 38.8 psu. The highest salinity values are about 38.96 psu and are found in the Sea of Crete. As with temperature, we can notice some subbasin gyres, as the Ierapetra and the Shikmona, with a weaker intensity.

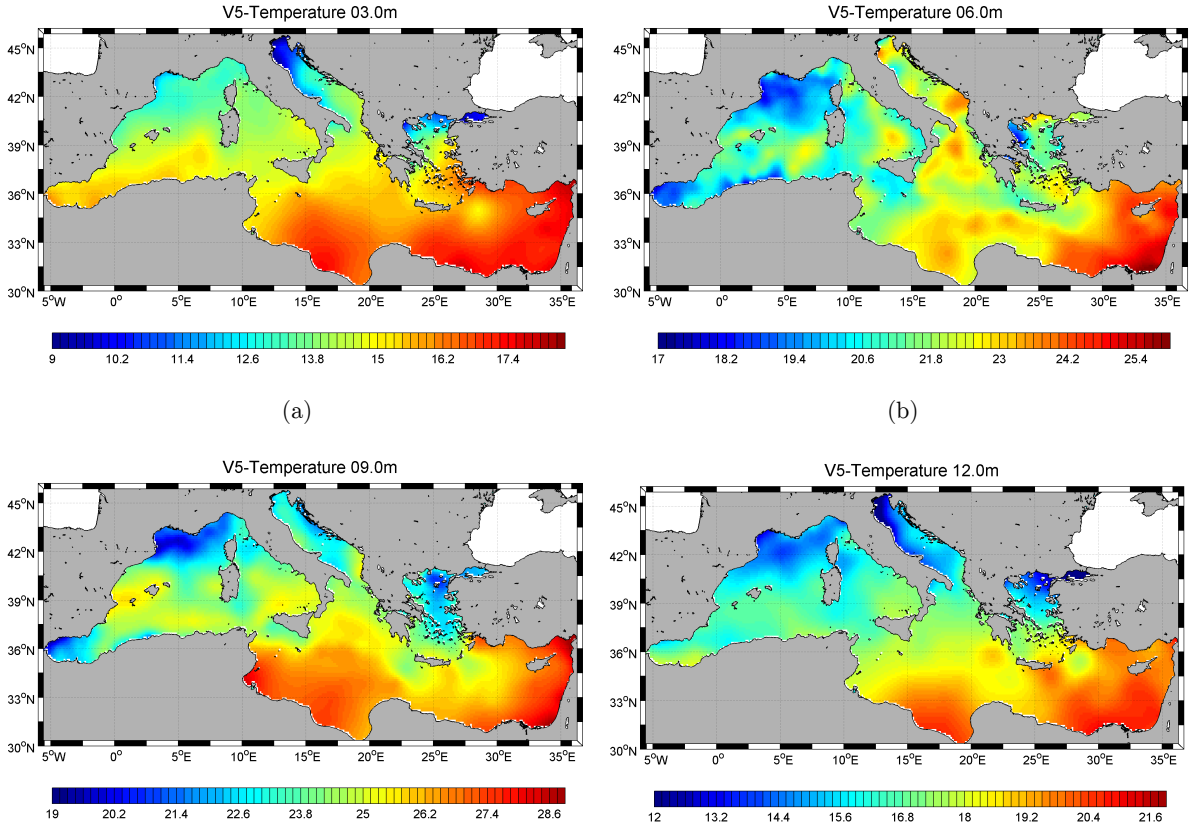

(a) (b)

(c) (d)

FIGURE 4.2: Temperature climatologies of the surface for March, June, September, and December.

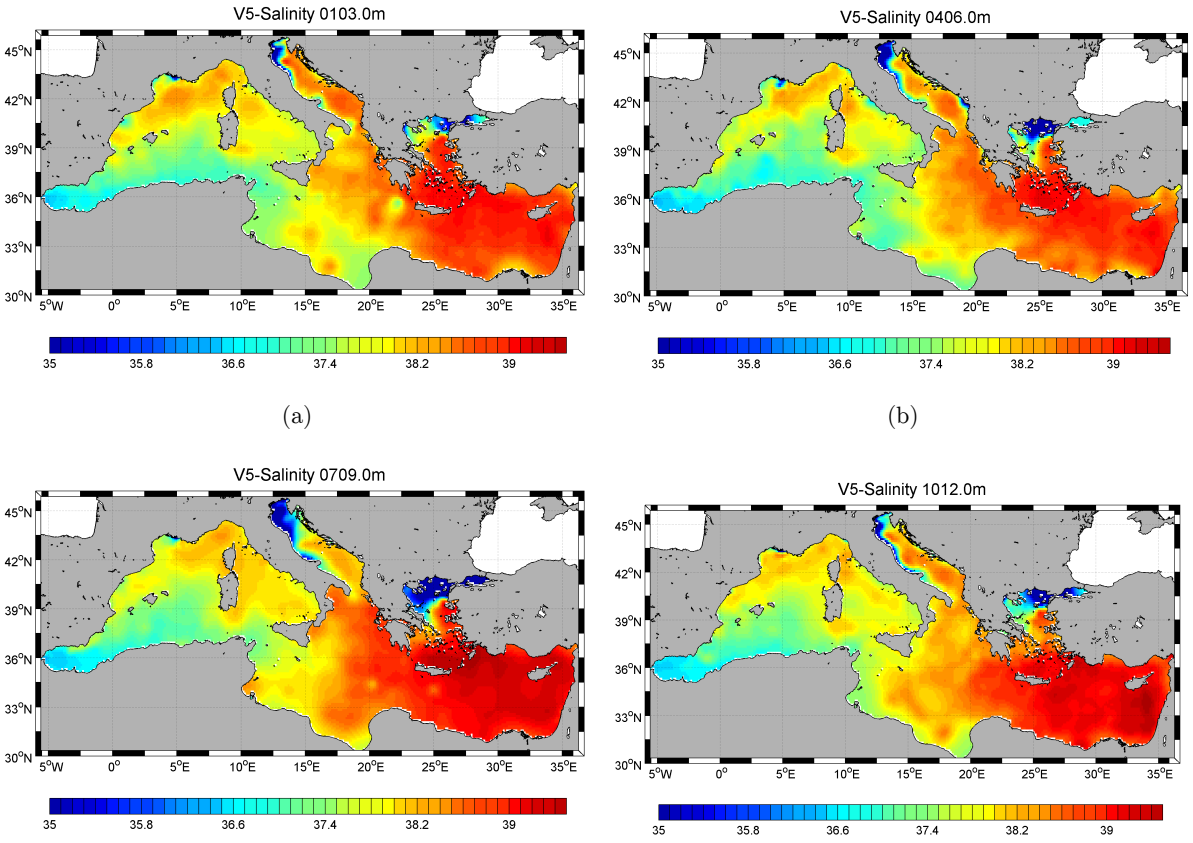

FIGURE 4.3: Salinity climatologies of the surface divided by seasons.

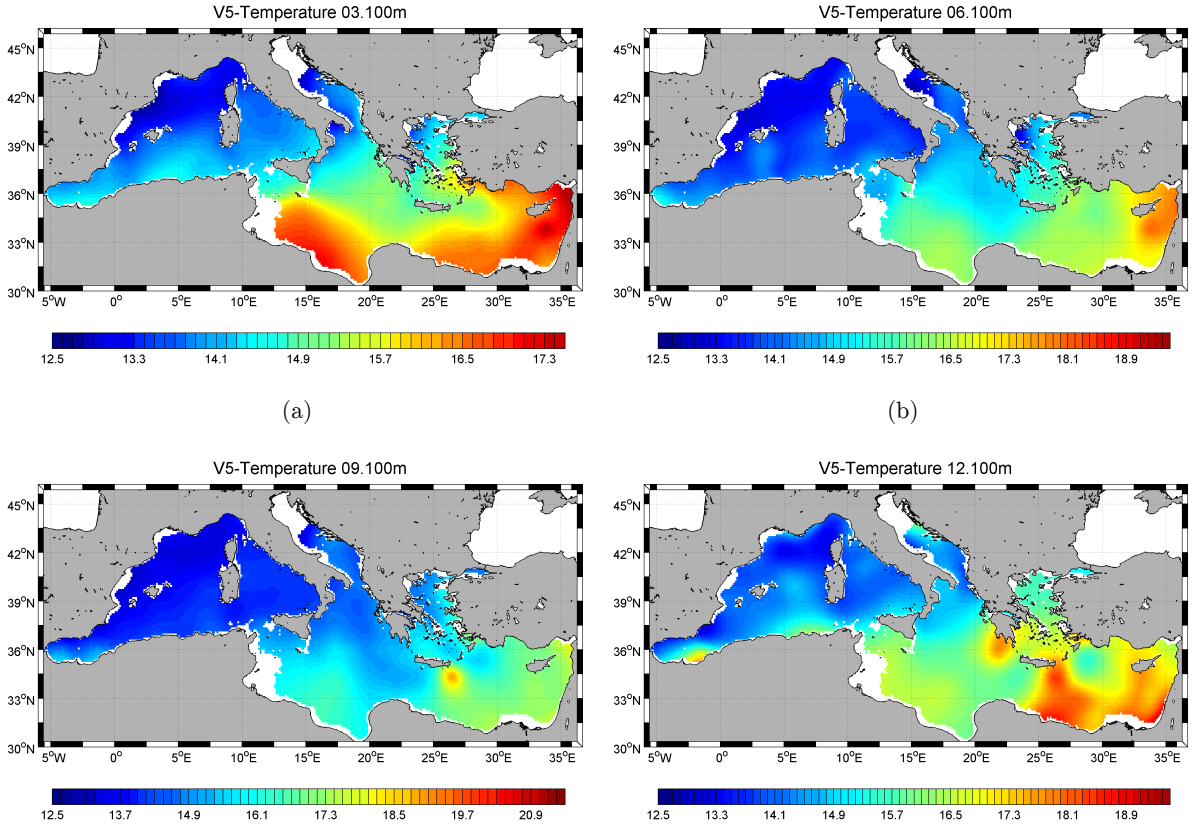

(a) (b)

(c) (d)

FIGURE 4.4: Temperature climatologies at 100m for March, June, September, and December.

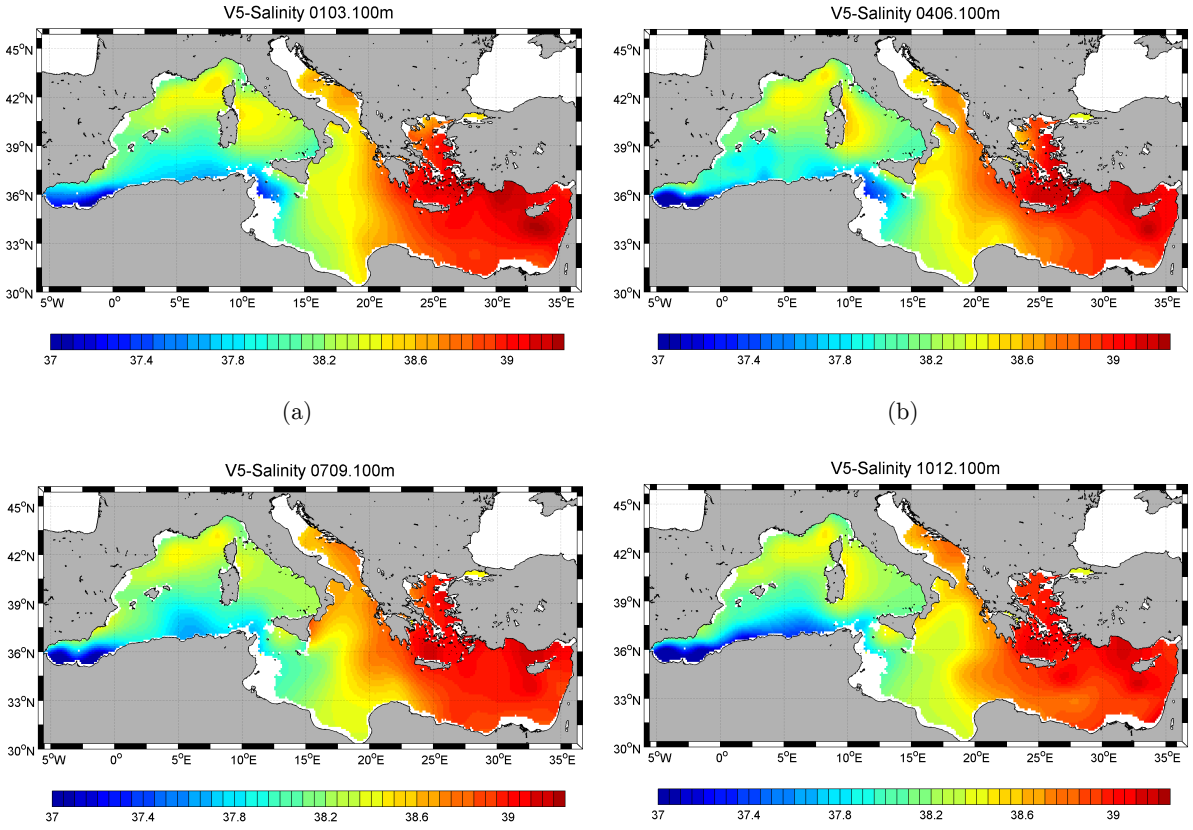

FIGURE 4.5: Salinity climatologies at 100 m divided by seasons.

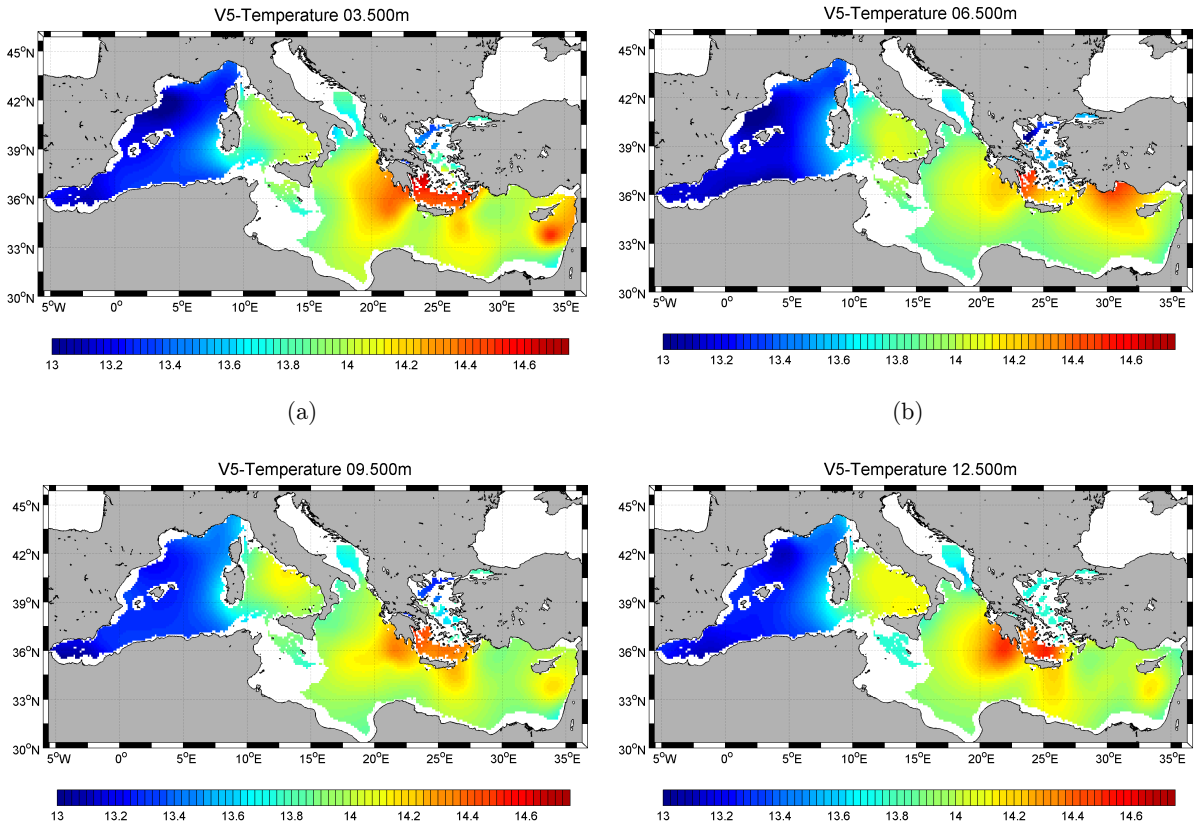

FIGURE 4.6: Temperature climatologies at 500m for March, June, September, and December.

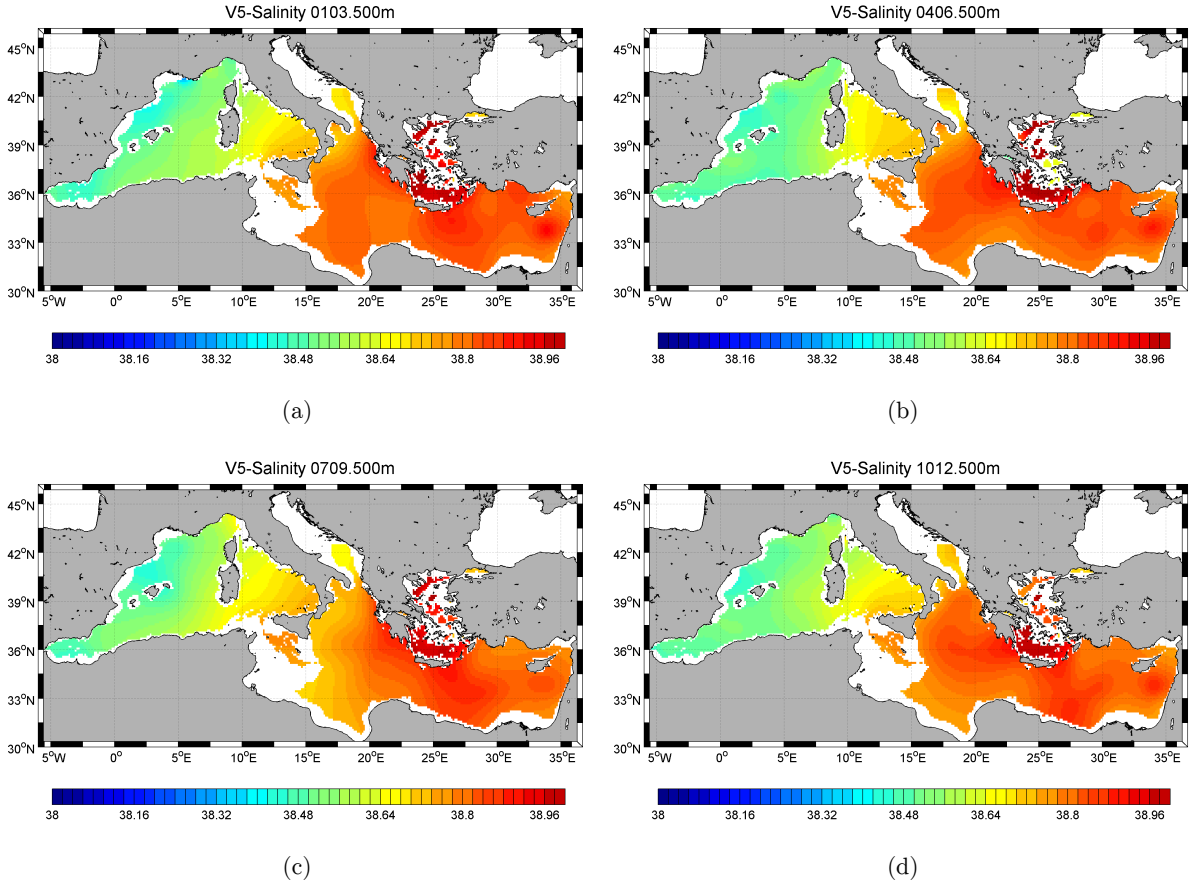

FIGURE 4.7: Salinity climatologies at 500 m divided by seasons.

The climatologies presented in this Section seem to be close to the real structure of the Mediterranean Sea. To demonstrate their goodness, in Section 4.2 we focus on the comparison between the present version and a previous version of the climatological fields, developed by INGV-CMCC for SeaDataNet 2.

4.1.3 Temperature and salinity error maps

In this Subsection we present some examples of error maps and focus on the connection between variational error values and data distribution.

As seen in Section 3.2.1, in particular equation 3.23, the error of the variational method is influenced by the data coverage and the data noise: in those regions which are void of data the variational error variance tends towards the background error variance ($e \sim \epsilon$). In regions with a high number of data the variational error decreases according to the data error variance. In

our analysis, we compute the variational error with the expression 3.23 with the background error variance ϵ^2 constant and equal to 0.6 and on the specified gridded domain.

In Figure 4.8 we can see some temperature error maps that are the proof of what we said, above. Figure 4.8a shows the temperature error map for September at the surface: here the error value is lower than 0.2. In fact we can see that the horizontal distribution is homogeneous enough.

By contrast Figure 4.8b represents the temperature error map for September at 500m: here we can see that the error value in some zones is superior to 0.4. It is possible to notice that these areas are void of data.

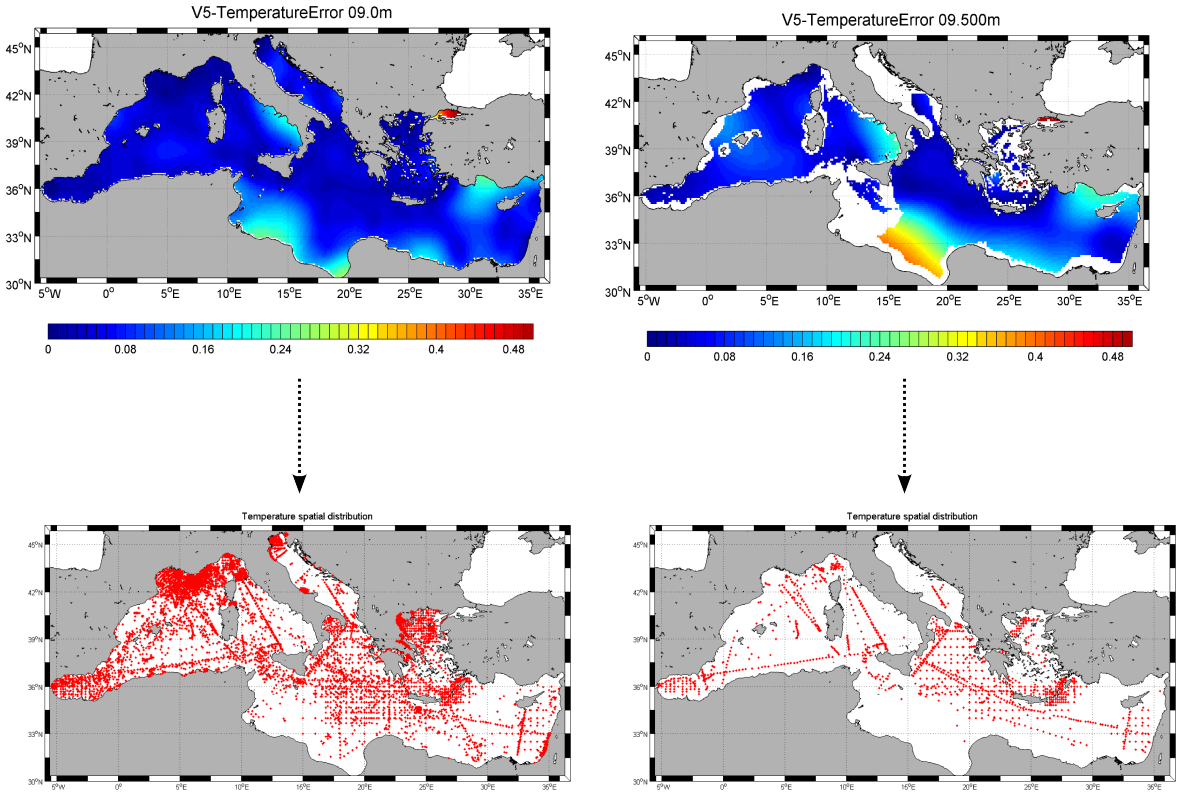

(a) (b)

FIGURE 4.8: Temperature error maps with the corresponding data distribution maps.

In Figure 4.9 we can see some salinity error maps. Figure 4.9a the salinity error map for summer at the surface: here the error values are high especially in the coastal zones. These areas are void of data. Figure 4.9b show the salinity error map for summer at 500m.

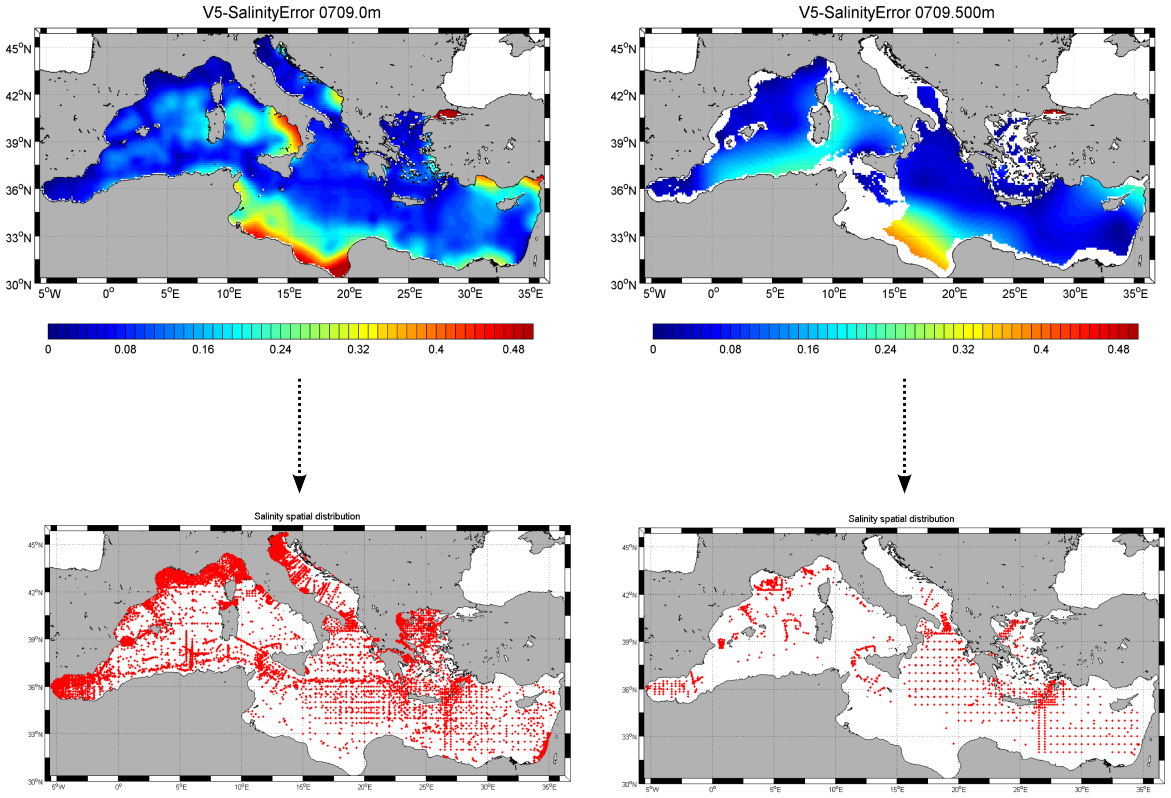

(a) (b)

FIGURE 4.9: Salinity error maps with the corresponding data distribution maps.

Considering as background error variance a value of $0.6°C$, we can calculate a surface temperature error of about $0.12°C$, taking from the temperature map error a value of 0.2 and an error of about $0.3°C$ at 500m, considering a value of 0.5% at 500m. For salinity we can calculate the error in the same way.

4.2 Quality Assessment criteria for the climatologies

In this Section we try to establish how our climatologies are 'good', following the types of goodness identified by Murphy (1993) to evaluate weather forecasts. [17]

There are different opinions in the scientific community about the phrases "that was a good forecast" or "that was a bad forecast". To solve these misunderstandings and the lack of clarity about the nature of goodness of weather forecasts, Murphy introduced three different types of practical relationship that indicate the goodness of a forecast:

- Type 1 goodness or *Consistency* is the correspondence between forecasts and forecaster's judgments.
- Type 2 goodness or *Quality* is the correspondence between forecasts and observations.
- Type 3 goodness or *Value* evaluates the usefulness of the forecasts for the users.

In this Section we will focus on the fist two types of goodness. To contextualize these general indications to our case, we name V5 our climatology, and V3 a previous version of the climatologies. The V3 version of the temperature and salinity fields was created using the data, provided by the MEDATLAS, MATER[2], and MFS[3] datasets for the period 1900-1999. For the period from 2000 to 2008 it was used the data provided by the SeaDataNet dataset. V3 and V5 present the same standard levels, coastlines files and dimensions of the output grid.

4.2.1 Consistency

In this Section we try to understand if our climatological fields are good in the type 1 sense, finding a correspondence between the V5 and the V3 fields through a visual inspection and our knowledge of the Mediterranean temperature and salinity characteristics. First of all we will describe the maps, pointing out differences and similarities.

Let us start by comparing the V5 with the V3 temperature fields at surface for March, June, September, and December, as shown in Figure 4.10. We can notice that the fields are quite similar. The only difference is that in the V5 the subbasin gyres and eddies are more marked, as in Figure 4.10c where the Sirte Gyre, the Northern Ionian Cyclonic Gyre, and the Southern Adriatic gyres are more pronounced. We can see some eddies near the Algerian coasts. Moreover some slight differences can be noticed along the Lebanon coasts.

Let us now consider the comparison between the V5 and the V3 salinity fields at surface divided by seasons, as shown in Figure 4.11. The V5 climatologies result to be slight accurate for gyres and eddies in particular in the centre of the Mediterranean Sea, it happened with the temperature fields. An example is the Western Cretan Cyclonic Gyre in Figure 4.11a.

Figure 4.12 and Figure 4.13 illustrate, respectively, the temperature and salinity fields of the V5 and V3 version at 100m. Temperature climatologies are very similar in both versions except

[2]XBT excluded
[3]Data from 1999-2008, ARGO, XBT and CTD

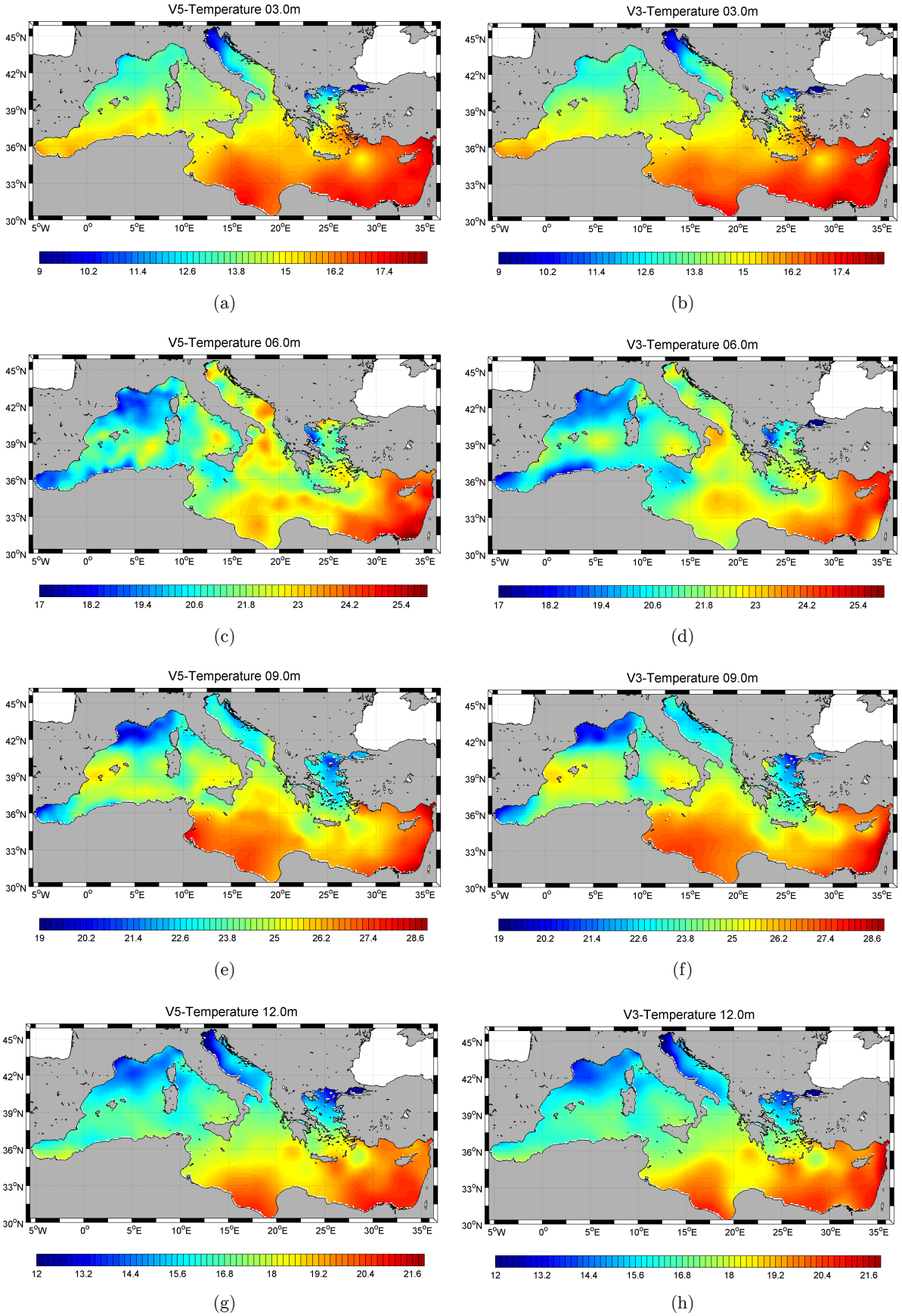

FIGURE 4.10: Comparison of temperature climatologies V5 and V3 at the surface for (a)March, (b)June, (c)September and (d)December.

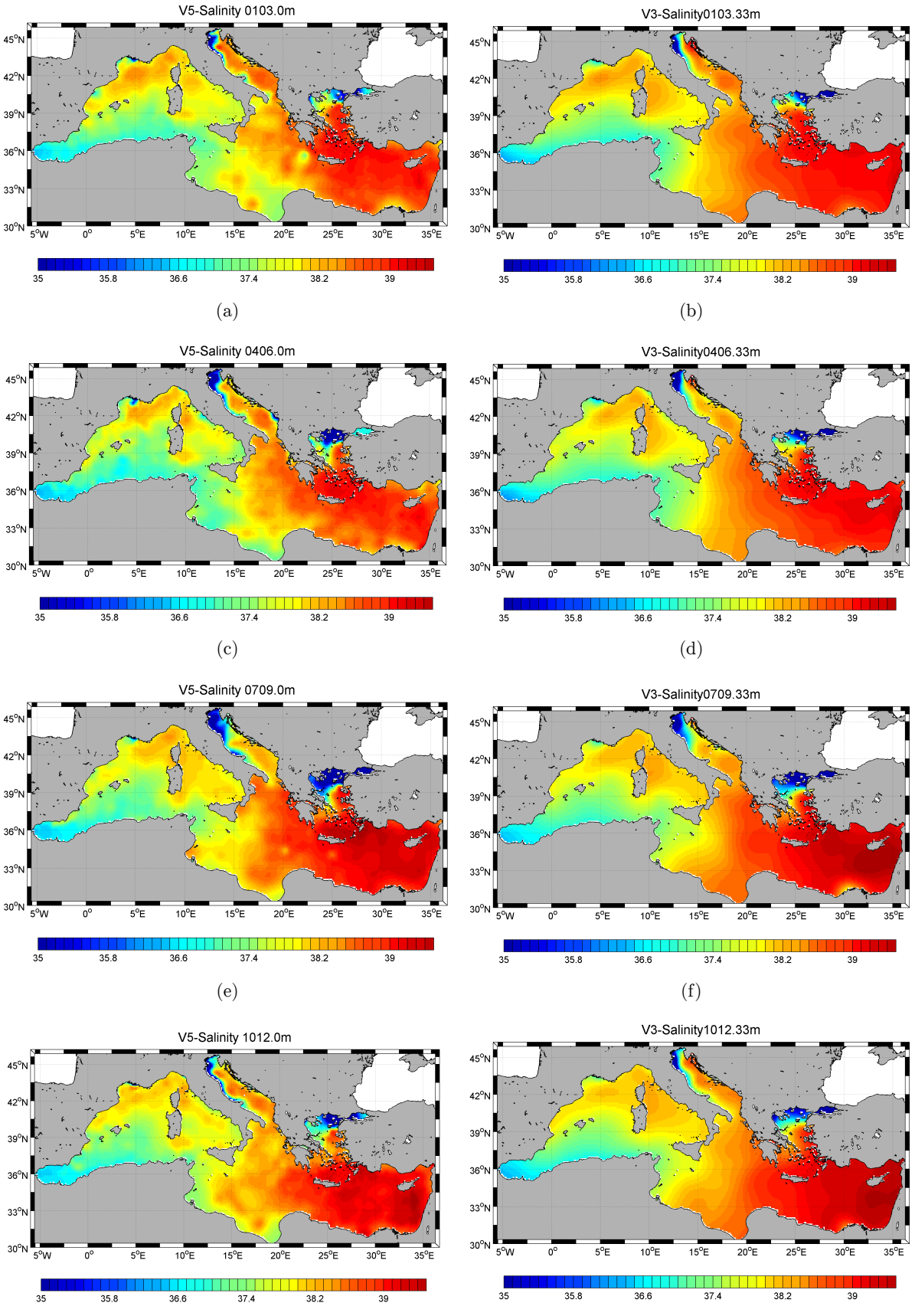

FIGURE 4.11: Comparison of salinity climatologies V5 and V3 at the surface divided by seasons ((a)Winter, (b)Spring, (c)Summer, (d)Autumn).

for the zone near the Lebanon coasts, where V3 presents higher values than V5, in particular for June and September (see Figure 4.12d and Figure 4.12f). Furthermore the Ierapetra Gyre is more marked in the V5 temperature fields in September (see Figure 4.12e). The salinity fields, divided by season, seem to be very similar in both versions except for those zones showing some differences in the temperature climatologies.

Let us consider Figure 4.14 and Figure 4.15 that present the comparison between V5 and V3 temperature and salinity fields at 500m. At this depth, the temperature climatologies present the greatest number of differences, in particular in the Eastern basin. All the V3 maps show more gyres and eddies for all the months in the Ionian basin and near the Greek coasts. In contrast the Western basin presents the same distribution for all cases.

The salinity fields, differently, present the same characteristics in the V5 and the V3 versions in the entire basin for all the seasons.

In short, the two climatological versions seem to be very similar, except for the temperature fields at 500m and some slight differences in the representation of gyres and eddies. The latter result is related to the high variability that these features have in nature. Therefore we can assert that our climatologies seem to be good in the type 1 sense. In the next Section we evaluate the goodness of type 2.

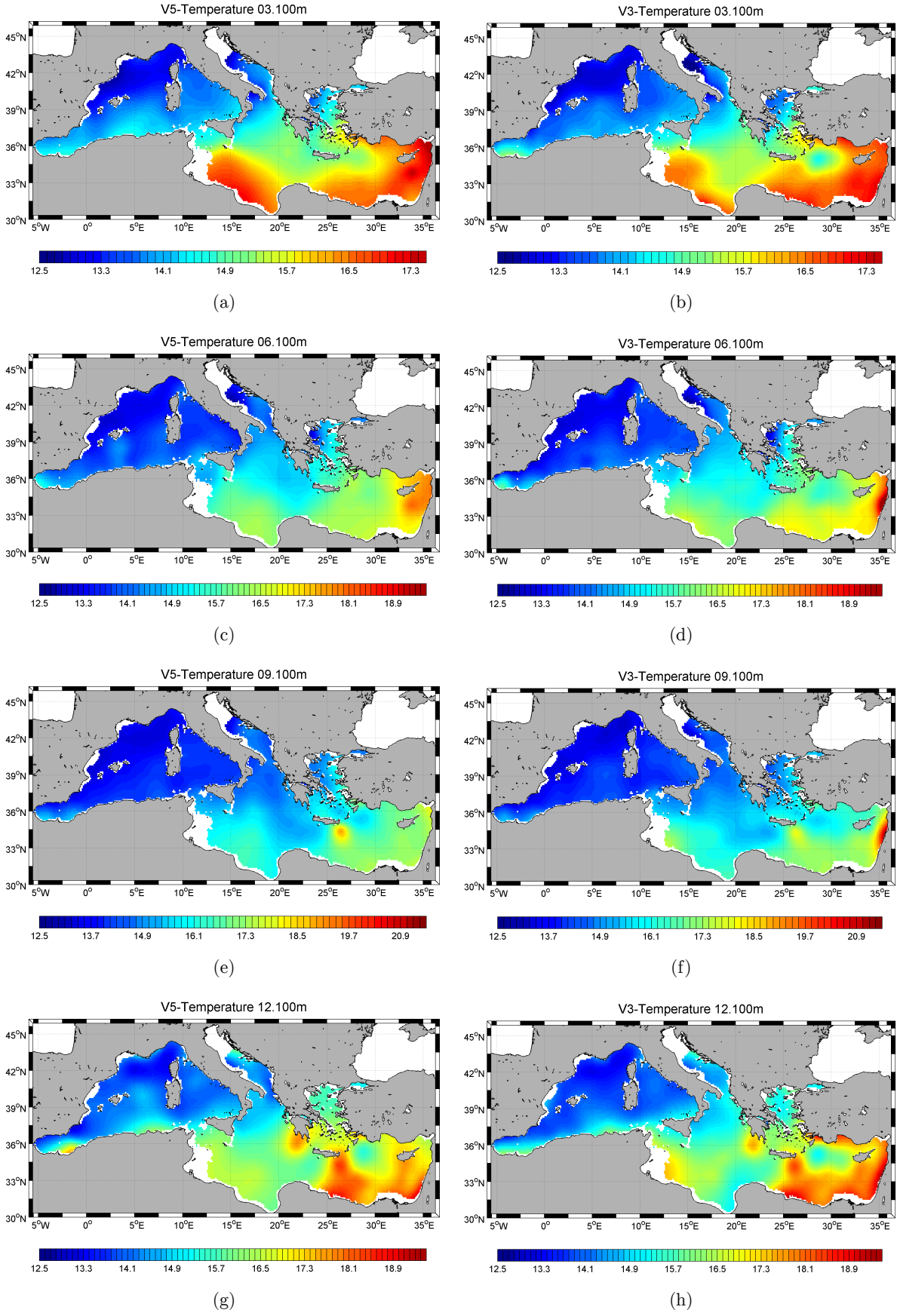

FIGURE 4.12: Comparison of temperature climatologies V5 and V3 at 100 m for (a)March, (b)June, (c)September and (d)December.

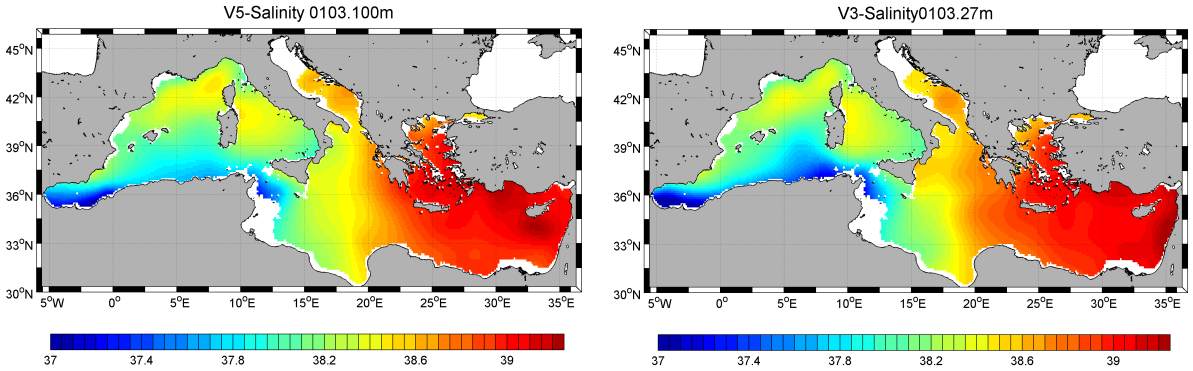

(a) (b)

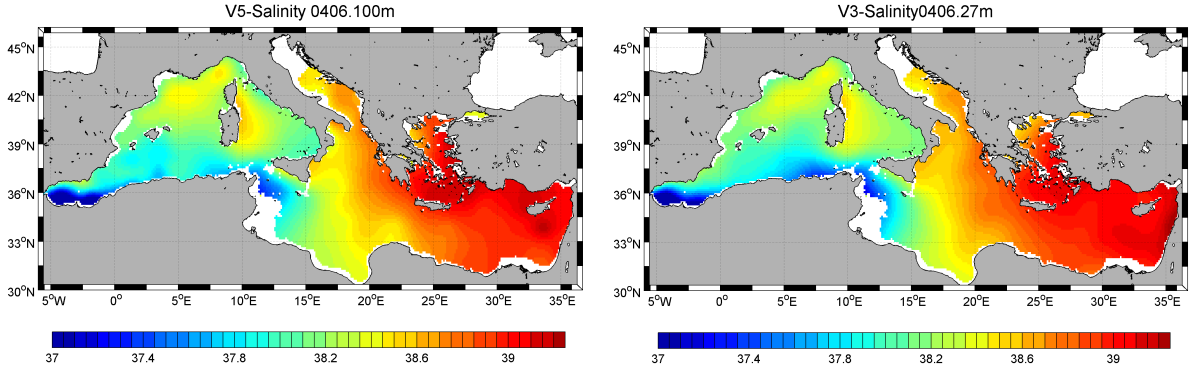

(c) (d)

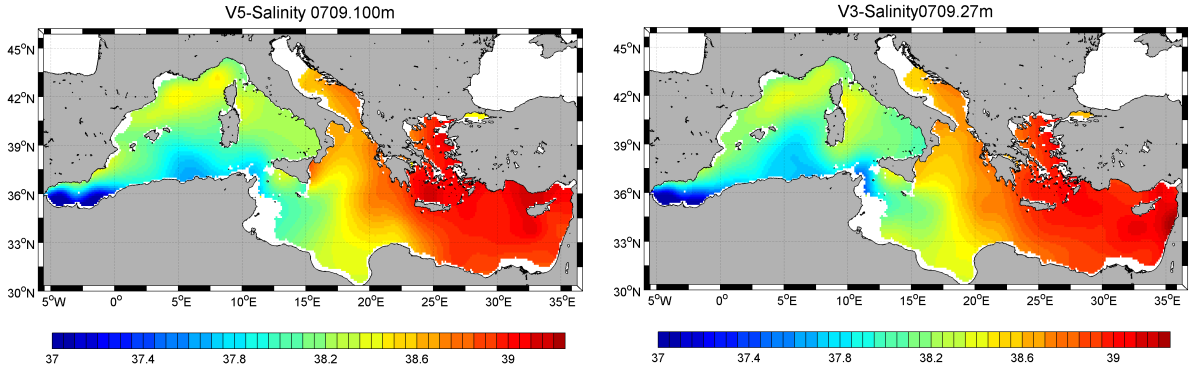

(e) (f)

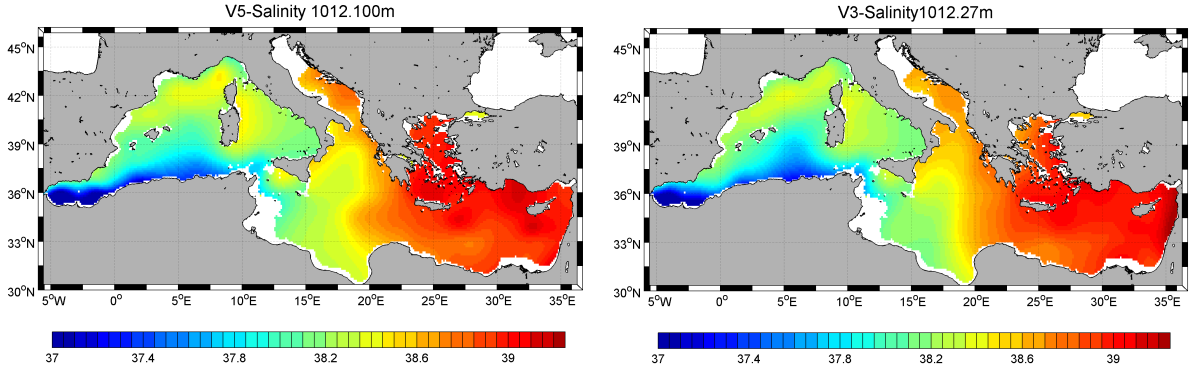

(g) (h)

FIGURE 4.13: Comparison of salinity climatologies V5 and V3 at 100 m divided by seasons((a)Winter, (b)Spring, (c)Summer, (d)Autumn).

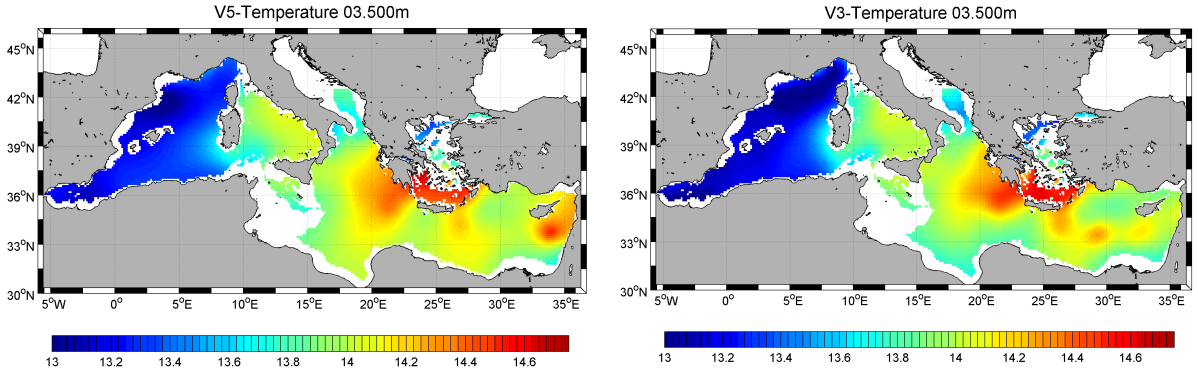

(a)

(b)

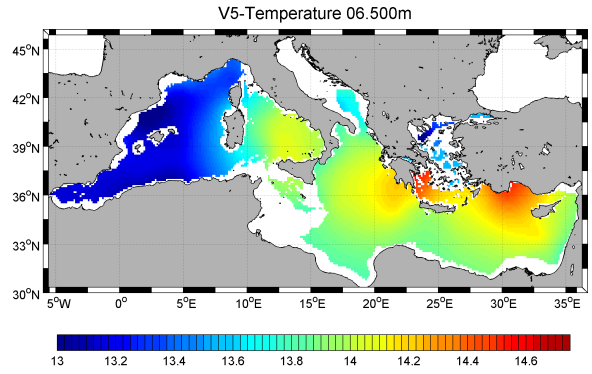

(c)

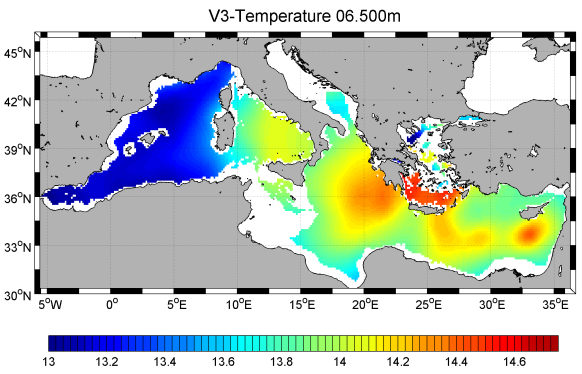

(d)

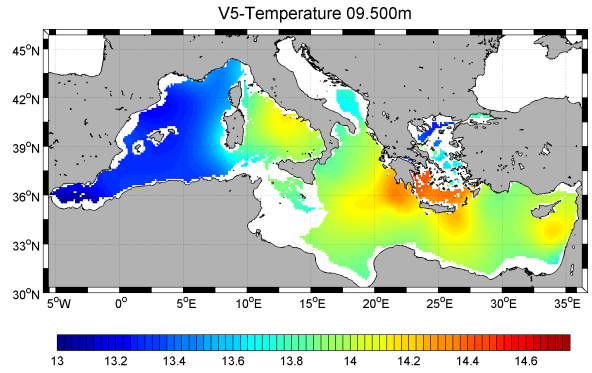

(e)

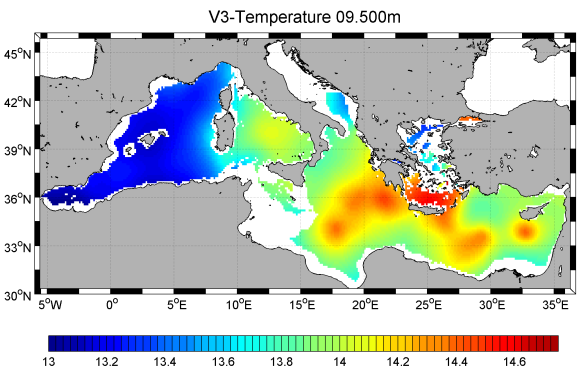

(f)

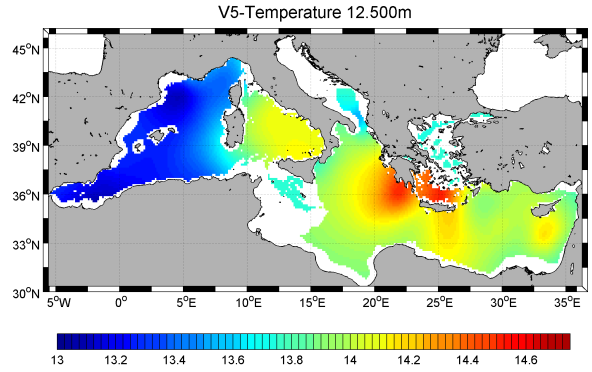

(g)

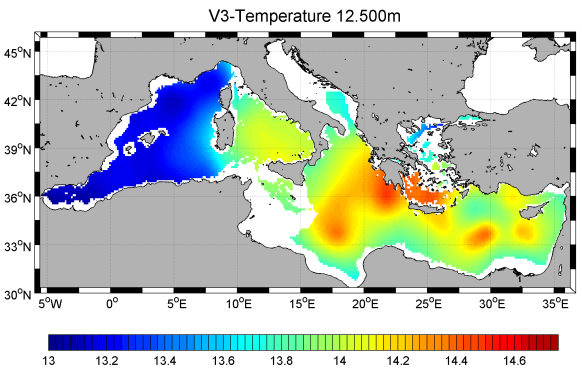

(h)

FIGURE 4.14: Comparison of temperature climatologies V5 and V3 at 500 m for (a)March, (b)June, (c)September and (d)December.

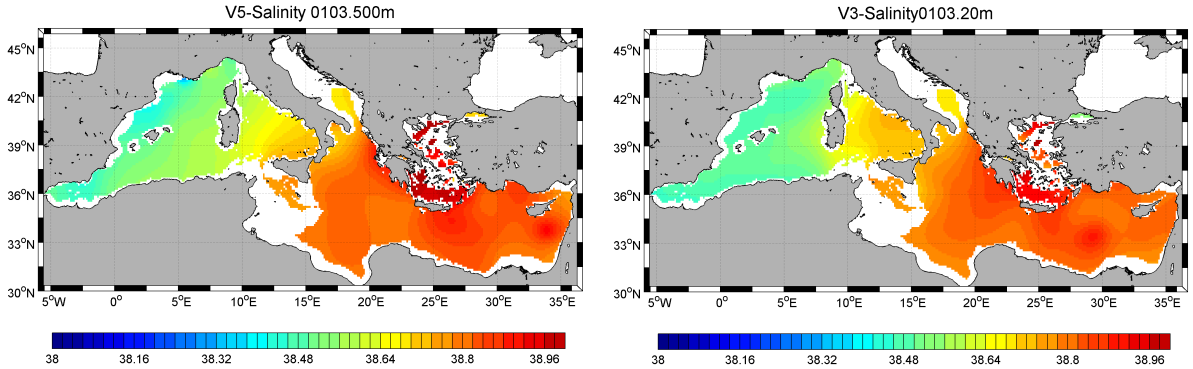

(a) (b)

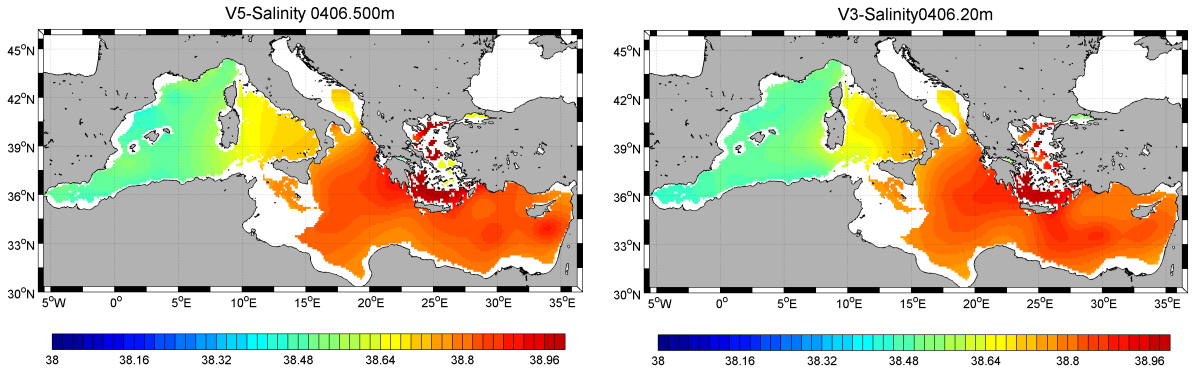

(c) (d)

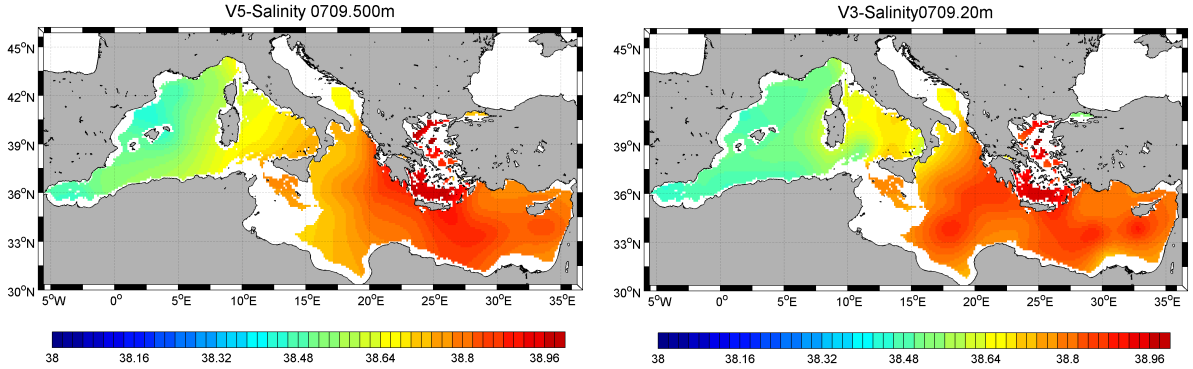

(e) (f)

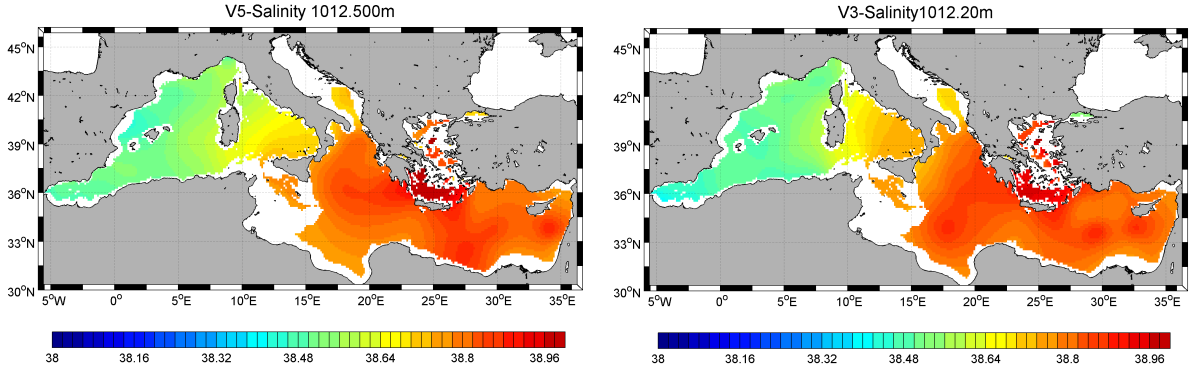

(g) (h)

FIGURE 4.15: Comparison of salinity climatologies V5 and V3 at 500 m divided by seasons ((a)Winter, (b)Spring, (c)Summer, (d)Autumn).

4.2.2 Quality

In this section we address to the following question: "what is the correspondence between the V5 and the V3 fields?". To resolve this issue, we will introduce some statical indexes and we will relate them to compute the degree of correspondence. Furthermore the answer of this question allows us to understand if the V5 fields are good in type 2 sense.

Fist of all, we introduce the element $\theta_{i,j} = [T_{i,j}, S_{i,j}]$ that represents the vectors of the temperature and salinity values where $i = 1...(m \times n)$ is the spatial index, with m the number of grid points in the longitude direction and n in the latitude direction, and $j = 1, ...M$ is the time index.

Second, we calculate the temperature and salinity Standard Deviation (SD) of both versions to point out the natural variability of the fields at different depths. The standard deviation of the V5 is defined as:

$$\mathrm{SD} = \sqrt{\frac{\sum_{i=1}^{N}(\theta'_{i,j,V5})^2}{N}} \tag{4.1}$$

with $\theta'_{i,j,V5} = \theta_{i,j,V5} - \overline{\theta_{V5}}$.

The standard deviation of the V3 is defined as:

$$\mathrm{SD} = \sqrt{\frac{\sum_{i=1}^{N}(\theta'_{i,j,V3})^2}{N}} \tag{4.2}$$

with $\theta'_{i,j,V3} = \theta_{i,j,V3} - \overline{\theta_{V3}}$.

The $\overline{\theta}$ is defined for both case as the temporal and spatial mean:

$$\overline{\theta} = \frac{1}{N}\sum_{i=1}^{N}\frac{1}{M}\sum_{j=1}^{M}\theta_{i,j}. \tag{4.3}$$

Figure 4.16 and Figure 4.17 show the temperature and salinity Standard Deviation profiles of V5 for each depth and month. The major variability is concentrated at the shallower depths in both cases, as we expected.

Figure 4.18 and Figure 4.19 show the temperature and salinity Standard Deviation profiles of V3 for each season and depth. As said above, the greater values of the Standard Deviation are located between 0 and 50 m.

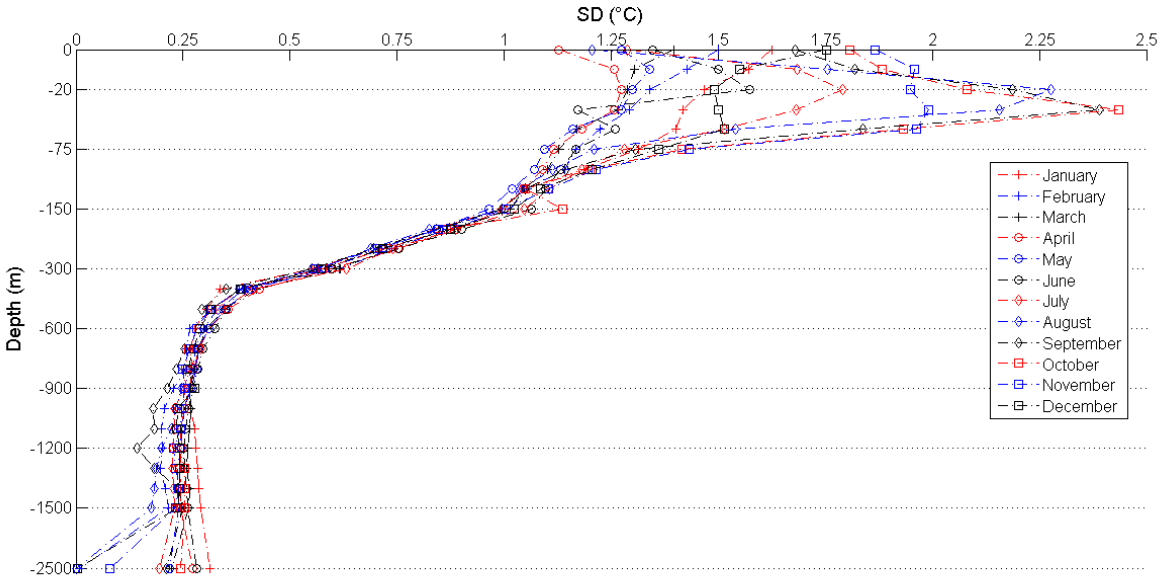

FIGURE 4.16: V5 temperature monthly profiles of Standard Deviation.

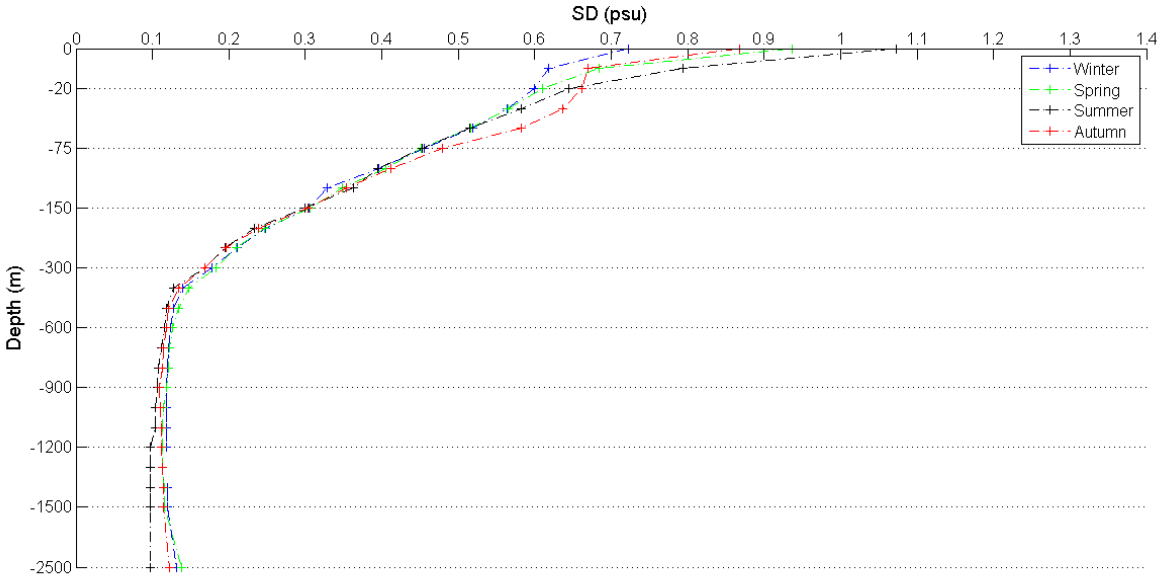

FIGURE 4.17: V5 salinty monthly profiles of Standard Deviation.

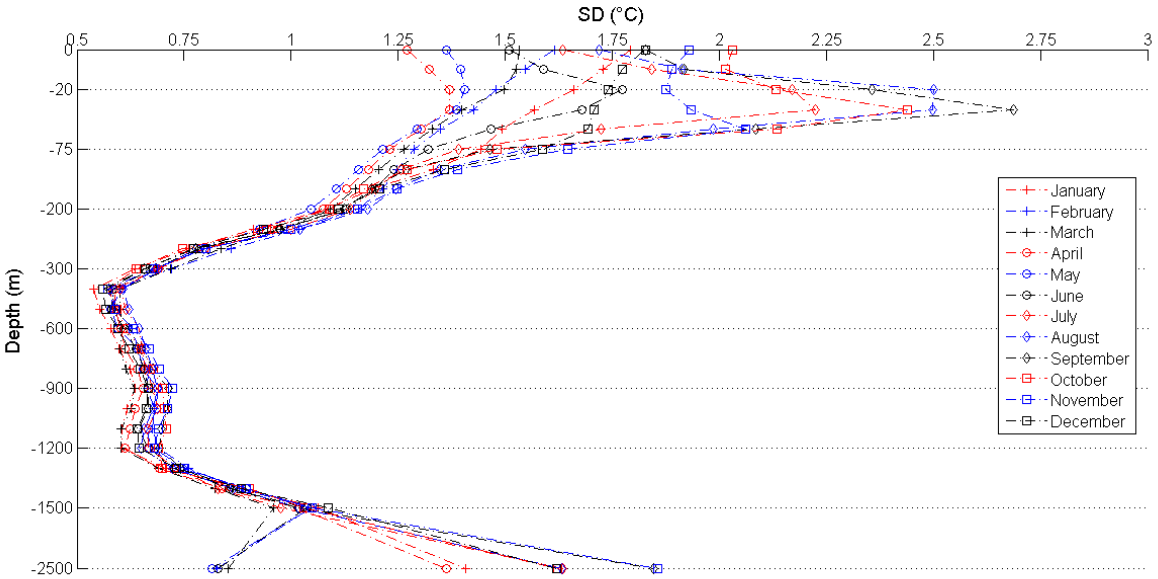

FIGURE 4.18: V3 temperature monthly profiles of Standard Deviation.

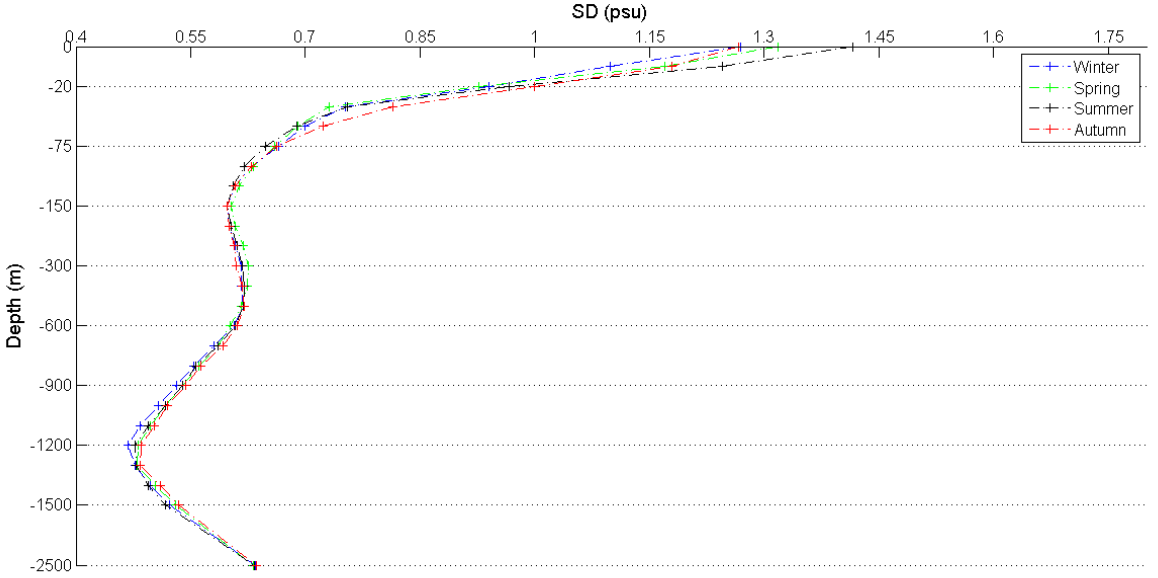

FIGURE 4.19: V3 salinity monthly profiles of Standard Deviation.

Let us consider two other statistical estimators to calculate the correspondence between the V5 and the V3 fields. The first is the Root Mean Square Difference (RMSD) that generally is used to compute the differences between the values predicted by a model and the values which are actually observed. In our case the model is represented by the V5 fields and the observed values by the V3 fields. We can write:

$$\mathrm{RMSD} = \frac{1}{N}\sqrt{\sum_{i=1}^{N}\left(\theta'_{i,j,V5} - \theta'_{i,j,V3}\right)^2} \tag{4.4}$$

with $\theta'_{i,j,V5}$ and $\theta'_{i,j,V3}$ the variables introduced below.

The second is the Mean Difference, defined as:

$$\mathrm{MD} = \frac{1}{N}\sum_{i=1}^{N}\left(\theta'_{i,j,V5} - \theta'_{i,j,V3}\right) \tag{4.5}$$

with $\theta'_{i,j,V5}$ and $\theta'_{i,j,V3}$ the variables introduced below.

To identify the correspondence between the two versions, in general, we must verify that:

$$\mathrm{RMSD} \leq \ \mathrm{SD}. \tag{4.6}$$

In Table 4.1 we present some examples of V5 SD, RMSD, and MD values for five depths. The last two columns of the table are the RMSD percentages with respect to the V5 SD values , and the MD percentages with respect to the V5 SD values, respectively. The values are very small: this indicates that the relation 4.6 is verified and we can conclude that there is a good correspondence between the V5 and V3 fields in this case.

Depth (m)	**SD (°C)**	**RMSD (°C)**	**MD °C**	**RMSD/SD (%)**	**MD/SD (%)**
0	1.13	0.0039	0.1515	0.34%	13.40%
50	1.18	0.0032	0.1083	0.27%	9.17%
100	1.08	0.0030	0.0718	0.26%	6.64%
500	0.35	0.0040	0.0140	1.14%	4.00%
2500	0.27	0.0193	0.0047	7.14%	1.74%

TABLE 4.1: Some SD, RMSD, and MD values for the V5 temperature fields.

Figure 4.20, 4.21, 4.22, and 4.23 show the temperature and salinity RMSD percentages with respect to the V5 SD values, and the MD and SD percentages with respect to the V5 SD values for all the depths considered in the analysis. Figure 4.24, 4.25, 4.26, and 4.27 show

the same quantities which respect to the V3. As shown in Table 4.1, the percentages are low in both versions for the majority of the depths. Only the bottom depths are excepted for the temperature cases. This is probably connected to the different background fields used in the analysis.

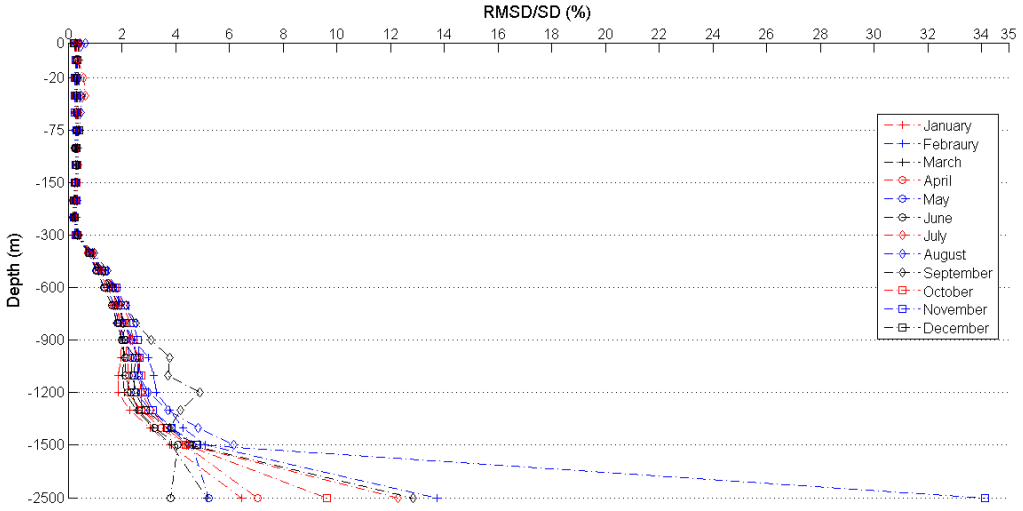

FIGURE 4.20: Temperature RMSD percentages with respect to the V5 SD.

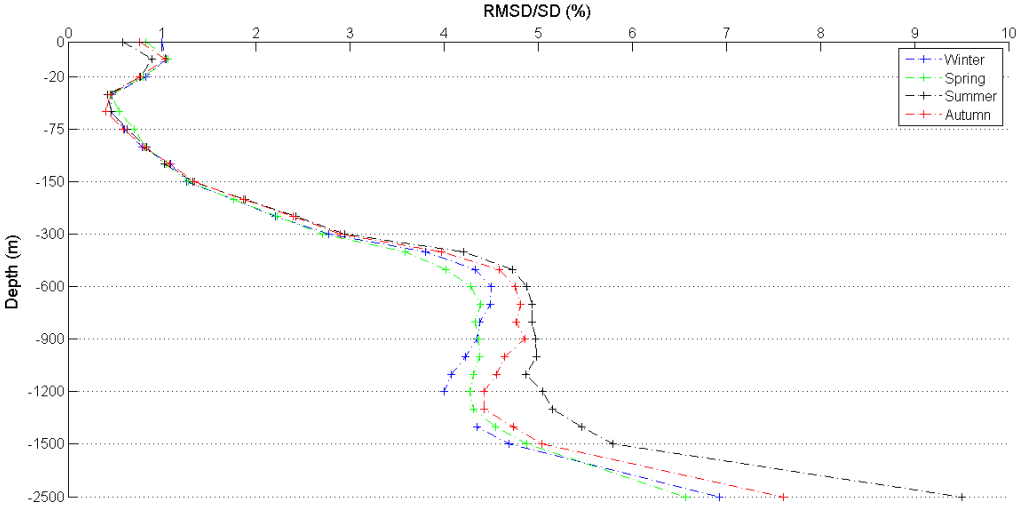

FIGURE 4.21: Salinity RMSD percentages with respect to the V5 SD.

Therefore we can conclude that the correspondence between the two climatology version is very close, and the V5 fields are good in the type 2 sense.

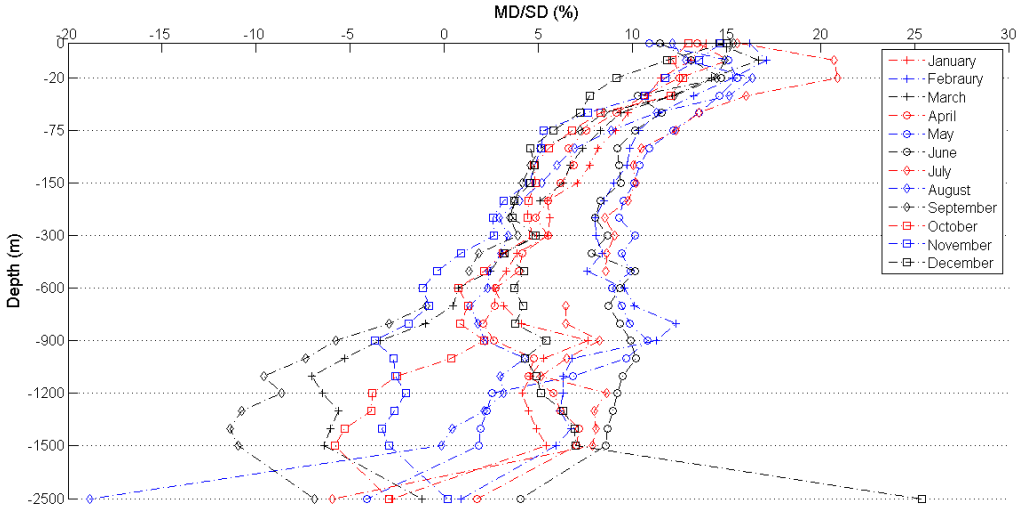

FIGURE 4.22: Temperature MD percentages with respect to the V5 SD.

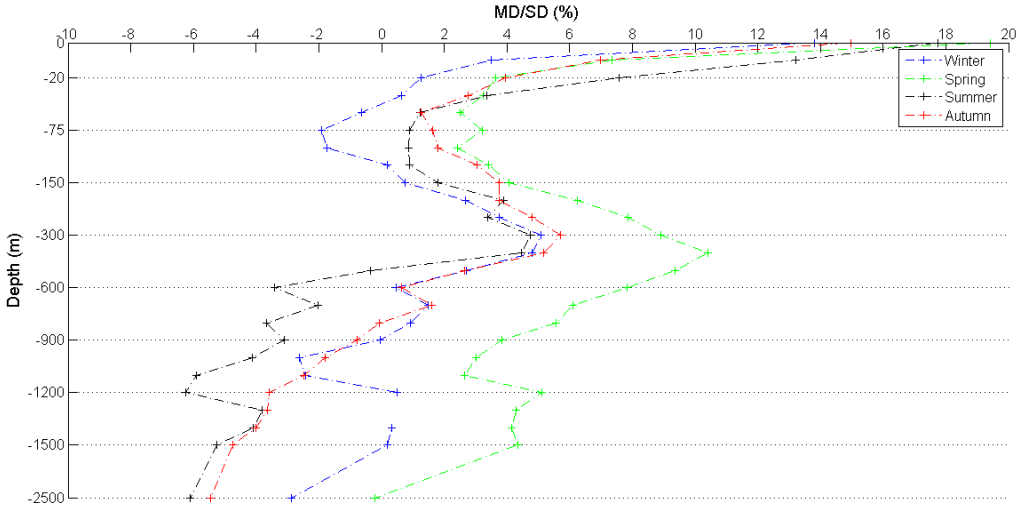

FIGURE 4.23: Salinity MD percentages with respect to the V5 SD.

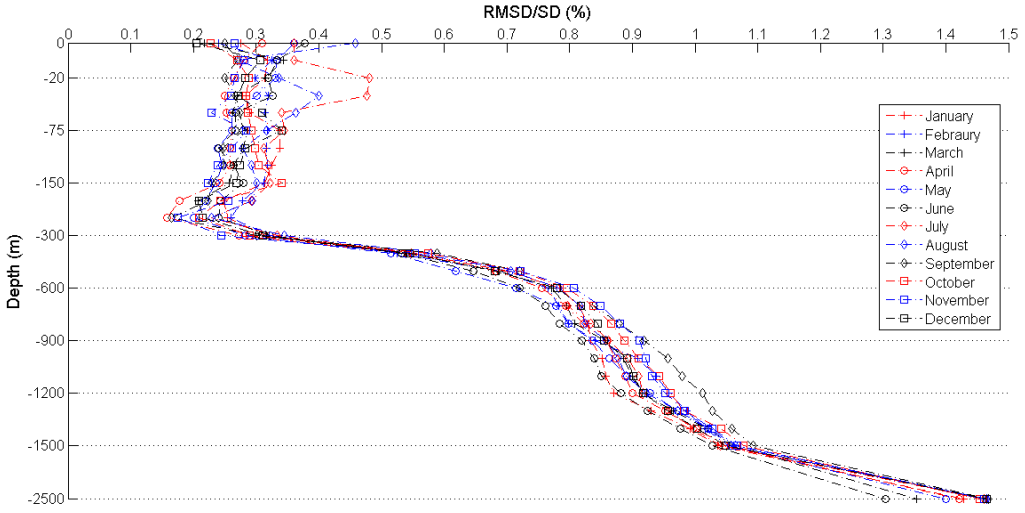

FIGURE 4.24: Temperature RMSD percentages with respect to the V3 SD.

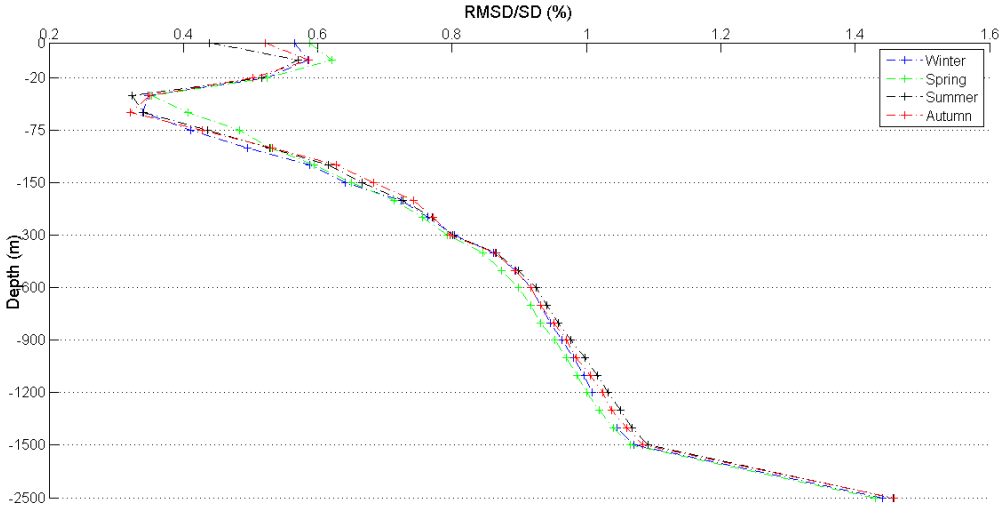

FIGURE 4.25: Salinity RMSD percentages with respect to the V3 SD.

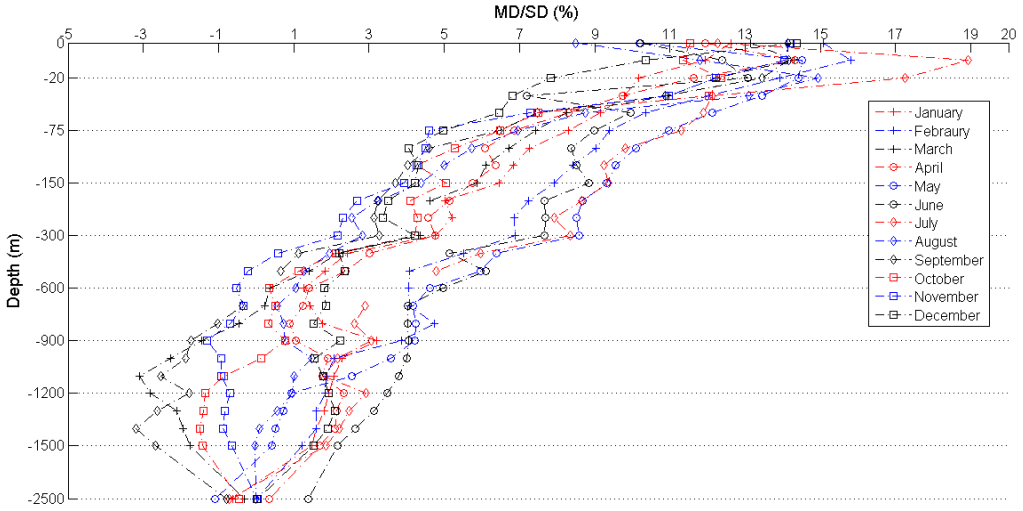

FIGURE 4.26: Temperature MD percentages with respect to the V3 SD.

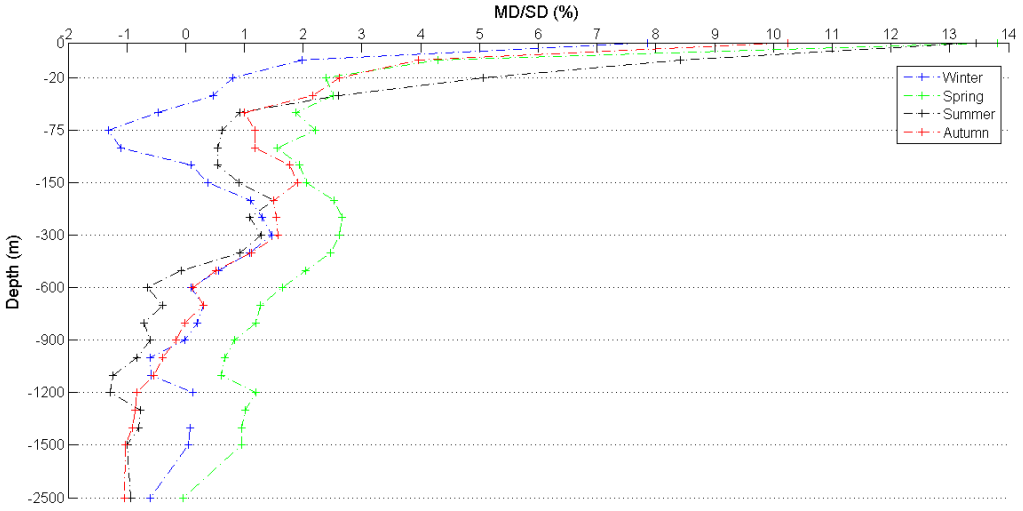

FIGURE 4.27: Salinity MD percentages with respect to the V3 SD.

This page is intentionally left blank.

Chapter 5

Seasonal cycle

In this chapter we present the most important result of this thesis: the temperature and salinity seasonal cycle in the Mediterranean Sea.

The seasonal cycle represents the change of the temperature and salinity mean values, related to general water circulation and the atmospheric characteristics. The major factor that determines the temperature seasonal cycle is the seasonal cycle of the solar radiation. For salinity, we can consider two major causes: evaporation and the river runoff. It is important to point out that there are two types of evaporation: the summer evaporation, related to the high solar radiation; the winter evaporation, associated to the winds. To show our results we divide the Mediterranean in thirteen regions, specified in Figure 2.14.

Let us start from region 1, the Alboran Sea. Figure 5.1a shows the temperature monthly mean values for five depths . As one can notice the surface temperature trend presents the most evident seasonal change. The lowest value is about $14.7°C$ in January and the highest is about $24.5°C$ in August, with a difference of about $9.8°C$ between the maximum and the minimum. For the temperature trend at 50 m the seasonal range of values is smaller. It is important to notice that in the first three months the temperature values at 50m are higher than the surface values: this is related to the entering of the Atlantic Water from the Strait of Gibraltar. For the other depths, the seasonal curves are nearly constant.

Figure 5.1b shows the salinity seasonal mean values for five depths. Also in this case, the surface temperature curve presents a distinct seasonal change. The highest value is about 37.25 psu and the lowest value is 36.75 psu. The difference between these two values is about 0.5 psu; we can

conclude that the salinity seasonal cycle is less marked than the temperature seasonal cycle. For the other depths the trend is constant.

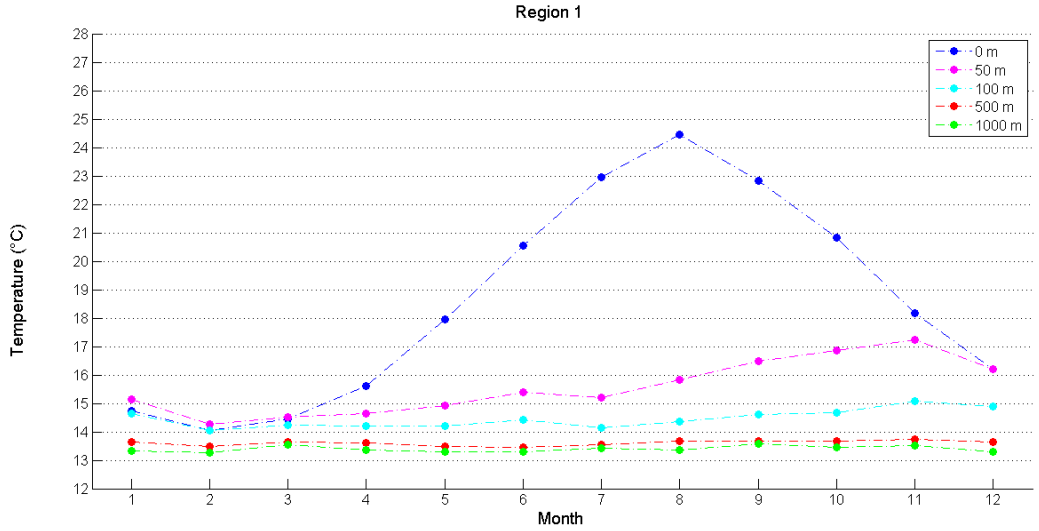

(a) Temperature mean values of region 1

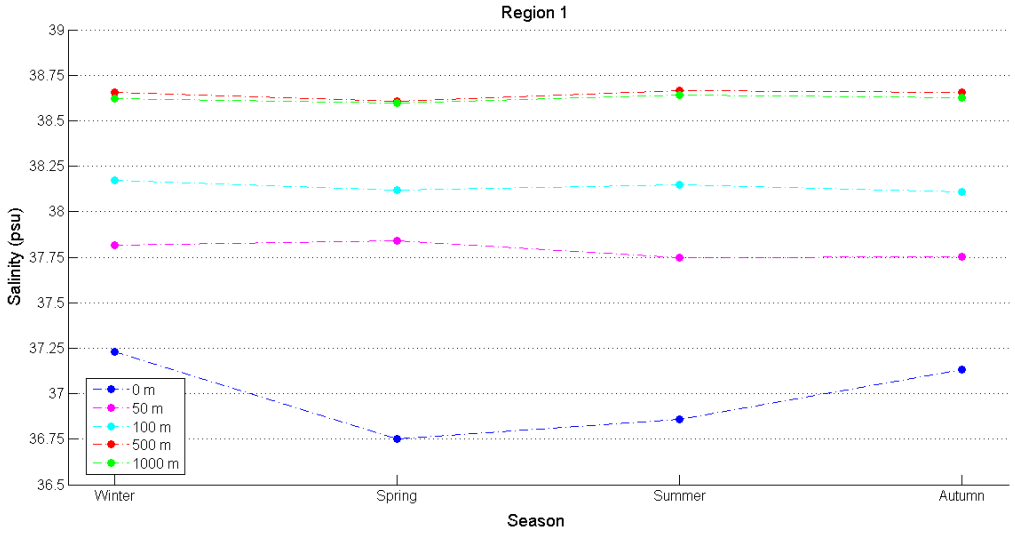

(b) Salinity mean values of region 1

FIGURE 5.1: Temperature and salinity mean values of region 1.

Figure 5.2a and Figure 5.2b show, respectively, the temperature and salinity seasonal variability of region 2, the Algerian basin. This zone presents characteristics similar to the previous region but the difference between the surface highest and lowest values of temperature is greater than in region 1, and equal to about $10°C$. On the contrary, the salinity presents a difference which is much smaller than in region 1 and equal to about 0.1 psu. Also in this case the curves of the other depths are constant.

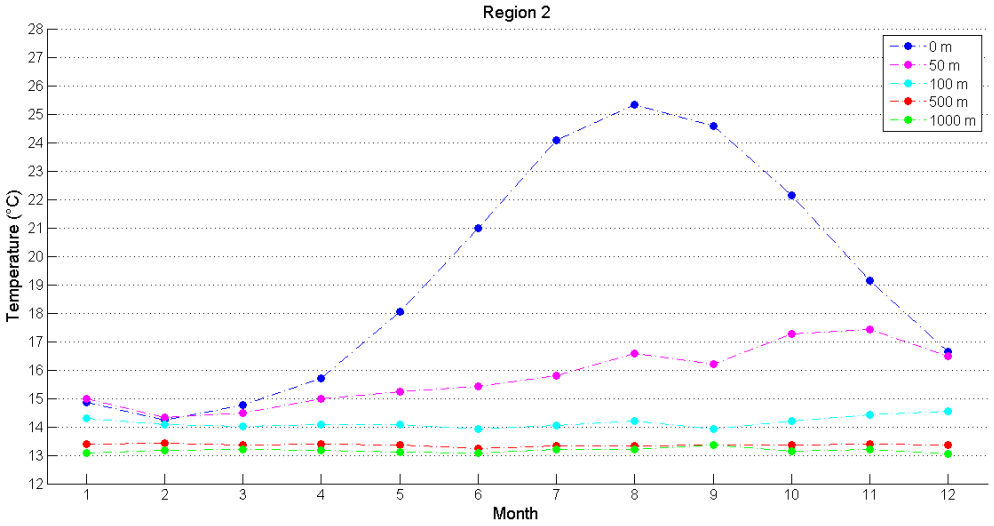

(a) Temperature mean values of region 2

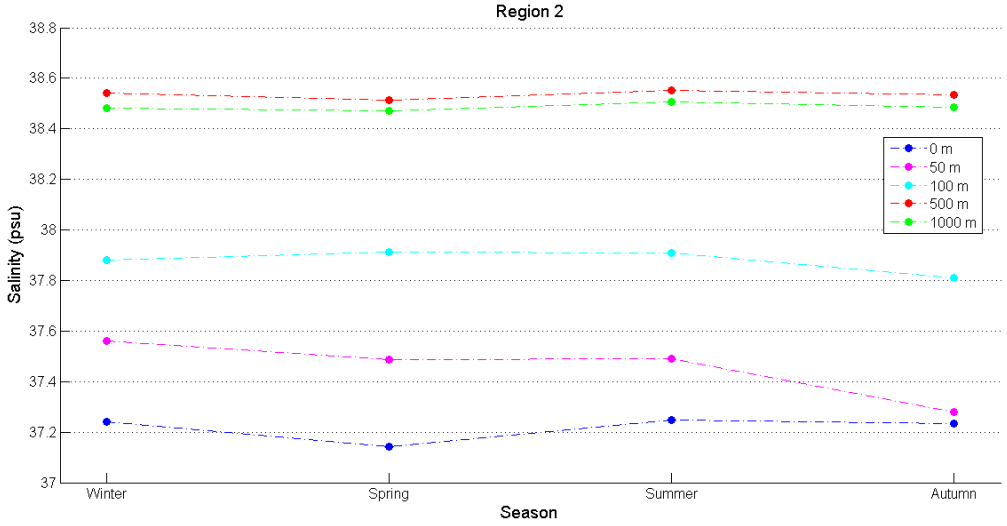

(b) Salinity mean values of region 2

FIGURE 5.2: Temperature and salinity mean values of region 2.

The temperature and salinity seasonal variability of region 3, that includes the Balearic Sea and the Gulf of Lions, present the same characteristics shown in the previous cases, as shown in Figure 5.3a and Figure 5.3b, respectively. For the temperature surface, we can calculate a difference between the highest and lowest value of about $11°C$; for salinity about 0.2 psu. The lowest salinity value, as in the previous cases, occurs in spring.

The characteristics of the temperature and salinity seasonal cycle of region 4, the Tyrrhenian Sea, for the five depths are similar to those of the other western regions, as shown in Figure 5.4a and Figure 5.4b. There is a distinctive trait in summer, when we observed the highest salinity

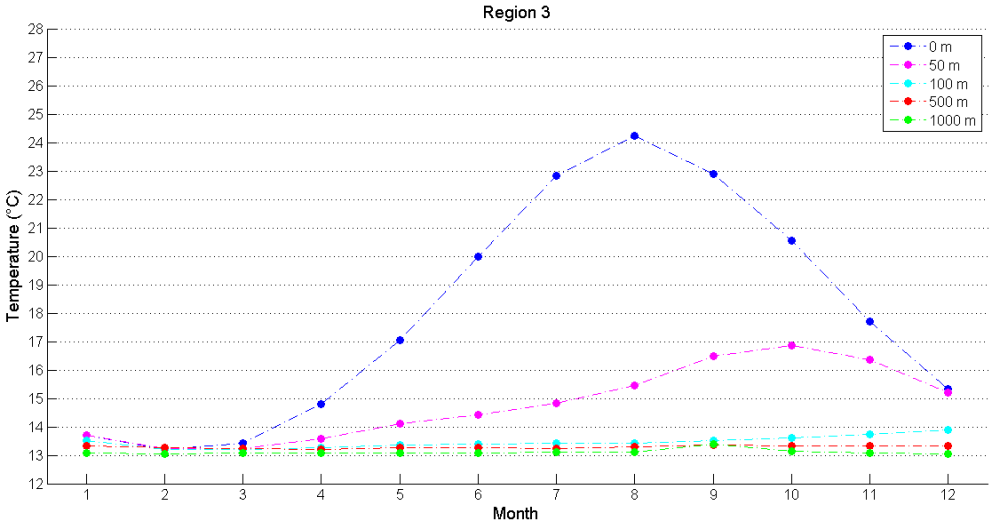

(a) Temperature mean values of region 3

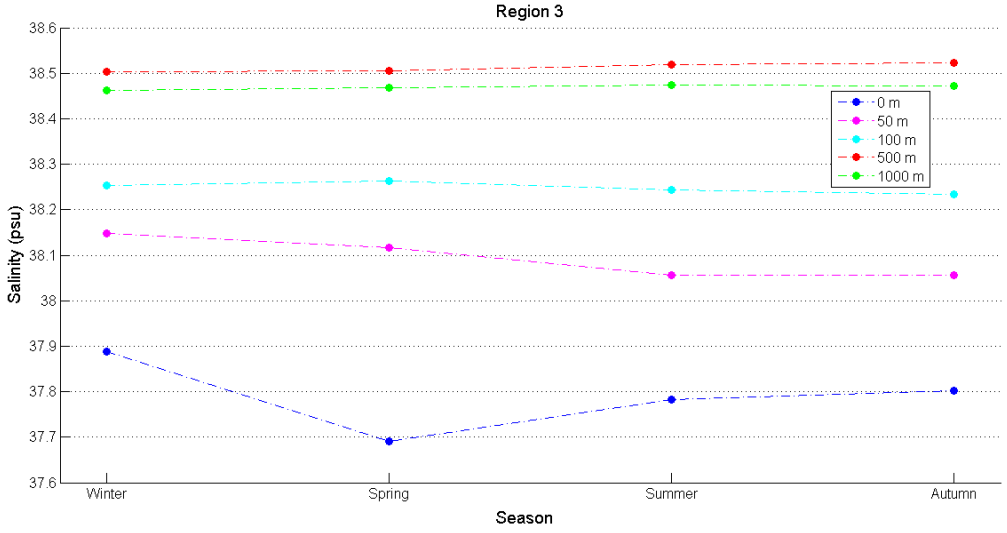

(b) Salinity mean values of region 3

FIGURE 5.3: Temperature and salinity mean values of region 3.

value, about 37.85 psu, related to evaporation. Also in this case, the surface temperature value in winter is lower than the temperature value at 50 m, because of the entering of the Atlantic Water.

The temperature and salinity seasonal variability of region 5, the Adriatic Sea, are shown in Figure 5.5a and Figure 5.5b, respectively. It is important to notice that the temperature surface values are lower than the other depths during the first three months. This event seems to be incongruous with the typical behaviour of the water masses. In fact cold water tends to go upwards because of its lower density value; on contrary the warm water tends to go downwards.

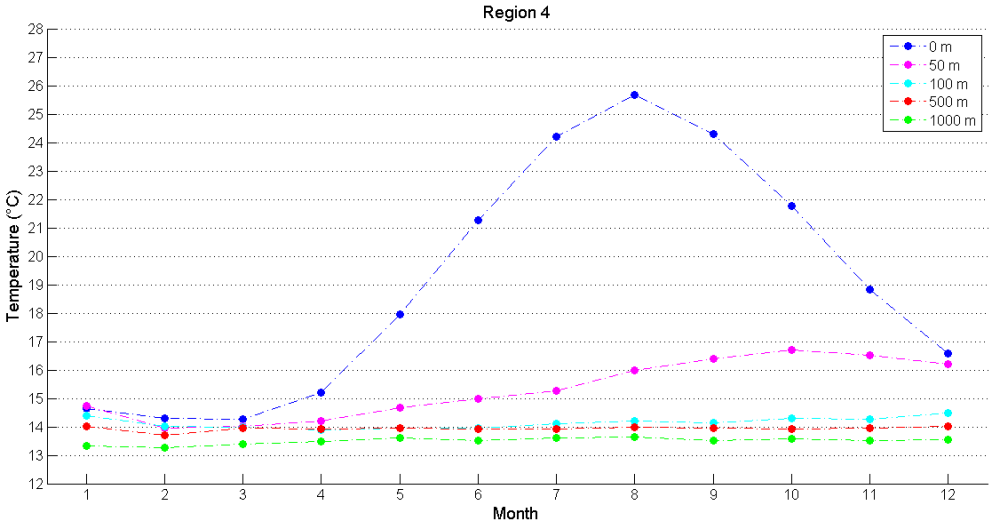

(a) Temperature mean values of region 4

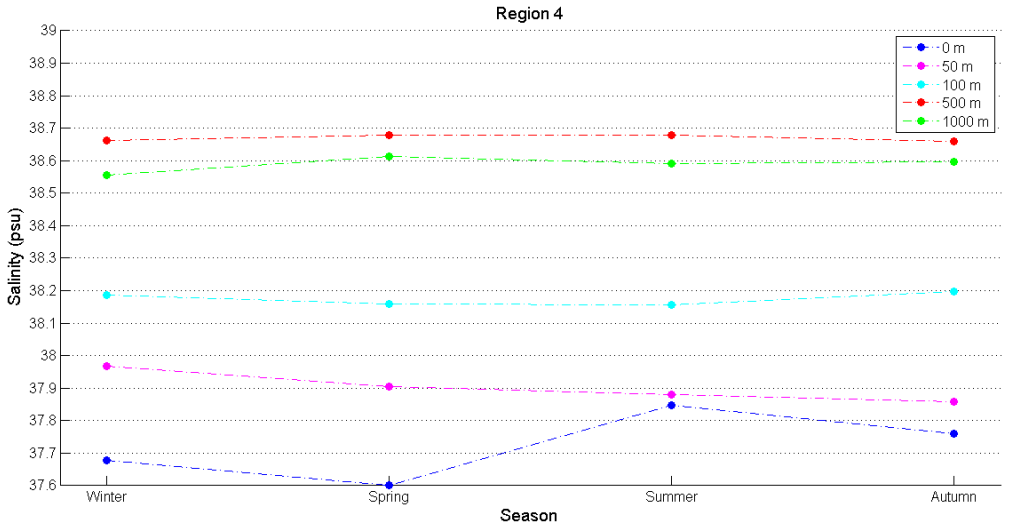

(b) Salinity mean values of region 4

FIGURE 5.4: Temperature and salinity mean values of region 4.

In our case this event is possible because the water density is also related to the salinity value. The relation between density, temperature and salinity for a water mass is:

$$\rho = \rho_0 + \rho_{ref}\left[-\alpha_T(T - T_0) + \beta(S - S_0)\right] \tag{5.1}$$

with:

$$\alpha_T = -\left(\frac{\partial\rho}{\partial T}\right)_S \frac{1}{\rho_{ref}}, \beta = \left(\frac{\partial\rho}{\partial S}\right)_T \frac{1}{\rho_{ref}}. \tag{5.2}$$

It is possible to notice that the temperature sign is opposite to the salinity one. This allows

the salinity value to counterbalance the temperature value. In fact the highest values of salinity occur in winter and autumn, when the temperature surface values are lower.

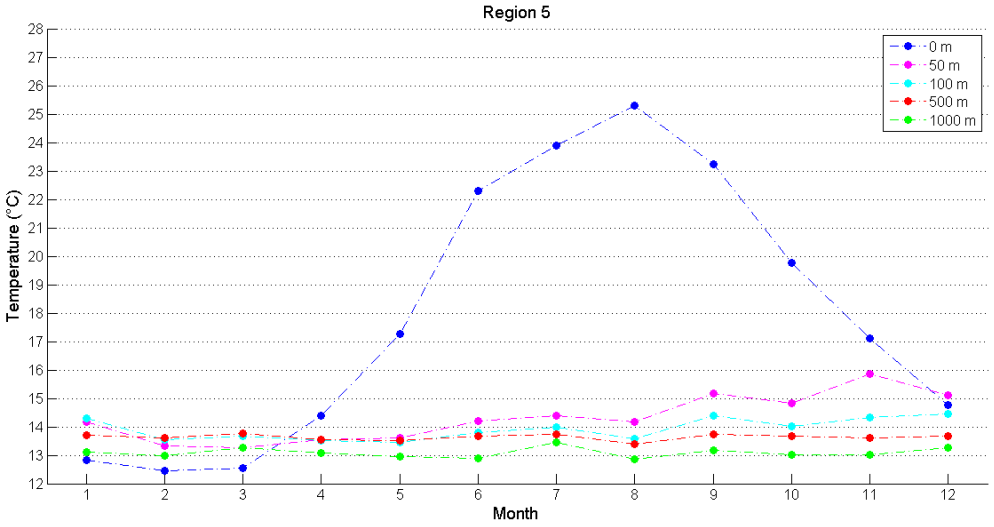

(a) Temperature mean values of region 5

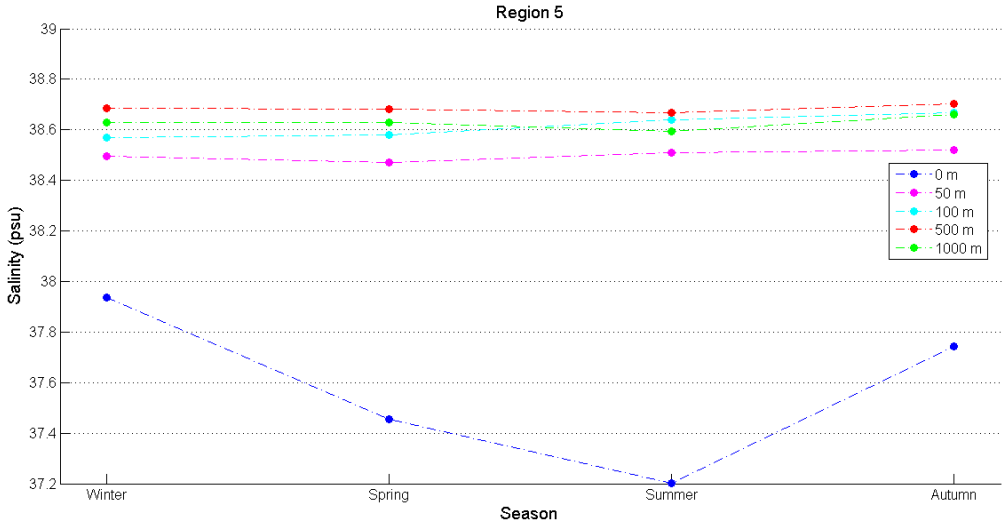

(b) Salinity mean values of region 5

FIGURE 5.5: Temperature and salinity mean values of region 5.

The temperature and salinity seasonal variability of region 6, the Ionian Sea, are shown in Figure 5.6a and Figure 5.6b, respectively. As for the temperature curves, we have the same trend of the previous regions. The salinity variability is quite different at surface. The maximum occurs in summer because of evaporation, and the minimum in autumn for the coming of the Atlantic Water.

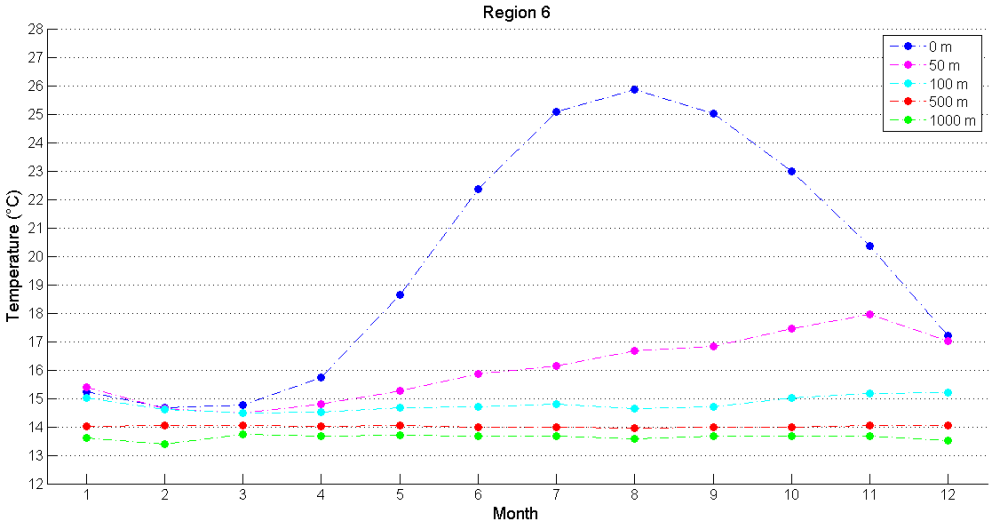

(a) Temperature mean values of region 6

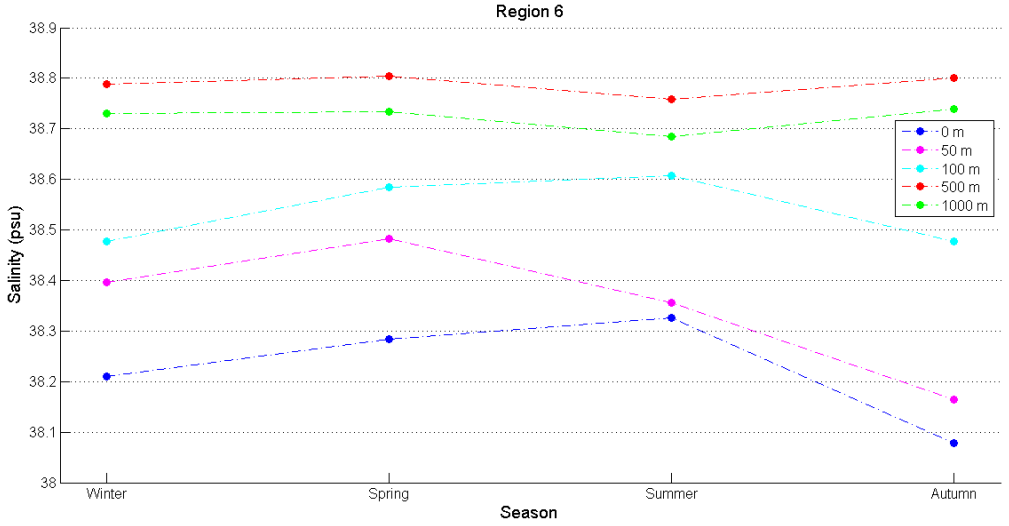

(b) Salinity mean values of region 6

FIGURE 5.6: Temperature and salinity mean values of region 6.

The temperature and salinity seasonal variability of region 7 and region 8 are shown in Figure 5.7a, 5.7b, 5.8a and 5.8b, respectively. The temperature and salinity curves present the same characteristics show in the previous cases whereas, differently from the previous cases, the maximum temperature value is about $27°C$. In both regions, the highest value of salinity at surface occurs in summer and exceeds the salinity value at 50 m.

Let us now consider the temperature and salinity seasonal variability of region 9, the Aegean Sea, shown in Figure 5.9a and Figure 5.9b, respectively. We can notice that the surface temperature values during winter are lower than the values at 50 and 100 m. This is related to the same

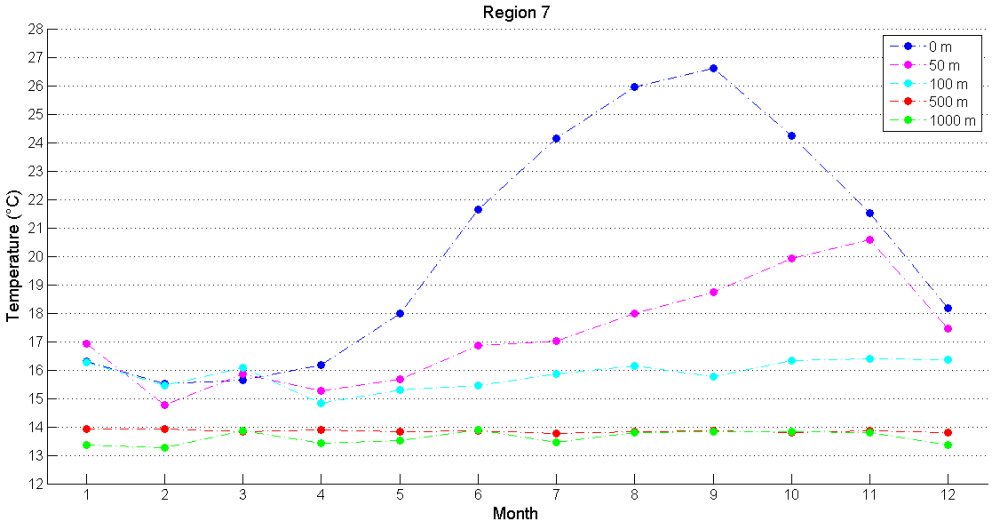

(a) Temperature mean values of region 7

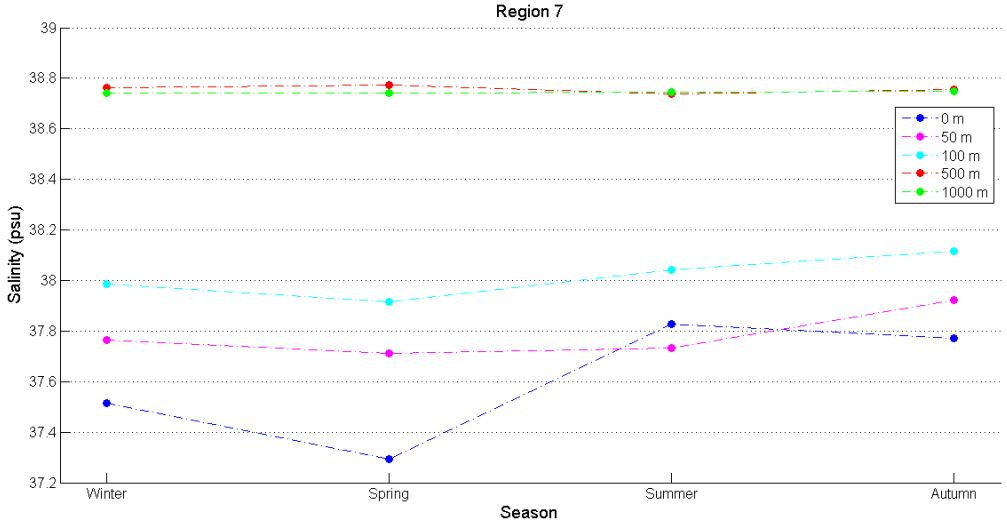

(b) Salinity mean values of region 7

FIGURE 5.7: Temperature and salinity mean values of region 7.

physical process described for region 5. For the rest of the months, the seasonal variability of region 9 is similar to the other regions.

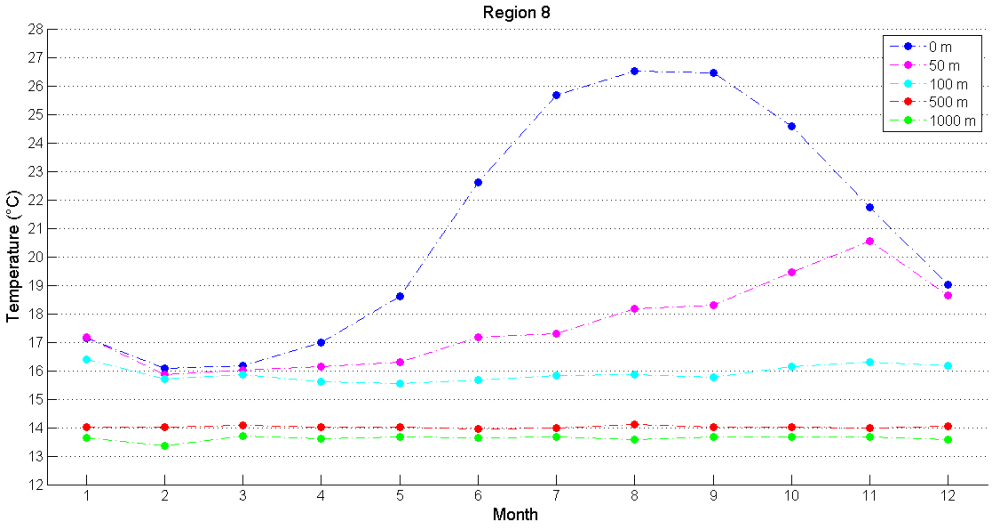

(a) Temperature mean values of region 8

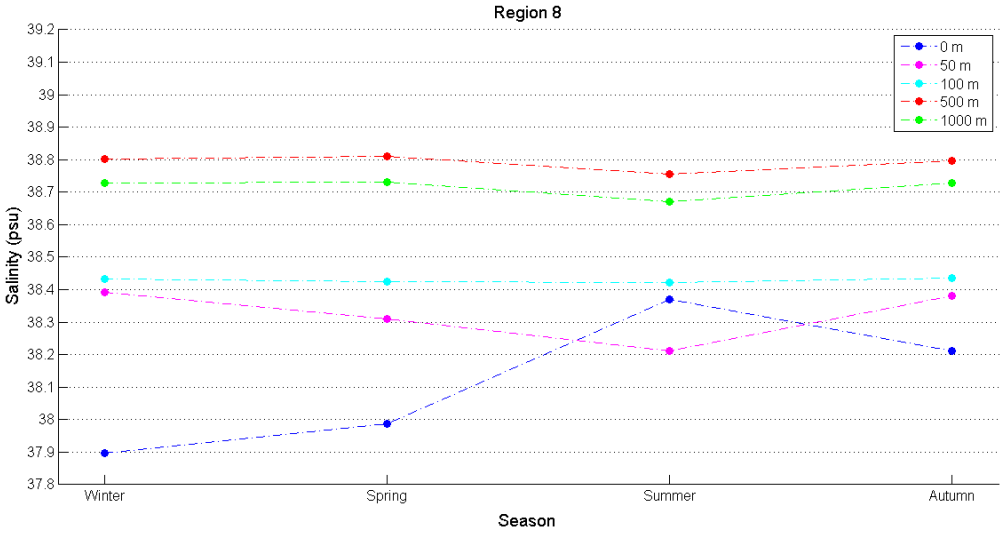

(b) Salinity mean values of region 8

FIGURE 5.8: Temperature and salinity mean values of region 8.

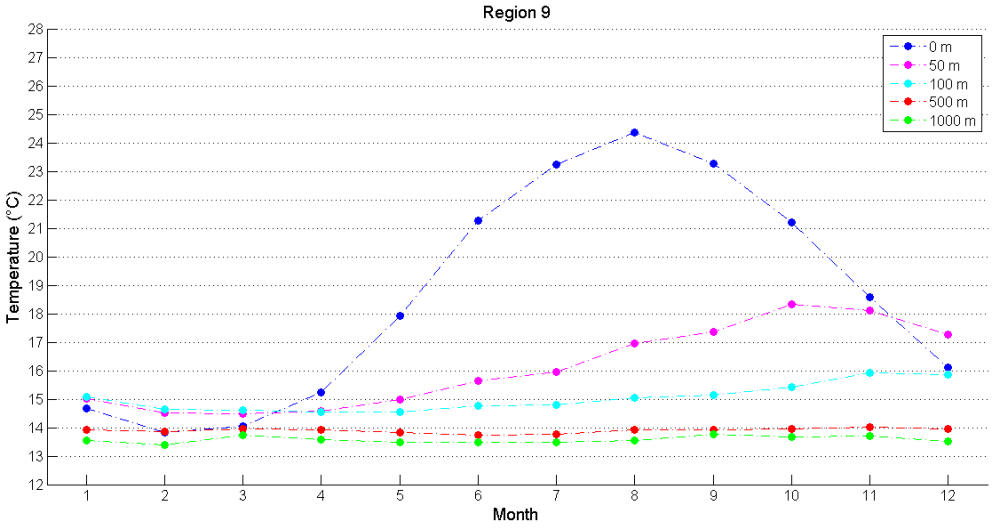

(a) Temperature mean values of region 9

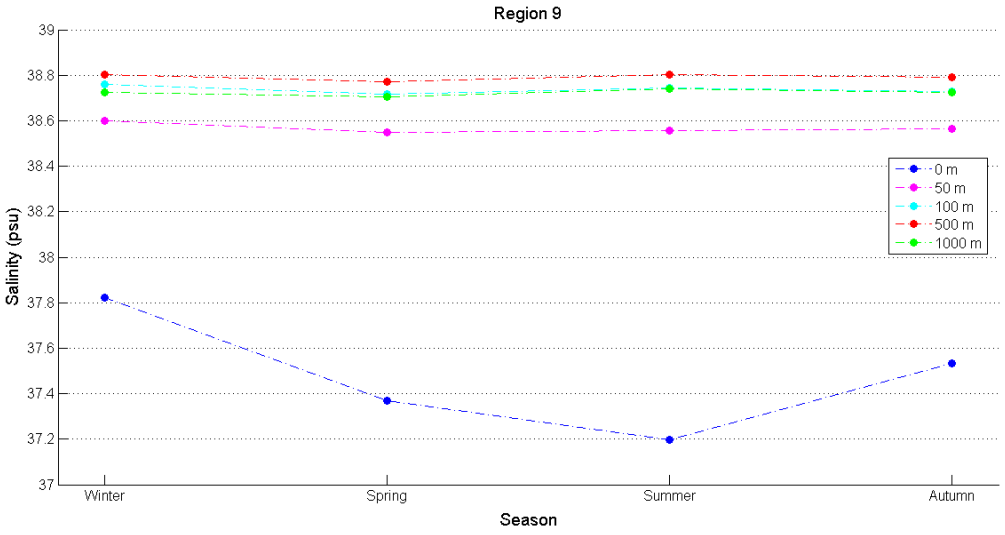

(b) Salinity mean values of region 9

FIGURE 5.9: Temperature and salinity mean values of region 9.

As for regions 10, 11, 12 and 13, as shown in Figures 5.10a, 5.10b, 5.11a, 5.11b, 5.12a, 5.12b, 5.13a, 5.13b, they have similar temperature seasonal variability, as well as a similar salinity seasonal variability. The temperature curves present the lowest values in winter and spring and the highest values in summer, as the salinity curves. The latter result is related to evaporation. The similar trend of these four region is connected to their geographical location, the Levantine basin.

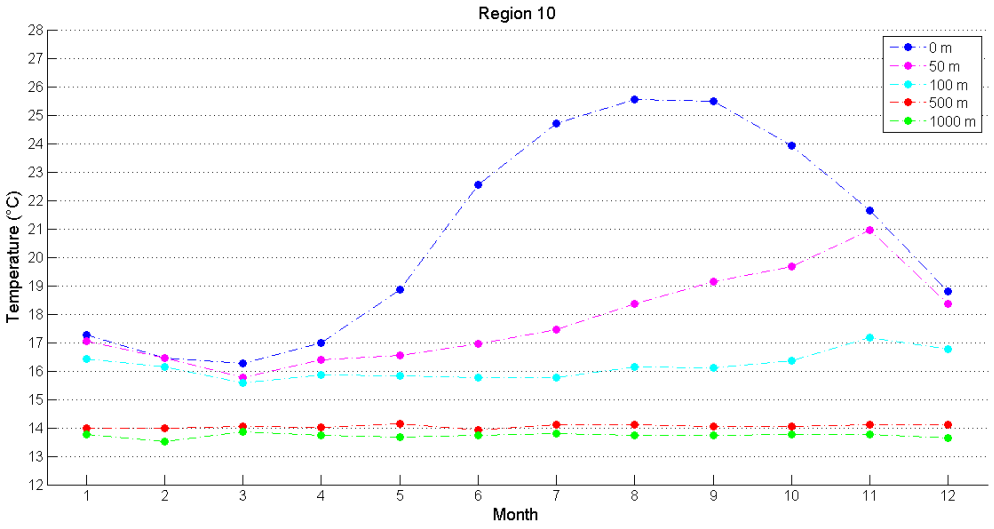

(a) Temperature mean values of region 10

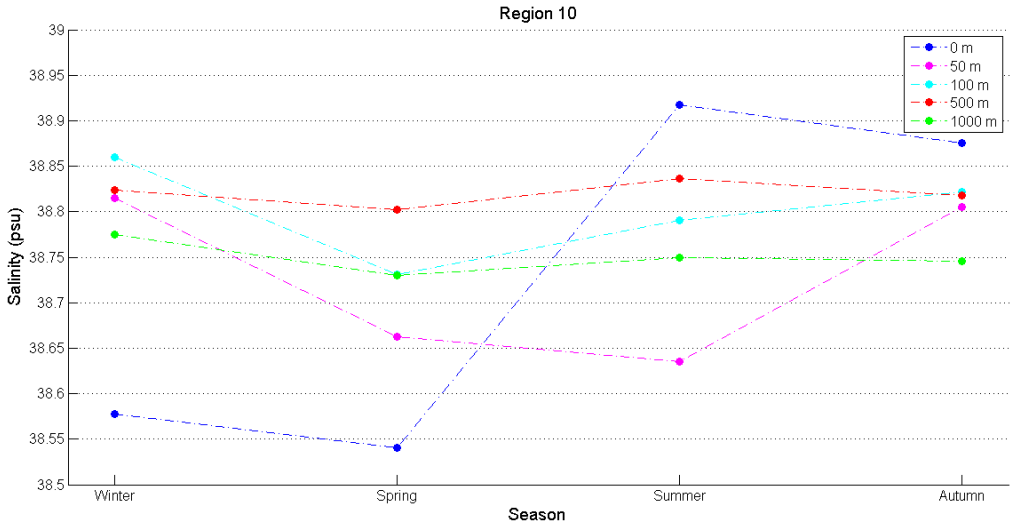

(b) Salinity mean values of region 10

FIGURE 5.10: Temperature and salinity mean values of region 10.

Let us now compare our seasonal cycle with the northeast United States Atlantic water seasonal cycle at surface, to show that this is a general characteristic for the water masses at our latitude.

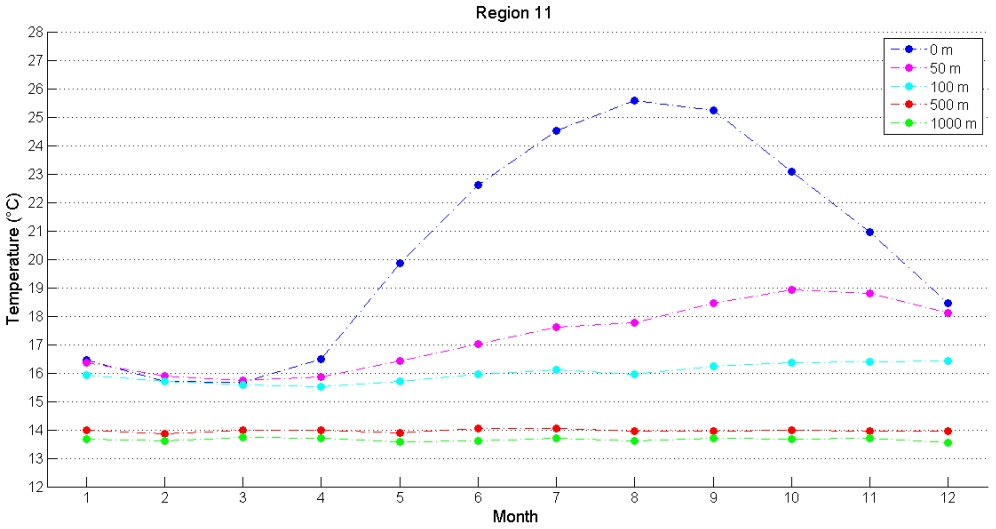

(a) Temperature mean values of region 11

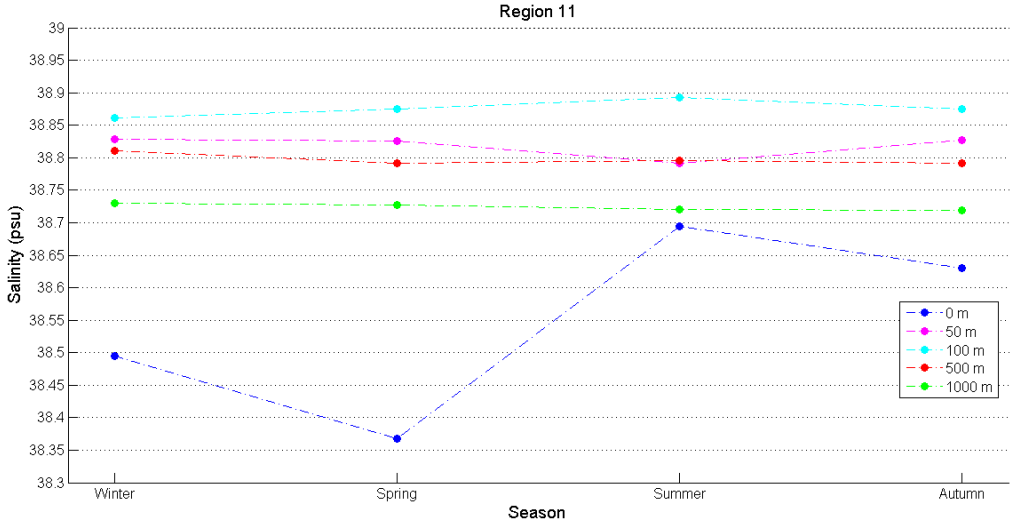

(b) Salinity mean values of region 11

FIGURE 5.11: Temperature and salinity mean values of region 11.

In Figure 5.14 we can see the temperature mean values during the year in the East (GOME) and West (GOMW) part of the Gulf of Maine at the surface. As in the Mediterranean the temperature changes heavily across seasons within a range between about $4°C$ and about $20°C$.

Figure 5.15 shows the salinity mean values during months in the GOME and GOMW regions. As in the Mediterranean, the salinity changes more softly, and the difference between the values is about 1 psu.

Therefore we can conclude that in general, at our latitude, the temperature seasonal cycle is more marked than the salinity seasonal cycle.

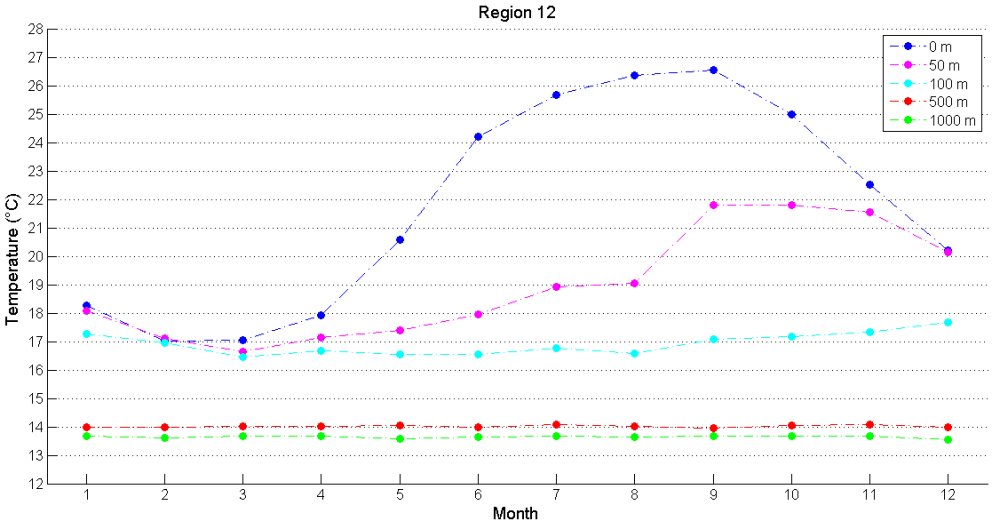

(a) Temperature mean values of region 12

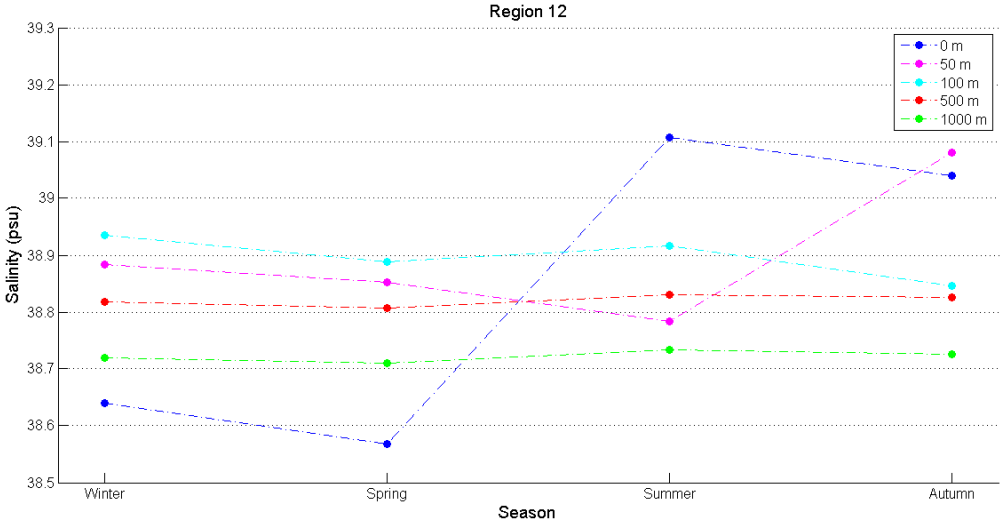

(b) Salinity mean values of region 12

FIGURE 5.12: Temperature and salinity mean values of region 12.

In the entire Mediterranean we can compute a temperature mean seasonal cycle of about $16°C$, whereas the salinity mean seasonal cycle is only of about 3 psu.

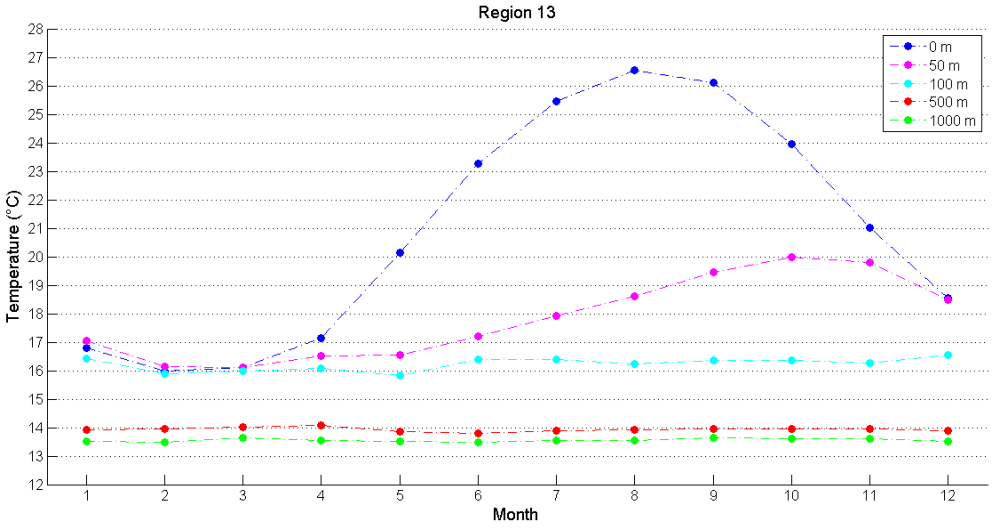

(a) Temperature mean values of region 13

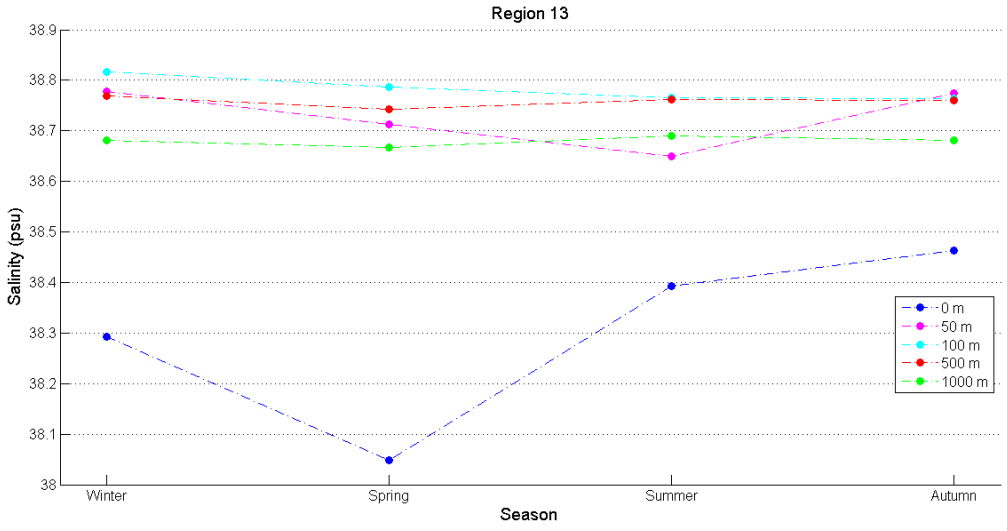

(b) Salinity mean values of region 13

FIGURE 5.13: Temperature and salinity mean values of region 13.

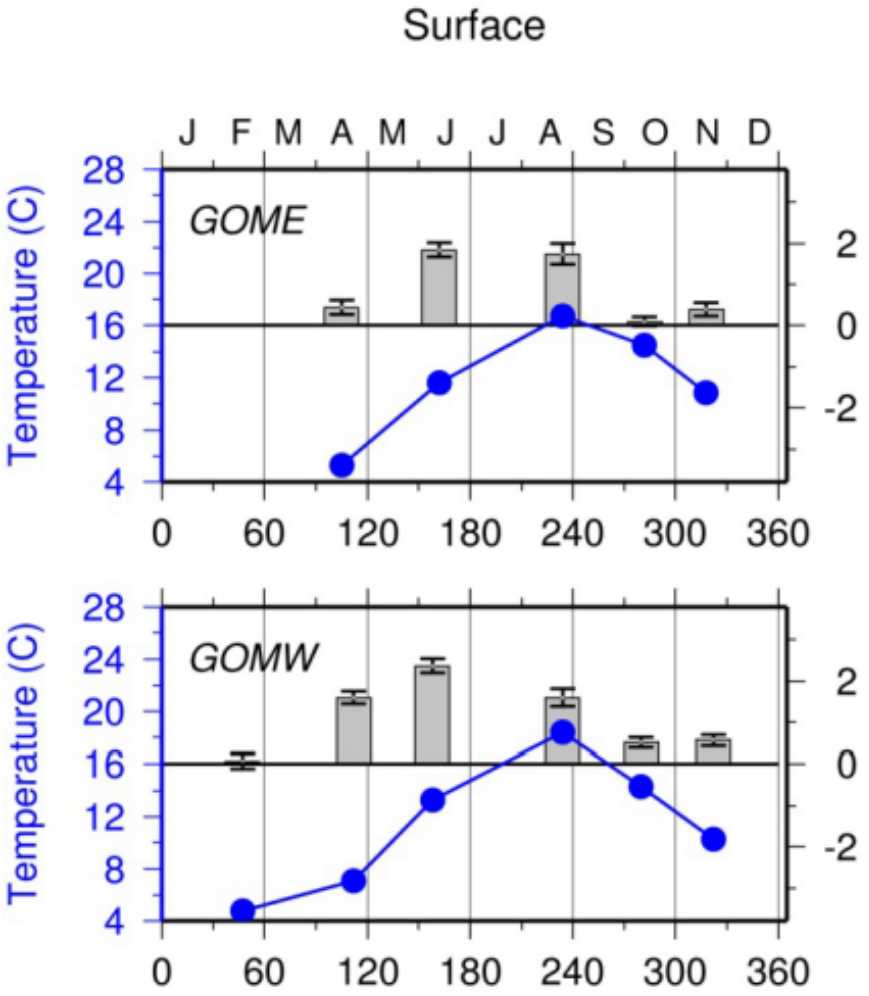

FIGURE 5.14: Temperature means at surface in the Gulf of Maine as a function of calendar day.
Source: Fratantoni *et al*, Description of the 2010 Oceanographic Conditions on the Northeast U.S. Continental Shelf

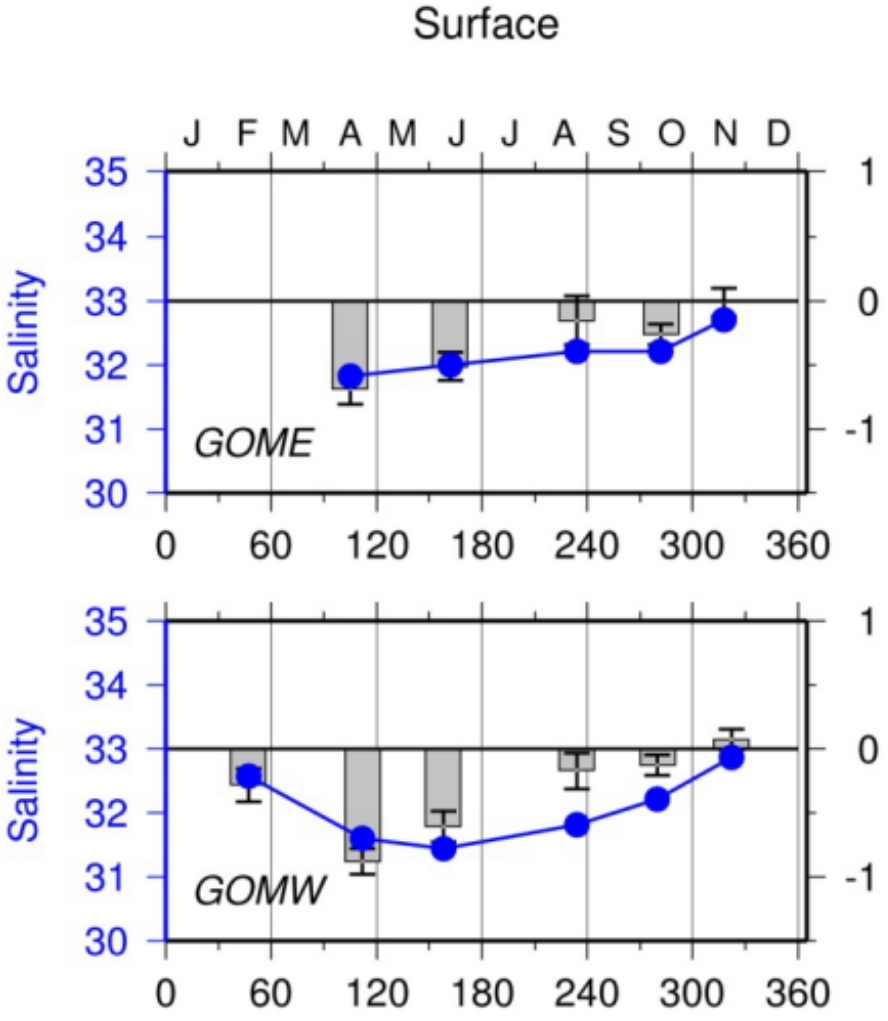

FIGURE 5.15: Salinity means at surface in the Gulf of Maine as a function of calendar day.
Source: Fratantoni *et al*, Description of the 2010 Oceanographic Conditions on the Northeast U.S. Continental Shelf

Concluding remarks

The aim of climatological analysis was to produce new temperature and salinity climatologies for the period 1900-2013 and describe the temperature and salinity seasonal cycle for that period in the Mediterranean Sea.

After introducing a few studies on the Mediterranean Sea climatological water masses and the general circulation, and a brief description of the instruments used for the ocean observations (Chapter 1), the SeaDataNet 2 dataset, used for the analysis, is described together with a few remarks on temporal and spatial characteristics of the data (Chapter 2). Furthermore the eight general principles of the quality control of the data set have been presented.

Chapter 3 presents the vertical and horizontal interpolation algorithms and techniques. The inhomogeneuos vertical and spatial distribution of data is the kernel of the gridding problem. Therefore it is necessary to introduce some interpolation techniques to solve it and produce the climatologies. The Variational Optimal Interpolation Technique, implemented in the DIVA algorithm, is the most important method to spatially interpolate data on a regular grid.

Chapter 4 deals with the results of the climatological analysis. The temperature and salinity maps were presented with the background fields used in the analysis and the relative error maps. Furthermore a comparison between our climatologies and a previous climatological version is performed, following the goodness criteria introduced by Murphy (1993) for weather forecasts. According to this comparison, our gridded fields are good.

In Chapter 5 the temperature and salinity seasonal cycle is described divided by the thirteen regions of the Mediterranean Sea, and a comparison with the North Atlantic temperature and salinity seasonal cycle is performed. From our results we can conclude that the temperature seasonal cycle at our latitude is more marked with respect to the salinity seasonal cycle and this is especially related to the solar radiation seasonal cycle.

This page is intentionally left blank.

Appendix A

Vertical interpolation python script

In this Appendix we present the python program for the vertical interpolation of the dataset that it is described in Section 3.1.

```
REQUESTED_DEPTHS = range(0, 5501, 10)

def findNearest(list, val):
prev = None
next = None
for i in xrange(0, len(list) - 1):
  if list[i] <= val and list[i + 1] >= val:
    prev = i
    next = i + 1
    break
return [prev, next]

def linear_interpolation(x0, x1, y0, y1, k):
    return y0 + ((y1 - y0) / (x1 - x0)) * (k - x0);

MAX_OFFSET = 5

def interpolate(measurements):

  depths = [float(elem[0]) for elem in measurements]
  temperatures = [float(elem[1]) for elem in measurements]
  salinities = [float(elem[2]) for elem in measurements]

  def processTemperature(depth, prev, next):
    return linear_interpolation(depths[prev], depths[next], temperatures[prev], \
      temperatures[next], depth)

  def processSalinity(depth, prev, next):
```

```
  return linear_interpolation(depths[prev], depths[next], salinities[prev], \
    salinities[next], depth)

result = []

for depth in REQUESTED_DEPTHS:
  if depth == 0:
    if len(depths) != 0 and depths[0] <= MAX_OFFSET:
      row = [depth, temperatures[0], salinities[0]]
      result.append(row)
  else:
    [prev, next] = findNearest(depths, depth)
    if prev != None and next != None:
      prevDiff = math.fabs(depths[prev] - depth);
      nextDiff = math.fabs(depths[next] - depth);
      if prevDiff <= MAX_OFFSET and nextDiff <= MAX_OFFSET:
        try:
          row = [depth, processTemperature(depth, prev, next), \
            processSalinity(depth, prev, next)]
          result.append(row)
        except ZeroDivisionError:
          print(''Division by zero'')

return result
```

Bibliography

[1] P. Brasseur, J. M. Beckers, J. M. Brankart, and R. Schoenauen. Seasonal temperature and salinity fields in the mediterranean sea: Climatological analyses of a historical data set. *Deep-Sea Research I*, 43(2):159–192, 1996.

[2] I. M. Ovchinnikov. Circulation in the surface and intermediate layers of the mediterranean. *Oceanology*, (6):49–59, 1966.

[3] P. Malanotte-Rizzoli and A. Hecht. Large-scale properties of the eastern mediterranean: a rewiew. *Oceanologica Acta*, 11(4):323–335, 1988.

[4] The POEM group (Physical Oceanography of the Eastern Mediterranean): A. R. Robinson, P. Malanotte-Rizzoli, A. Hecht, A. Michelato, W. Roether, A. Theocharis, Ü. Ünlüata, N. Pinardi, A. Artegiani, A. Bergamasco, J. Bishop, S. Brenner, S. Christianidis, M. Gacic, D. Georgopoulos, M. Golnaraghi, M. Hausmann, H. G. Junghaus, A. Lascaratos, M. A. Latif, W. G. Leslie, C. J. Lozano, T. Oğuz, E. Özsoy, E. Papageorgiou, E. Paschini, Z. Rozentroub, E. Sansone, P. Scarazzato, R. Schlitzer, G. C. Spezie, E. Tziperman, G. Zodiatis, L. Athanassiadou, M. Gerges, and M. Osman. General circulation of the eastern mediterranean. *Earth-Science Reviews*, 32:285–309, 1992.

[5] A. Hecht, N. Pinardi, and A. R. Robinson. Currents, water masses, eddies and jets in the mediterranean levantine basin. *Journal of Physical Oceanography*, 18(10):1320–1353, 1988.

[6] S. Levitus. *Climatological atlas of the world ocean.* NOAA Prof Paper 13, US Government Printing Office, Washington, D.C., 173 pp., 1982.

[7] P. Picco. *Climatological atlas of the western Mediterranean.* ENEA Santa Teresa Center, La Spezia, Italy, 224 pp., 1990.

[8] C. Maillard, E. Balopoulos, A. Giorgetti, M. Fichaut, A. Iona, M. Larour, A. Latrouite, B. Manca, G. Maudire, P. Nicolas, and J. A. Sanchez-Cabeza. An integrated system for managing multidisciplinary oceanographic data collected in the mediterranean sea during the basin-scale research project eu/mast-mater (1996–2000). *Journal of Marine Systems*, 33(34), 2002.

[9] J.M Brankart and P. Brasseur. The general circulation in the mediterranean sea: a climatological approach. *Journal of Marine Systems*, 18:41–70, 1998.

[10] B. Klein, W. Roether, B. B. Manca, D. Bregant, V. Beitzel, V. Kovacevic, and A. Luchetta. The large deep water transient in the eastern mediterranean. *Deep-Sea Research*, I(46):371–414, 1999.

[11] N. Pinardi and et al. Mediterranean sea large-scale low-frequency ocean variability and water mass formation rates from 1987 to 2007: A retrospective analysis. *Prog. Oceanogr.*, 2013.

[12] G. M. R. Manzella and M. Gambetta. Implementation of real-time quality control procedures by means of a probabilistic estimate of seawater temperature and its temporal evolution. *Journal of Atmospheric and Oceanic Technology*, 30:609–625, 2013.

[13] N. P. Fofonoff and R. C. Millard. Algorithms for the computation of fundamental properties of seawater. *Unesco technical papers in marine sciences*, (44):1–53, 1983.

[14] G. Wahba and J. Wendelberger. Some new mathematical methods for variational objective analysis using splines and cross validation. *Monthly Weather Review*, (108):1122–1143, 1980.

[15] C. Troupin, M. Ouberdous, D. Sirjacobs, A. Alvera-Azcárate, A. Barth, M.-E. Toussaint, and J.-M. Beckers. Diva user guide. *Ocean Modelling*, 2013.

[16] M. Tonani, N. Pinardi, S. Dobricic, I. Pujol, and C. Fratianni. A high-resolution free-surface model of the mediterranean sea. *Ocean Science*, (4):1–14, 2008.

[17] A.H. Murphy. What is a good forecast? an essay on the nature of goodness in weather forecasting. *Weathere Forecasting*, (8):281–293, 1993.

[18] M. Rixen, J.M. Beckers, and C. Maillard. A hydrographic and biochemical climatology of the mediterranean and the black seas: some statistical pitfalls. *Brown, M. et al. (Ed.)*

(2002). The Colour of Ocean Data: International Symposium on oceanographic data and information management, with special attention to biological data. Brussels, Belgium, 25-27 November 2002: book of abstracts. VLIZ Special Publication, 11: pp. 8, 2002.

[19] G. M. R. Manzella, E. Scoccimarro, N. Pinardi, and M. Tonani. Improved near real-time data management procedures for the mediterranean ocean forecasting system-voluntary observing ship program. *Annales Geophysicae*, 21:49–62, 2003.

[20] W. J. Emery and R. E. Thomson. *Data Analysis Methods in Physical Oceanography - Second and Revised Edition*. ELSEVIER, 638 pp., 2001.

[21] G. Montanari, Rinaldi A., N. Pinardi, S. Simoncelli, and L. Giacomelli. *Le correnti costiere in Emilia-Romagna nel periodo 1995-2002*. I quaderni di Arpa, ARPA, Agenzia Regionale Prevenzione e Ambiente dell'Emilia-Romagna, Bologna, 160 pp., 2006.

[22] J.M Brankart and P. Brasseur. Optimal analysis of in situ data in the western mediterranean using statistics and cross-validation. *Journal of Atmospheric and Oceanic Technology*, (13):477–491, 1996.

[23] M. Rixen, J.M. Beckers, J.M Brankart, and P. Brasseur. A numerically efficient data method with error map generation. *Ocean Modelling*, (2):45–60, 2000.

[24] A Barth, A.A. Alvera-Azcárate, P. Joassin, J.M. Beckers, and C Troupin. Introduction to optimal interpolation and variational analysis. 2008.

[25] C. Troupin, A. Barth, D. Sirjacobs, M. Ouberdous, J.-M. Brankart, P. Brasseur, M. Rixen, A. Alvera-Azcárate, M. Belounis, A. Capet, F. Lenartz, M.-E. Toussaint, and J.-M. Beckers. Generation of analysis and consistent error fields using the data interpolating variational analysis (diva). *Ocean Modelling*, 52-53:90–101, 2012.

[26] G. Wahba. *Spline model for observational data*. SIAM, 169 pp., 1990.

[27] P.P. Brasseur. A variational inverse method for the reconstruction of the general circulation fields in the northern bering sea. *Journal of Geophisical Research*, 96(C3):4891–4907, 1991.

[28] C. Troupin, M. Ouberdous, F. Machin, M. Rixen, D. Sirjacobs, and J.M. Beckers. Three-dimensional analysis of oceanographic data with the software diva. *Geophysical Research Abstracts, 4th EGU General Assembly*, 10, 2008.

[29] P.S. Fratantoni, T. Holzwarth-Davis, C. Bascuñán, and M.H. Taylor. Description of the 2010 oceanographic conditions on the northeast u.s. continental shelf. *US Dept Commer, Northeast Fish Sci Cent Ref Doc*, (12-16):32 p., 2012.

[30] A. Artegiani, D. Bregant, E. Paschini, N. Pinardi, F. Raicich, and Russo A. The adriatic sea general circulation. part i: Air–sea interactions and water mass structure. *Journal of Physical Oceanography*, 27:1492–1514, 1997.